

¹ A Search in the Two-Photon Final State for
² Evidence of New Particle Production in pp
³ Collisions at $\sqrt{s} = 7$ TeV

⁴ Rachel P. Yohay
University of Virginia
`rpy3y@virginia.edu`

⁵ May 17, 2012

Contents

7	1	The Supersymmetric Extension to the Standard Model	3
8	1.1	Supermultiplet Representation	3
9	1.2	The Unbroken SUSY Lagrangian	4
10	1.3	Soft SUSY Breaking	10
11	1.4	Gauge-Mediated SUSY Breaking	12
12	1.5	Phenomenology of General Gauge Mediation	15
13	1.6	Experimental Status of SUSY	19
14	2	Event Selection	25
15	2.1	Object Reconstruction	26
16	2.1.1	Photons	26
17	2.1.2	Electrons	37
18	2.1.3	Jets and Missing Transverse Energy	37
19	2.2	HLT	43
20	2.3	Event Quality	46
21	2.4	Photon Identification Efficiency	48
22	2.4.1	Tag and Probe Method	50
23	2.4.2	Photon Efficiency Scale Factor $\epsilon_e^{\text{data}}/\epsilon_e^{\text{MC}}$	53
24	3	Data Analysis	59
25	3.1	Modeling the QCD Background	63

26	3.1.1	Outline of the Procedure	63
27	3.1.2	Reweighting	64
28	3.1.3	Normalization	75
29	3.2	Modeling the Electroweak Background	75
30	3.3	Errors on the Background Prediction	81
31	3.4	Results	89
32	4	Interpretation of Results in Terms of GMSB Models	93
33	4.1	Simplified Models	93
34	4.2	Upper Limit Calculation and Model Exclusion	93
35	4.2.1	Signal Acceptance \times Efficiency	94
36	4.2.2	CL_s and the Profile Likelihood Test Statistic	96
37	4.3	Cross Section Upper Limits	103
38	4.4	Exclusion Contours	104
39	A	Monte Carlo Samples	107
40	A.0.1	List of Samples	107
41	A.0.2	Explanation of Naming Conventions	108

⁴² **Chapter 1**

⁴³ **The Supersymmetric Extension to
the Standard Model**

⁴⁵ The following introduction to SUSY focuses primarily on the aspects of the formalism that are relevant to phenomenology. In particular, most of the details of SUSY breaking (about which there is little theoretical consensus) are omitted, except where they are relevant to experiment. The notation is similar to that used in refs. [5] and [6], and much of the information presented is culled from those references.

⁵⁰ **1.1 Supermultiplet Representation**

⁵¹ The Standard Model is extended to include supersymmetry by the introduction of a supersymmetry transformation that takes fermionic states to bosonic states and vice versa. The resulting model is called the *minimal supersymmetric Standard Model* (MSSM). In analogy with the known symmetries of the Standard Model, the SUSY transformation has associated generators that obey defining commutation and anti-commutation relations, and a fundamental representation. All SM particles and their superpartners fall into one of two *supermultiplet* representations. Using the property that

$$n_F = n_B, \quad (1.1)$$

59 where n_F is the number of fermionic degrees of freedom per supermultiplet and n_B is
 60 the number of bosonic degrees of freedom, the two types of supermultiplets are

- 61 1. *Chiral supermultiplets*: one Weyl fermion (two helicity states $\Rightarrow n_F = 2$) and
 62 one complex scalar field (with two real components $\Rightarrow n_B = 2$)

 63 2. *Gauge supermultiplets*: One spin-1 vector boson (two helicity states $\Rightarrow n_B = 2$)
 64 and one Weyl fermion (two helicity states $\Rightarrow n_F = 2$)

65 In the gauge supermultiplet, the vector boson is assumed massless (i.e. before
 66 EWSB generates a mass for it). Since the superpartners to the SM particles have not
 67 yet been discovered, they must be significantly heavier than their SM counterparts.
 68 Unbroken SUSY predicts that the SM particles and their superpartners must have
 69 exactly the same mass, so ultimately a mechanism for SUSY breaking must be intro-
 70 duced to generate masses for the superpartners (see Sec. 1.3). Tables 1.1 and 1.2 show
 71 the chiral and gauge supermultiplets of the MSSM, respectively. Note that the scalar
 72 partners to the SM fermions are denoted by placing an “s” in front of their names,
 73 while the chiral fermion partners to the SM gauge bosons are denoted by appending
 74 “ino” to their names.

75 1.2 The Unbroken SUSY Lagrangian

76 The first piece of the full unbroken SUSY Lagrangian density consists of the kinetic
 77 and interacting terms related to the chiral supermultiplets. As explained in Sec. 1.1,
 78 a chiral supermultiplet consists of a Weyl fermion ψ (the ordinary fermion) and a
 79 complex scalar ϕ (the sfermion). For a collection of such chiral supermultiplets, the
 80 Lagrangian is

Table 1.1: Chiral supermultiplets of the supersymmetric Standard Model. Adapted from Table 1.1 of ref. [6].

Type of supermultiplet	Notation	Spin-0 component	Spin-1/2 component	Representation under $SU(3)_C \otimes SU(2)_L \otimes U(1)_Y$
Left-handed quark/squark doublet ($\times 3$ families)	Q	$(\tilde{u}_L \tilde{d}_L)$	$(u_L d_L)$	$(\mathbf{3}, \mathbf{2}, \frac{1}{6})$
Right-handed up-type quark/squark singlet ($\times 3$ families)	\bar{u}	\tilde{u}_R^*	u_R^\dagger	$(\bar{\mathbf{3}}, \mathbf{1}, -\frac{2}{3})$
Right-handed down-type quark/squark singlet ($\times 3$ families)	\bar{d}	\tilde{d}_R^*	d_R^\dagger	$(\bar{\mathbf{3}}, \mathbf{1}, \frac{1}{3})$
Left-handed lepton/slepton doublet ($\times 3$ families)	L	$(\tilde{\nu}_{eL} \tilde{e}_L)$	$(\bar{\nu}_{eL} e_L)$	$(\mathbf{1}, \mathbf{2}, -\frac{1}{2})$
Right-handed lepton/slepton singlet ($\times 3$ families)	\bar{e}	\tilde{e}_R^*	e_R^\dagger	$(\bar{\mathbf{1}}, \mathbf{1}, 1)$
Up-type Higgs/Higgsino doublet	H_u	$(H_u^+ H_u^0)$	$(\tilde{H}_u^+ \tilde{H}_u^0)$	$(\mathbf{1}, \mathbf{2}, \frac{1}{2})$
Down-type Higgs/Higgsino doublet	H_d	$(H_d^0 H_d^-)$	$(\tilde{H}_d^0 \tilde{H}_d^-)$	$(\mathbf{1}, \mathbf{2}, -\frac{1}{2})$

Table 1.2: Gauge supermultiplets of the supersymmetric Standard Model. Adapted from Table 1.2 of ref. [6].

Type of supermultiplet	Spin-1/2 component	Spin-1 component	Representation under $SU(3)_C \otimes SU(2)_L \otimes U(1)_Y$
Gluon/gluino	\tilde{g}	g	$(\mathbf{8}, \mathbf{1}, 0)$
W/wino	$\tilde{W}^\pm \tilde{W}^0$	$W^\pm W^0$	$(\mathbf{1}, \mathbf{3}, 0)$
B/bino	\tilde{B}^0	B^0	$(\mathbf{1}, \mathbf{1}, 0)$

$$\begin{aligned}\mathcal{L}_{\text{chiral}} = & -\partial^\mu \phi^{*i} \partial_\mu \phi_i - V_{\text{chiral}}(\phi, \phi^*) - i\psi^{\dagger i} \bar{\sigma}^\mu \partial_\mu \psi_i - \frac{1}{2} M^{ij} \psi_i \psi_j \\ & - \frac{1}{2} M_{ij}^* \psi^{\dagger i} \psi^{\dagger j} - \frac{1}{2} y^{ijk} \phi_i \psi_j \psi_k - \frac{1}{2} y_{ijk}^* \phi^{*i} \psi^{\dagger j} \psi^{\dagger k}\end{aligned}\quad (1.2)$$

where i runs over all supermultiplets in Table 1.1, $\bar{\sigma}^\mu$ are $-1 \times$ the Pauli matrices (except for $\sigma^0 = \bar{\sigma}^0$), M^{ij} is a mass matrix for the fermions, y^{ijk} are the Yukawa couplings between one scalar and two spinor fields, and $V_{\text{chiral}}(\phi, \phi^*)$ is the scalar potential

$$\begin{aligned}V_{\text{chiral}}(\phi, \phi^*) = & M_{ik}^* M^{kj} \phi^{*i} \phi_j + \frac{1}{2} M^{in} y_{jkn}^* \phi_i \phi^{*j} \phi^{*k} \\ & + \frac{1}{2} M_{in}^* y^{jkn} \phi^{*i} \phi_j \phi_k + \frac{1}{4} y^{ijn} y_{klm}^* \phi_i \phi_j \phi^{*k} \phi^{*l}.\end{aligned}\quad (1.3)$$

The Lagrangian can also be written as the kinetic terms plus derivatives of the *superpotential* W :

$$\begin{aligned}\mathcal{L}_{\text{chiral}} = & -\partial^\mu \phi^{*i} \partial_\mu \phi_i - i\psi^{\dagger i} \bar{\sigma}^\mu \partial_\mu \psi_i \\ & - \frac{1}{2} \left(\frac{\delta^2 W}{\delta \phi^i \delta \phi^j} \psi_i \psi_j + \frac{\delta^2 W^*}{\delta \phi_i \delta \phi_j} \psi^{\dagger i} \psi^{\dagger j} \right) - \frac{\delta W}{\delta \phi^i} \frac{\delta W^*}{\delta \phi_i}\end{aligned}\quad (1.4)$$

where

$$W = M^{ij} \phi_i \phi_j + \frac{1}{6} y^{ijk} \phi_i \phi_j \phi_k. \quad (1.5)$$

The second part of the Lagrangian involves the gauge supermultiplets. In terms of the spin-1 ordinary gauge boson A_μ^a and the spin-1/2 Weyl spinor gaugino λ^a of

⁹⁰ the gauge supermultiplet, where a runs over the number of generators for the SM
⁹¹ subgroup (i.e. 1-8 for $SU(3)_C$, 1-3 for $SU(2)_L$, and 1 for $U(1)_Y$), this part of the
⁹² Lagrangian is

$$\mathcal{L}_{\text{gauge}} = -\frac{1}{4}F_{\mu\nu}^a F^{\mu\nu a} - i\lambda^{\dagger a}\bar{\sigma}^\mu D_\mu \lambda^a + \frac{1}{2}D^a D^a \quad (1.6)$$

⁹³ where

$$F_{\mu\nu}^a = \partial_\mu A_\nu^a - \partial_\nu A_\mu^a + g f^{abc} A_\mu^b A_\nu^c \quad (1.7)$$

⁹⁴ (g is the coupling constant and f^{abc} are the structure constants for the particular SM
⁹⁵ gauge group),

$$D_\mu \lambda^a = \partial_\mu \lambda^a + g f^{abc} A_\mu^b \lambda^c, \quad (1.8)$$

⁹⁶ and D^a is an auxiliary field that does not propagate (in the literature, it is used as a
⁹⁷ bookkeeping tool and can be removed via its algebraic equation of motion).

⁹⁸ To build a fully supersymmetric and gauge-invariant Lagrangian, the ordinary
⁹⁹ derivatives in $\mathcal{L}_{\text{chiral}}$ (Eq. 1.2) must be replaced by covariant derivatives

$$D_\mu \phi_i = \partial_\mu \phi_i - ig A_\mu^a (T^a \phi)_i \quad (1.9)$$

$$D_\mu \phi^{*i} = \partial_\mu \phi^{*i} + ig A_\mu^a (\phi^* T^a)^i \quad (1.10)$$

$$D_\mu \psi_i = \partial_\mu \psi_i - ig A_\mu^a (T^a \psi)_i. \quad (1.11)$$

¹⁰⁰ This leads to the full Lagrangian

$$\begin{aligned}
\mathcal{L} &= \mathcal{L}_{\text{chiral}} + \mathcal{L}_{\text{gauge}} \\
&\quad - \sqrt{2}g(\phi^{*i}T^a\psi_i)\lambda^a - \sqrt{2}g\lambda^{\dagger a}(\psi^{\dagger i}T^a\phi_i) + g(\phi^{*i}T^a\phi_i)D^a \\
&= -\partial^\mu\phi^{*i}\partial_\mu\phi_i - i\psi^{\dagger i}\bar{\sigma}^\mu\partial_\mu\psi_i + ig\partial^\mu\phi^{*i}A_\mu^a(T^a\phi)_i - ig\partial_\mu\phi_iA^{\mu a}(\phi^*T^a)^i \\
&\quad - g^2A^{\mu a}(\phi^*T^a)^iA_\mu^a(T^a\phi)_i - g\psi^{\dagger i}\bar{\sigma}^\mu A_\mu^a(T^a\psi)_i - V_{\text{chiral}}(\phi, \phi^*) \\
&\quad - \frac{1}{2}M^{ij}\psi_i\psi_j - \frac{1}{2}M_{ij}^*\psi^{\dagger i}\psi^{\dagger j} - \frac{1}{2}y^{ijk}\phi_i\psi_j\psi_k - \frac{1}{2}y_{ijk}^*\phi^{*i}\psi^{\dagger j}\psi^{\dagger k} \\
&\quad - \frac{1}{4}F_{\mu\nu}^aF^{\mu\nu a} - i\lambda^{\dagger a}\bar{\sigma}^\mu\partial_\mu\lambda^a - ig\lambda^{\dagger a}\bar{\sigma}^\mu f^{abc}A_\mu^b\lambda^c + \frac{1}{2}D^aD^a \\
&\quad - \sqrt{2}g(\phi^{*i}T^a\psi_i)\lambda^a - \sqrt{2}g\lambda^{\dagger a}(\psi^{\dagger i}T^a\phi_i) + g(\phi^{*i}T^a\phi_i)D^a. \tag{1.12}
\end{aligned}$$

¹⁰¹ Writing out $F_{\mu\nu}^a$ and $V_{\text{chiral}}(\phi, \phi^*)$ explicitly combining the D^a terms using the equation

¹⁰² of motion $D^a = -g\phi^{*i}T^a\phi_i$, and rearranging some terms, the final unbroken SUSY

¹⁰³ Lagrangian is

$$\begin{aligned}
\mathcal{L} = & -\partial^\mu \phi^{*i} \partial_\mu \phi_i - i\psi^{\dagger i} \bar{\sigma}^\mu \partial_\mu \psi_i \\
& - \frac{1}{4} (\partial_\mu A_\nu^a - \partial_\nu A_\mu^a) (\partial^\mu A^{\nu a} - \partial^\nu A^{\mu a}) - i\lambda^{\dagger a} \bar{\sigma}^\mu \partial_\mu \lambda^a \\
& - M_{ik}^* M^{kj} \phi^{*i} \phi_j - \frac{1}{2} M^{ij} \psi_i \psi_j - \frac{1}{2} M_{ij}^* \psi^{\dagger i} \psi^{\dagger j} \\
& + ig \partial^\mu \phi^{*i} A_\mu^a (T^a \phi)_i - ig \partial_\mu \phi_i A^{\mu a} (\phi^* T^a)^i - g \psi^{\dagger i} \bar{\sigma}^\mu A_\mu^a (T^a \psi)_i \\
& - ig \lambda^{\dagger a} \bar{\sigma}^\mu f^{abc} A_\mu^b \lambda^c \\
& - \frac{1}{4} g f^{abc} [(\partial_\mu A_\nu^a - \partial_\nu A_\mu^a) A^{\mu b} A^{\nu c} + A_\mu^b A_\nu^c (\partial^\mu A^{\nu a} - \partial^\nu A^{\mu a})] \\
& - \frac{1}{2} M_{in}^* y^{jkn} \phi^{*i} \phi_j \phi_k - \frac{1}{2} M^{in} y_{jkn}^* \phi_i \phi^{*j} \phi^{*k} \\
& - \frac{1}{2} y^{ijk} \phi_i \psi_j \psi_k - \frac{1}{2} y_{ijk}^* \phi^{*i} \psi^{\dagger j} \psi^{\dagger k} \\
& - \sqrt{2} g (\phi^{*i} T^a \psi_i) \lambda^a - \sqrt{2} g \lambda^{\dagger a} (\psi^{\dagger i} T^a \phi_i) \\
& - g^2 A^{\mu a} (\phi^* T^a)^i A_\mu^a (T^a \phi)_i - \frac{1}{4} g^2 f^{abc} A_\mu^b A_\nu^c f^{abc} A^{\mu b} A^{\nu c} \\
& - \frac{1}{4} y^{ijn} y_{kln}^* \phi_i \phi_j \phi^{*k} \phi^{*l} - \frac{1}{2} g^2 (\phi^{*i} T^a \phi_i)^2.
\end{aligned} \tag{1.13}$$

¹⁰⁴ The above Lagrangian applies to chiral supermultiplets interacting with one kind
¹⁰⁵ of gauge supermultiplet (i.e. one SM gauge group). In the general case, there are
¹⁰⁶ additional terms corresponding to interactions with all three SM gauge groups.

¹⁰⁷ The following list gives a description of the terms in Eq. 1.13:

- ¹⁰⁸ • First two lines: kinetic terms for the four types of fields ϕ_i , ψ_i , A_μ^a , and λ^a
- ¹⁰⁹ • Third line: mass terms for the ϕ_i and ψ_i (see Figs. 1.1(a) and 1.1(b))
- ¹¹⁰ • Fourth and fifth lines: cubic couplings in which ϕ_i , ψ_i , or λ^a radiates an A_μ^a (see
¹¹¹ Figs. 1.1(c), 1.1(d), and 1.1(e))
- ¹¹² • Sixth line: triple gauge boson couplings (see Fig. 1.1(f))
- ¹¹³ • Seventh line: triple sfermion couplings (see Fig. 1.1(g))

- ¹¹⁴ • Eighth line: cubic couplings in which ψ_i radiates a ϕ_i (see Fig. 1.1(h))
- ¹¹⁵ • Ninth line: ϕ_i - ψ_i - λ^a vertices (see Fig. 1.1(i))
- ¹¹⁶ • 10th line: A_μ^a - A_μ^a - ϕ_i - ϕ_i and quadruple gauge boson couplings (see Figs. 1.1(j)
¹¹⁷ and 1.1(k))
- ¹¹⁸ • 11th line: ϕ_i^4 vertices (see Figs. 1.1(l) and 1.1(m))

¹¹⁹ 1.3 Soft SUSY Breaking

¹²⁰ Since quadratic divergences in sfermion masses vanish to all orders in perturbation
¹²¹ theory in plain unbroken SUSY [6] due to the presence of gauge and Yukawa interac-
¹²² tions with the necessary relationships between coupling constants, it is desirable that
¹²³ the terms that break SUSY not disturb this property. In addition, SUSY should be
¹²⁴ broken spontaneously, as electroweak symmetry is broken in the Standard Model, so
¹²⁵ that it is only made manifest at high energies. To satisfy these constraints, SUSY-
¹²⁶ breaking terms are simply added to the unbroken SUSY Lagrangian in Eq. 1.13 such
¹²⁷ that $\mathcal{L}_{\text{total}} = \mathcal{L}_{\text{unbroken}} + \mathcal{L}_{\text{breaking}}$. The coefficients of terms in $\mathcal{L}_{\text{breaking}}$ must have
¹²⁸ positive mass dimension in order not to contribute quadratically divergent loop cor-
¹²⁹ rections to the scalar masses (like the Higgs mass).¹ This form of SUSY breaking is
¹³⁰ called *soft*, and all coefficients of soft SUSY breaking terms are expected to be of
¹³¹ order m_{soft} or m_{soft}^2 .

¹This point can be argued via dimensional analysis. Radiative corrections take the form Δm_S^2 , where m_S is the mass of the scalar particle in question. The dimensions of Δm_S^2 are mass². Δm_S^2 is proportional to some coupling constant or mass coefficient k multiplied by a function of Λ_{UV} , the high energy cutoff scale. The function of Λ_{UV} is determined by a loop integral, and thus typically takes the form Λ_{UV}^2 (quadratically divergent) or $\ln \frac{\Lambda_{\text{UV}}}{m_{\text{low}}}$ (logarithmically divergent, where m_{low} is some other lower-mass scale in the problem). Now, if k already contributes at least one power of mass to Δm_S^2 , then the high-energy behavior—the function of Λ_{UV} —can only contribute at most one power of the dimensionful parameter Λ_{UV} . However, there are typically no loop integrals that diverge linearly in Λ_{UV} , so by forcing k to have positive mass dimension, the form of the radiative corrections contributed by SUSY-breaking terms is limited to $\Delta m_S^2 \sim m_{\text{low}}^2 \ln \frac{\Lambda_{\text{UV}}}{m_{\text{low}}}$. In effect, the possibility of dangerous corrections proportional to Λ_{UV}^2 is excluded by dimensional analysis if the requirement that k contribute at least one power of mass is enforced.

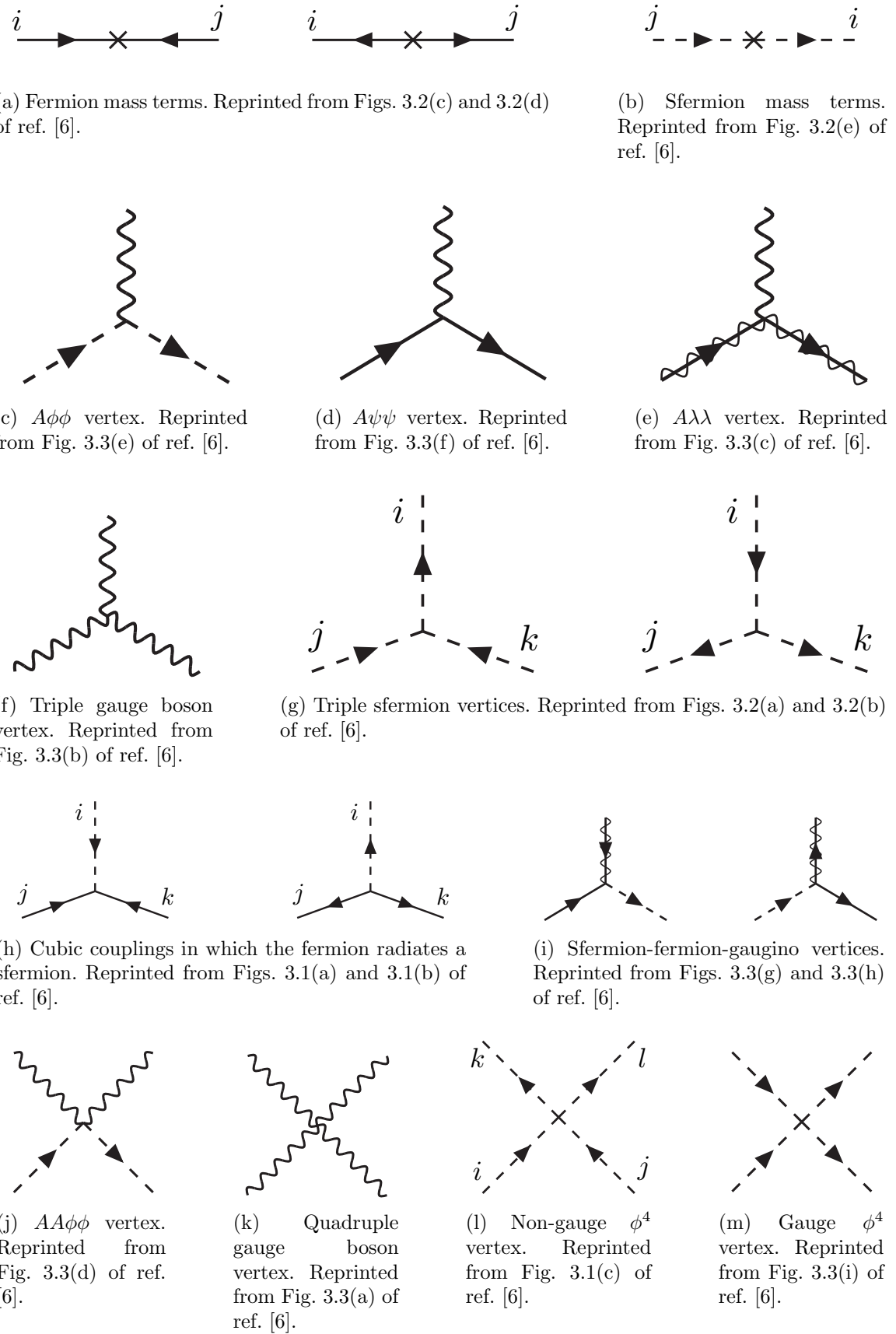


Figure 1.1: Interactions in the unbroken SUSY Lagrangian.

¹³² Soft SUSY breaking terms give masses to the sfermions and gauginos and introduce
¹³³ a cubic sfermion vertex. The soft terms are given by

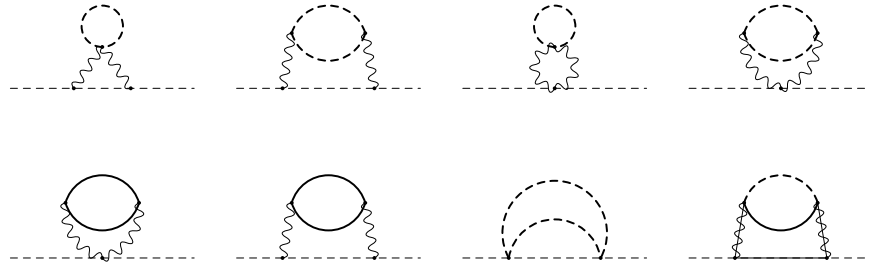
$$\begin{aligned}
 \mathcal{L}_{\text{soft}} = & -\frac{1}{2}(M_3\tilde{g}^a\tilde{g}^a + M_2\tilde{W}^a\tilde{W}^a + M_1\tilde{B}\tilde{B} + \text{h.c.}) \\
 & - (a_u^{ij}\tilde{u}_{Ri}^*\tilde{Q}_j H_u - a_d^{ij}\tilde{d}_{Ri}^*\tilde{Q}_j H_d - a_e^{ij}\tilde{e}_{Ri}^*\tilde{L}_j H_d + \text{h.c.}) \\
 & - m_{\tilde{Q}_{ij}}^2 \tilde{Q}_i^\dagger \tilde{Q}_j - m_{\tilde{L}_{ij}}^2 \tilde{L}_i^\dagger \tilde{L}_j \\
 & - m_{\tilde{u}_{ij}}^2 \tilde{u}_{Ri} \tilde{u}_{Rj}^* - m_{\tilde{d}_{ij}}^2 \tilde{d}_{Ri} \tilde{d}_{Rj}^* - m_{\tilde{e}_{ij}}^2 \tilde{e}_{Ri} \tilde{e}_{Rj}^* \\
 & - m_{H_u}^2 H_u^* H_u - m_{H_d}^2 H_d^* H_d - (b H_u H_d + \text{h.c.})
 \end{aligned} \tag{1.14}$$

¹³⁴ where a runs from 1-8 for \tilde{g}^a and from 1-3 for \tilde{W}^a , and i, j run over the three families.
¹³⁵ The color indices are not shown. The first line of Eq. 1.14 contains the gaugino mass
¹³⁶ terms. The second line contains cubic scalar couplings that contribute to mixing
¹³⁷ between the left- and right-handed third generation sfermions (it is assumed in the
¹³⁸ supersymmetric Standard Model that the a_u^{ij} , a_d^{ij} , and a_e^{ij} are negligible unless $i =$
¹³⁹ $j = 3$). The third and fourth lines of Eq. 1.14 contain squark and slepton mass terms,
¹⁴⁰ and finally the last line contains the Higgs mass terms.

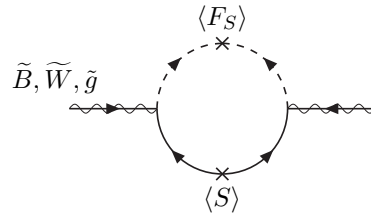
¹⁴¹ Many viable models of achieving soft SUSY breaking have been studied over the
¹⁴² last 30 years. For an overview, see Sec. 6 of ref. [6]. However, this thesis will only cover
¹⁴³ *gauge-mediated SUSY breaking* (GMSB), because the two-photon search performed
¹⁴⁴ is far more sensitive to this model than to other models of SUSY breaking.

¹⁴⁵ 1.4 Gauge-Mediated SUSY Breaking

¹⁴⁶ In gauge-mediated models [7], “hidden” fields spontaneously break the supersymme-
¹⁴⁷ try of very heavy chiral *messenger* supermultiplets. There are a number of compet-
¹⁴⁸ ing models (see ref. [7]) that explain the precise mechanism of spontaneous SUSY



(a) Sfermion mass terms. Heavy dashed lines denote messenger sfermions; solid lines denote messenger fermions. Reprinted from Fig. 6.4 of ref. [6].



(b) Gaugino mass term. The $\langle S \rangle$ part of the loop is a messenger fermion contribution; the $\langle F_S \rangle$ part is a messenger sfermion contribution. Reprinted from Fig. 6.3 of ref. [6].

Figure 1.2: Contributions to sfermion and gaugino masses from loop interactions with messenger particles in the GMSB framework.

149 breaking, but fortunately the details of those models mostly decouple from the phe-
 150 nomenology of GMSB. The messengers then communicate the SUSY breaking to the
 151 sparticles via loop diagrams of gauge interaction strength (i.e. via vertices like those
 152 shown in Figs. 1.1(c), 1.1(d), 1.1(i), 1.1(j), and 1.1(m), which are proportional to
 153 the SM gauge couplings constants). Feynman diagrams corresponding to gaugino and
 154 sfermion mass terms are shown in Figure 1.2.

155 Historically, GMSB and gravity-mediated SUSY breaking, or mSUGRA [8], have
 156 been the two most thoroughly experimentally studied scenarios of SUSY breaking.
 157 One advantage of GMSB over mSUGRA is that it naturally suppresses flavor vio-
 158 lation, a generic prediction of supersymmetry. Flavor violation is introduced in the
 159 scalar³ couplings and sfermion mass terms of $\mathcal{L}_{\text{soft}}$ (second, third, and fourth lines of

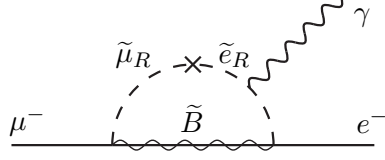


Figure 1.3: Possible contribution to $\mu \rightarrow e\gamma$ from $m_{\tilde{e}ij}$ soft term. Reprinted from Fig. 5.6(a) of ref. [6].

Eq. 1.14). Since a_u^{ij} , a_d^{ij} , a_e^{ij} , $m_{\tilde{Q}ij}$, $m_{\tilde{L}ij}$, $m_{\tilde{u}ij}$, $m_{\tilde{d}ij}$, and $m_{\tilde{e}ij}$ are matrices in family space, any nonzero off-diagonal elements will lead to mixing between sfermions of different families. This can lead, for example, to contributions to the diagram $\mu \rightarrow e\gamma$ (Figure 1.3) exceeding the experimental bounds. To avoid this disaster, *universality* conditions are assumed:

$$\mathbf{m}_{\tilde{\mathbf{Q}}}^2 = m_{\tilde{Q}}^2 \mathbf{1}, \mathbf{m}_{\tilde{\mathbf{L}}}^2 = m_{\tilde{L}}^2 \mathbf{1}, \mathbf{m}_{\tilde{\mathbf{u}}}^2 = m_{\tilde{u}}^2 \mathbf{1}, \mathbf{m}_{\tilde{\mathbf{d}}}^2 = m_{\tilde{d}}^2 \mathbf{1}, \mathbf{m}_{\tilde{\mathbf{e}}}^2 = m_{\tilde{e}}^2 \mathbf{1} \quad (1.15)$$

i.e. all sfermion mass matrices arising from the soft terms are assumed to be proportional to the unit matrix $\mathbf{1}$, such that there can be no flavor mixing from these terms and contributions to flavor-changing processes are drastically reduced.² In mSUGRA models, universality is assumed from the beginning, while in GMSB it is a natural consequence of the fact that the sparticle-messenger vertices are flavor-blind.

In minimal GMSB (mGMSB), there are four messenger supermultiplets q, \bar{q}, l, \bar{l} providing the messenger (s)quarks and (s)leptons. There is one breaking scale Λ . The gaugino masses computed from diagrams like Fig. 1.2(b) are given by

$$M_a = \frac{\alpha_a}{4\pi} \Lambda \quad (1.16)$$

²Universality also includes some assumptions about the form of a_{uij} , a_{dij} , and a_{eij} and the stipulation that the soft terms not introduce any CP-violating phases.

¹⁷³ where a runs from 1-3 and the α_a are the SM gauge coupling constants. The sfermion
¹⁷⁴ masses computed from diagrams like Fig. 1.2(a) are given by

$$m_{\phi_i}^2 = 2\Lambda^2 \sum_{a=1}^3 \left(\frac{\alpha_a}{4\pi}\right)^2 C_a(i) \quad (1.17)$$

¹⁷⁵ where $C_a(i)$ are group theory factors that are identical for all particles residing in
¹⁷⁶ the same type of supermultiplet (e.g. for all left-handed (s)quarks or left-handed
¹⁷⁷ (s)leptons). As explained in the previous paragraph, the gaugino and sfermion masses
¹⁷⁸ do not depend on fermion family.

¹⁷⁹ In recent years, much theoretical progress has been made in unifying models of
¹⁸⁰ gauge mediation and developing less restrictive models than mGMSB. *General gauge*
¹⁸¹ *mediation* (GGM) [9] retains the essential features of mGMSB, such as flavor de-
¹⁸² generacy and communication of SUSY breaking via messengers, but does not make
¹⁸³ assumptions about the specific messenger sector or SUSY breaking scale. Many dif-
¹⁸⁴ ferent collider final states can be interpreted in terms of GGM, and conversely, GGM
¹⁸⁵ implies a wealth of signatures, only a small fraction of which have been searched for
¹⁸⁶ at colliders [10, 11, 12]. The following section discusses the aspects of GGM collider
¹⁸⁷ phenomenology relevant to this thesis.

¹⁸⁸ 1.5 Phenomenology of General Gauge Mediation

¹⁸⁹ The main distinguishing feature of all GMSB phenomenology is that the gravitino \tilde{G} is
¹⁹⁰ very light (eV-keV). In general, the gravitino mass is proportional to $\langle F \rangle / M_P$, where
¹⁹¹ $\langle F \rangle$ is the vacuum expectation value (VEV) of a field F that spontaneously breaks
¹⁹² SUSY in the vacuum state and M_P is the Planck mass. In GGM models, $\langle F \rangle \sim 10^8$
¹⁹³ GeV, leading to a very light gravitino. In contrast, mSUGRA predicts $\langle F \rangle \sim 10^{20}$
¹⁹⁴ GeV. The fact that the gravitino is so much lighter than any other particles in the

¹⁹⁵ supersymmetric Standard Model, and that it interacts only gravitationally (and thus
¹⁹⁶ extremely feebly), leads to two important phenomenological consequences:

- ¹⁹⁷ 1. All sparticle decay chains end with the production of a gravitino.
- ¹⁹⁸ 2. The gravitino escapes 4π , hermetic collider detectors without interacting, leav-
¹⁹⁹ ing a signature of “missing” momentum transverse to the beam direction.

²⁰⁰ Even if the gravitino were lighter than any other sparticle, but heavier than an
²⁰¹ ordinary SM particle, it still could not decay to the SM particle due to *R-parity*. R-
²⁰² parity is a conserved quantity of the supersymmetric Standard Model that enforces
²⁰³ baryon and lepton number conservation, which would otherwise be generically allowed
²⁰⁴ at levels in conflict with experiment (e.g. the non-observation of baryon- and lepton-
²⁰⁵ number-violating proton decay). All sparticles have R-parity -1, while all ordinary SM
²⁰⁶ particles have R-parity +1, and R-parity conservation dictates that at any vertex, the
²⁰⁷ product of the R-parities of each leg must be +1. This leads to two more important
²⁰⁸ consequences:

- ²⁰⁹ 1. Since conservation of energy only allows it to decay to ordinary SM particles,
²¹⁰ but R-parity prevents a sparticle-particle-particle vertex, the *lightest supersym-
²¹¹ metric particle* (LSP) must be absolutely stable. All sparticle decays proceed
²¹² through the *next-to-lightest supersymmetric particle* (NLSP), which in turn de-
²¹³ cays to the LSP. The fact that it is stable and only gravitationally interacting
²¹⁴ makes the gravitino a candidate dark matter particle (see Sec. 1.6).
- ²¹⁵ 2. In colliders, sparticles are produced in pairs (particle + particle \rightarrow sparticle +
²¹⁶ sparticle).

²¹⁷ In GMSB, then, the gravitino is the LSP. If the NLSP is a gaugino,³ then the
²¹⁸ possible decays depend on mixing among the gauginos. Due to the effects of EWSB,

³In principle, the NLSP could be anything, but in most popular GGM models, it is either a gaugino or a stau. The stau NLSP search is not the subject of this thesis, so it will not be considered in this section.

²¹⁹ the four neutral gauginos \tilde{H}_u^0 , \tilde{H}_d^0 , \tilde{B} , \tilde{W}^0 mix into four *neutralino* mass eigenstates
²²⁰ $\tilde{\chi}_1^0, \tilde{\chi}_2^0, \tilde{\chi}_3^0, \tilde{\chi}_4^0$, and the four charged gauginos $\tilde{H}_u^+, \tilde{H}_d^-, \tilde{W}^+, \tilde{W}^-$ mix into two *chargino*
²²¹ mass eigenstates $\tilde{\chi}_1^\pm, \tilde{\chi}_2^\pm$ (two mass eigenstates each with two possible charges = four
²²² particles). In the limit that EWSB effects are small, the neutralino and chargino
²²³ masses can be written as the gauge eigenstate masses plus a small perturbation:

$$m_{\tilde{\chi}_1^0} = M_1 - \frac{m_Z^2 \sin^2 \theta_W (M_1 + \mu \sin 2\beta)}{\mu^2 - M_1^2} + \dots \quad (1.18)$$

$$m_{\tilde{\chi}_2^0} = M_2 - \frac{m_W^2 (M_2 + \mu \sin 2\beta)}{\mu^2 - M_2^2} + \dots \quad (1.19)$$

$$m_{\tilde{\chi}_3^0} = |\mu| + \frac{m_Z^2 (\text{sgn}(\mu) - \sin 2\beta)(\mu + M_1 \cos^2 \theta_W + M_2 \sin^2 \theta_W)}{2(\mu + M_1)(\mu + M_2)} + \dots \quad (1.20)$$

$$m_{\tilde{\chi}_4^0} = |\mu| + \frac{m_Z^2 (\text{sgn}(\mu) + \sin 2\beta)(\mu - M_1 \cos^2 \theta_W - M_2 \sin^2 \theta_W)}{2(\mu - M_1)(\mu - M_2)} + \dots \quad (1.21)$$

$$m_{\tilde{\chi}_1^\pm} = M_2 - \frac{m_W^2 (M_2 + \mu \sin 2\beta)}{\mu^2 - M_2^2} + \dots \quad (1.22)$$

$$m_{\tilde{\chi}_2^\pm} = |\mu| + \frac{m_W^2 \text{sgn}(\mu)(\mu + M_2 \sin 2\beta)}{\mu^2 - M_2^2} + \dots \quad (1.23)$$

²²⁴ where $\tan \beta = \langle H_u^0 \rangle / \langle H_d^0 \rangle$.

²²⁵ The two scenarios studied in ref. [12] are the following:

²²⁶ • **Bino NLSP:** $M_1 \sim$ few hundred GeV, $M_2, |\mu| \gg M_1$. All but the lightest
²²⁷ neutralino are effectively inaccessible at the LHC due to their large masses. The
²²⁸ NLSP can always decay to $\gamma + \tilde{G}$, and if it is heavy enough, to $Z + \tilde{G}$ or $H + \tilde{G}$.

²²⁹ • **Wino NLSP:** $M_2 \sim$ few hundred GeV, $M_1, |\mu| \gg M_2$. The lightest neutralino
²³⁰ and the lightest chargino are nearly degenerate in mass, and are the only two
²³¹ particles to play a role at the LHC. The decays described in the previous bullet
²³² point can happen, as well as chargino decays to $W + \tilde{G}$.

²³³ The subject of this thesis is the classic bino NLSP decay $\gamma + \tilde{G}$.

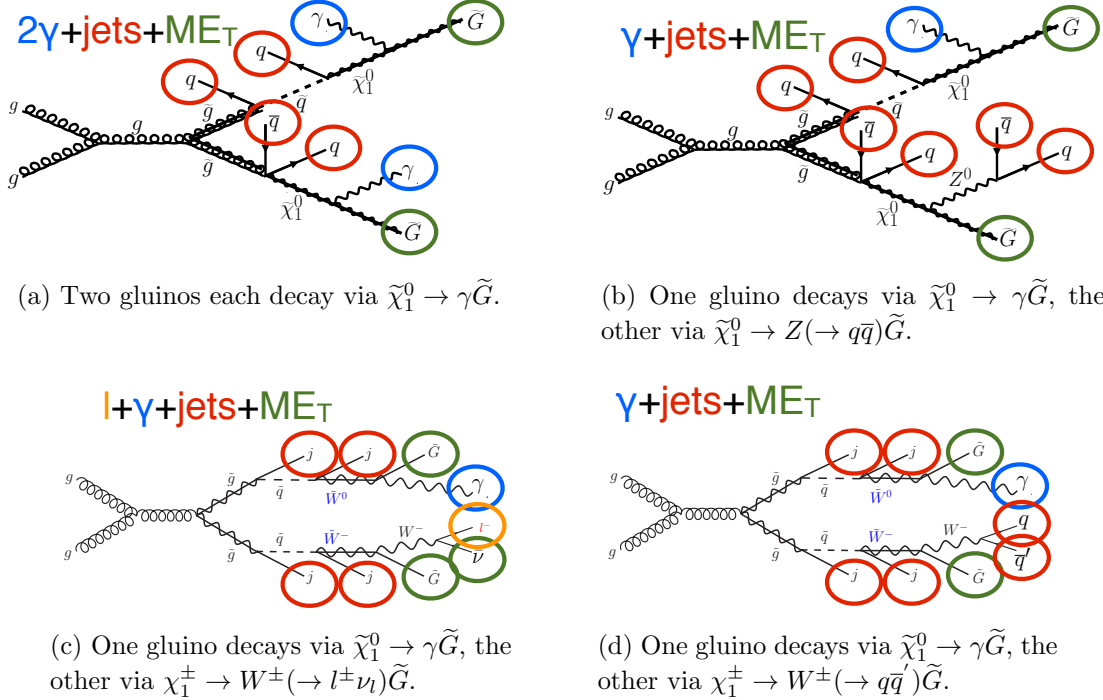


Figure 1.4: Typical LHC signatures of the bino and wino NLSP scenarios.

234 Since strong production of SUSY particles dominates over electroweak production
235 at the LHC due to the enhanced gg parton luminosity over the $q\bar{q}$ parton luminosity,
236 early LHC searches are particularly sensitive to light squarks and gluinos. General
237 gauge mediation makes no a priori restrictions on the mass splitting between the
238 strongly interacting sparticles and the weakly interacting sparticles, so models with
239 light squarks and gluinos are viable. In fact, such models could not be probed as
240 well at the Tevatron⁴ as they are at the LHC due to the aforementioned parton
241 luminosities.

242 Typical LHC signatures of the bino and wino NLSP scenarios are shown in Fig-
243 ure 1.4.

⁴Located on the Fermilab site in Batavia, Illinois, the Tevatron was a proton-antiproton collider operating at 1.96 TeV center-of-mass energy. The Tevatron ran from 1987 to 2011 [13].

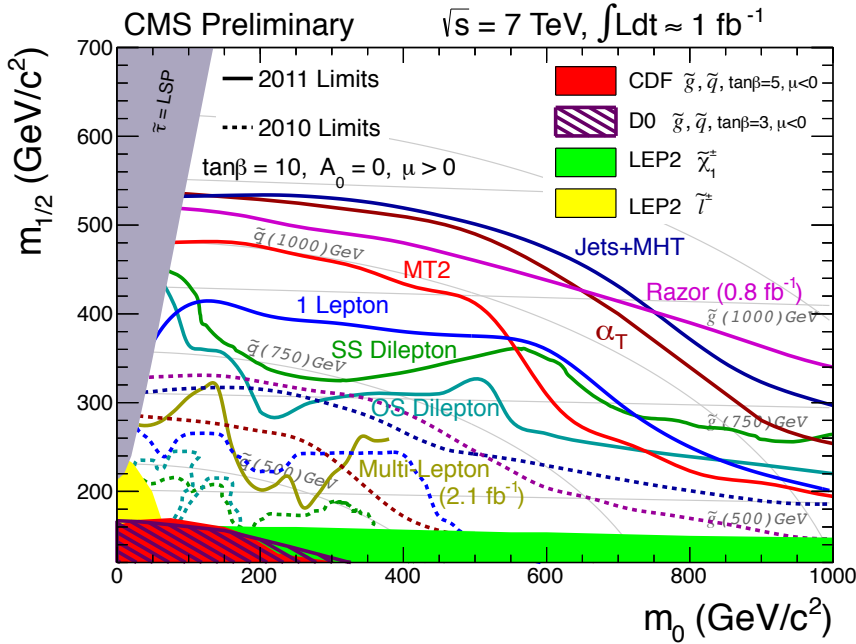


Figure 1.5: CMS limits on mSUGRA with $\tan \beta = 10$. The limits set by individual searches are shown as separate colored lines. Solid lines refer to 2011 searches (i.e. using an integrated luminosity of $\sim 1 \text{ fb}^{-1}$), while dashed lines refer to 2010 searches ($\sim 36 \text{ pb}^{-1}$). Reprinted from ref. [16].

²⁴⁴ 1.6 Experimental Status of SUSY

²⁴⁵ Collider searches for evidence of supersymmetry began in earnest in the 1980s [14]
²⁴⁶ and continue to this day. Most recently, the LHC and Tevatron experiments have set
²⁴⁷ the strictest limits on a variety of SUSY breaking scenarios, including GMSB and
²⁴⁸ mSUGRA.

²⁴⁹ Figure 1.5 shows the current limits set by the CMS experiment on the mSUGRA
²⁵⁰ model (with $\tan \beta = 10$) in the m_0 - $m_{1/2}$ plane. (Note that although the plot is trun-
²⁵¹ cated at $m_0 = 1000 \text{ GeV}/c^2$, some searches are sensitive out to $m_0 \sim 2000 \text{ GeV}/c^2$.)
²⁵² Although the LHC has pushed m_0 above $\sim 1 \text{ TeV}/c^2$ for $m_{1/2}$ up to $\sim 400 \text{ GeV}/c^2$,
²⁵³ casting some doubt onto the theory's prospects for solving the hierarchy problem,
²⁵⁴ there is still a sizable chunk of mSUGRA parameter space that is not ruled out by
²⁵⁵ collider experiments. Furthermore, parts of the CMS unexplored regions overlap with
²⁵⁶ areas allowed by astrophysics experiments [15].

257 Figure 1.6 shows the most up-to-date limit (using 1 fb^{-1} of integrated luminosity
 258 collected by the ATLAS experiment [17] at the LHC) on the Snowmass Points and
 259 Slopes (SPS) model of mGMSB, dubbed SPS8 [18]. The best limits on a variety
 260 of GGM models are shown in Figure 1.7 [19]. In these models, no assumptions are
 261 made about the specific parameters common to many gauge mediation models (e.g.
 262 the number of messengers or the relationship between the messenger mass and the
 263 SUSY breaking scale). Instead, it is only assumed that the lightest neutralino is light
 264 enough to be produced on-shell at the LHC (by setting M_1 and M_2 appropriately, see
 265 Sec. 1.5) and that it decays to a gravitino, that the gravitino is extremely relativistic
 266 (mass of order eV-keV), and that the gravitino is stable. The one-dimensional scan
 267 over SUSY breaking scales in the SPS8 model (in which the full sparticle spectrum is
 268 specified by the model parameters) is replaced by a two-dimensional scan over gluino
 269 and lightest neutralino mass in the GGM models (in which all sparticles except the
 270 gluino, first- and second-generation squarks, and neutralinos are forced to be at ~ 1.5
 271 TeV/c^2 , effectively decoupling them from the dynamics that can be probed with 1
 272 fb^{-1} at a $7 \text{ TeV}/c$ pp collider).

273 In general, the lifetime of the lightest neutralino in GMSB models can take on any
 274 value between hundreds of nanometers to a few kilometers depending on the mass
 275 of the lightest neutralino and the SUSY breaking scale [6]. The search published in
 276 ref. [10] (from which Figs. 1.6 and ?? are culled) considers only *prompt* neutralino
 277 variants, i.e. with neutralino lifetime short enough that the distance traveled by the
 278 neutralino before decay cannot be resolved by the detector. The most recent limits
 279 on non-prompt SPS8-style neutralino models were set by the Collider Detector at
 280 Fermilab (CDF) collaboration with 570 pb^{-1} , and are shown in Figure 1.8 [11].

281 Finally, if the gravitino is to make up some or all of the dark matter, constraints
 282 on the form of gauge mediation must come from cosmological considerations and
 283 astronomical observations. The gravitino in gauge mediation models is usually very

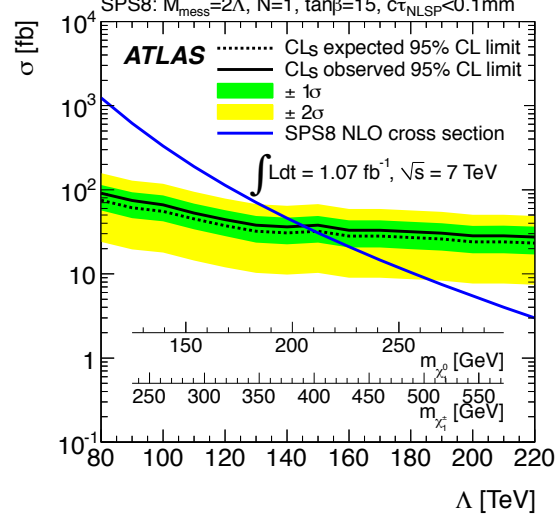


Figure 1.6: ATLAS cross section upper limit on the SPS8 [18] model of mGMSB as a function of SUSY breaking scale Λ , lightest neutralino mass $m_{\tilde{\chi}_1^0}$, or lightest chargino mass $m_{\tilde{\chi}_1^\pm}$. Values of Λ , $m_{\tilde{\chi}_1^0}$, or $m_{\tilde{\chi}_1^\pm}$ below the intersection point between the blue (predicted SPS8 cross section) and black (observed cross section upper limit) curves are excluded. The model parameters listed above the plot are defined in Secs. 1.4 and 1.5, except for τ_{NLSP} , which is the neutralino lifetime. Reprinted from ref. [10].

284 light ($\mathcal{O}(\text{eV-MeV})$) because it is proportional to the SUSY breaking scale divided by
 285 the Planck mass, and in GMSB the breaking scale is typically only of order a few
 286 hundred TeV ([6] and Sec. 1.5). A light, highly relativistic dark matter particle might
 287 have been produced, for instance, in the early, radiation-dominated period of the
 288 universe [20]. This *warm dark matter* (WDM) may be responsible for all of the dark
 289 matter needed to account for galactic structure, or it may share the duties with *cold*
 290 *dark matter* (CDM, weakly interacting particles with masses in the GeV range). In
 291 any viable model, the predicted relic density of the dark matter species must match
 292 the observed value of $\Omega h^2 \sim 0.1$ [21]. For many GMSB models, this measurement
 293 constrains the gravitino mass to the keV range [22]. This constraint, however, does
 294 not translate into a very strong bound on the lifetime of the lightest neutralino. Using
 295 the following equation (taken from [22]):

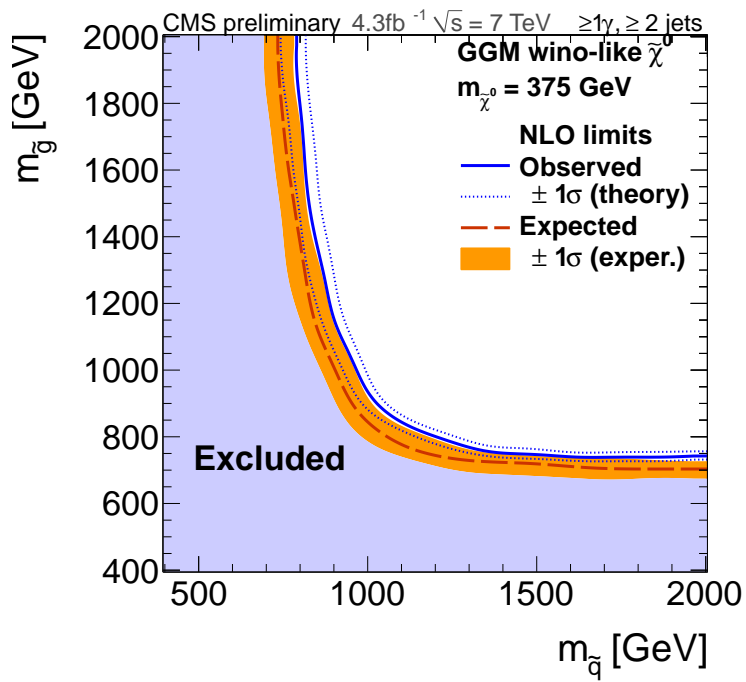
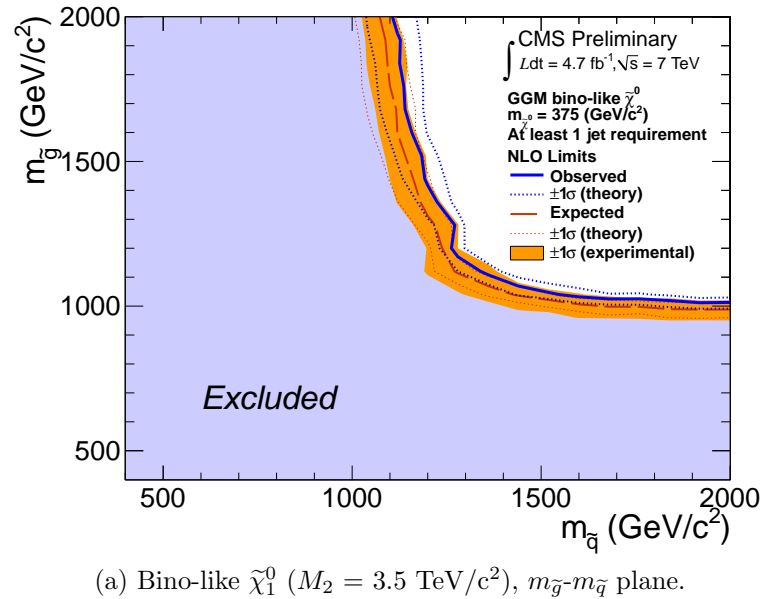


Figure 1.7: CMS exclusion contours for GGM models using 5 fb^{-1} of LHC data.
Reprinted from ref. [12].

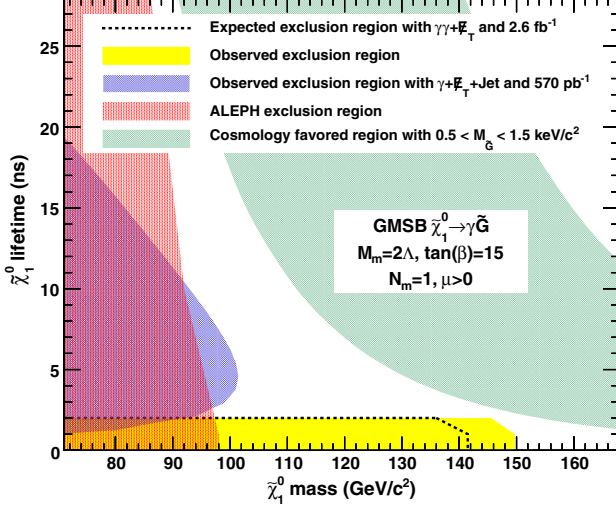


Figure 1.8: CDF exclusion contour in the $\tau_{\tilde{\chi}_1^0}$ - $m_{\tilde{\chi}_1^0}$ plane, where $\tau_{\tilde{\chi}_1^0}$ is the lifetime of the neutralino. Reprinted from ref. [11].

$$\tau_{\tilde{\chi}_1^0} \sim 130 \left(\frac{100 \text{ GeV}}{m_{\tilde{\chi}_1^0}} \right)^5 \left(\frac{\sqrt{\langle F \rangle}}{100 \text{ TeV}} \right)^4 \mu\text{m} \quad (1.24)$$

and applying the gravitino mass constraint $\sqrt{\langle F \rangle} \lesssim 3000 \text{ TeV}$ (cf. the first paragraph of Sec. 1.5 with $m_{\tilde{G}} \sim \text{keV}$) and $m_{\tilde{\chi}_1^0} = 100 \text{ GeV}$, the upper bound on the neutralino lifetime is 100 meters. For $\sqrt{\langle F \rangle} \sim 100 \text{ TeV}$, the neutralino lifetime is detectable on collider time scales.

Recently, a lower bound on the WDM particle mass in either pure warm or mixed warm and cold dark matter scenarios was set using observations of the Lyman- α forest. For pure WDM, $m_{\text{WDM}} > 8 \text{ keV}$, while for some mixed WDM-CDM scenarios, $m_{\text{WDM}} > 1.1\text{-}1.5 \text{ keV}$ [20, 23]. These bounds and others have motivated the development of more complicated gauge mediation models [23]. However, rather than focus on a specific GMSB model, of which there are many, the search detailed here is interpreted in a minimally model dependent way. With this approach, the results can be applied to many competing models. The remainder of this thesis is devoted to the experimental details of the search, analysis strategy, and presentation of the results. The work described in this thesis forms the basis for the CMS public result “Search

³¹⁰ for Supersymmetry in Events with Photons and Missing Energy” [19], published in
³¹¹ April 2012.

³¹² Chapter 2

³¹³ Event Selection

³¹⁴ In keeping with the phenomenology described in Sec. 1.5, the candidate GGM events
³¹⁵ selected in this search consist of two high- E_T photons and a significant momentum
³¹⁶ imbalance transverse to the beam, indicating the production of an escaping gravitino.
³¹⁷ This momentum imbalance is usually referred to as *missing transverse energy* and is
³¹⁸ denoted by the symbol \cancel{E}_T .

³¹⁹ However, in order to use real CMS data (as opposed to simulation) to derive pre-
³²⁰ dictions for the backgrounds to the search, *control samples* distinct from the *candidate*
³²¹ two-photon sample must be collected. These samples consist of different numerical
³²² combinations of photons, electrons, and jets, and are explained in more detail in
³²³ Chapter 3. Since this search is performed in the high- \cancel{E}_T tail of the \cancel{E}_T distribution,
³²⁴ where adequate detector simulation is very difficult, it is advantageous to use *data-
325 driven* background estimates, which capture the true detector response, over numbers
³²⁶ derived from simulation.

³²⁷ In the following sections, the reconstruction of photons, electrons, jets, and \cancel{E}_T
³²⁸ is explained. Sec. 2.1 begins with an explanation of the high level reconstruction.
³²⁹ It is followed by Sec. 2.2, which describes the triggers used to collect the candidate
³³⁰ and control samples. Sec. 2.3 describes event cleaning cuts that are applied to the

331 candidate and control samples. Finally, the chapter concludes with a measurement of
332 the photon identification efficiency in Sec. 2.4.

333 2.1 Object Reconstruction

334 This section describes the *offline* object reconstruction, i.e. the reconstruction of par-
335 ticle objects from events that have already been triggered and written to permanent
336 storage, as opposed to the building of trigger objects explained in Secs. ?? and 2.2.

337 2.1.1 Photons

338 Uncalibrated EB/EE Hits

339 Photon reconstruction begins with the ADC count value for each of the 10 recorded
340 time samples per ECAL crystal per trigger. To construct an *uncalibrated hit*, the
341 gain (1, 6, or 12; see Sec. ??) of each sample is determined and the ADC count
342 value scaled appropriately. The pedestal is estimated from the average of the first
343 three samples, which, for a properly timed in hit, should contain no signal. This
344 pedestal value is subtracted from the rest of the samples. Finally, the amplitude of the
345 pulse is reconstructed using a predetermined weight for each sample [24]. The weights
346 correspond to the pulse shape expected from the MGPA and shaping circuit response.
347 The time of the hit is also reconstructed using the ratios between neighboring time
348 samples [25]. A typical ECAL channel pulse shape is shown in Figure 2.1.

349 Calibrated EB/EE Hits

350 In the next phase of the photon reconstruction, calibrations are applied to the un-
351 calibrated hits to form *calibrated hits* with energy measured in GeV. Channels are
352 excluded from seeding calibrated hits if

- 353 • they are excessively noisy,

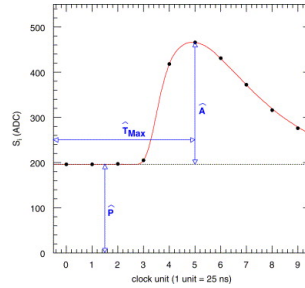


Figure 2.1: Typical ECAL channel pulse shape. \hat{P} is the pedestal value, \hat{A} is the pulse amplitude, and \hat{T}_{\max} is the hit time. The red line is the assumed pulse shape from which the weights are derived. Reprinted from ref. [24].

- 354 • they are stuck in fixed gain (i.e. the MGPA gain does not change properly to
355 avoid saturation),
- 356 • they are totally dead,
- 357 • they have one or more neighboring dead channels, or
- 358 • they do not have good trigger primitives (i.e. trigger primitive is missing, satu-
359 rated, or *spike-like*).

Added

360 *ECAL spikes* are hits in which low energy protons and heavy ions from jets ionize this
361 in the sensitive volume of the EB APD, causing the APD to register a fake large- para-
362 amplitude hit. Because they are not the result of a real electromagnetic shower, spikes graph
363 tend to be isolated. They may also appear to arrive early or late with respect to the and the
364 nominal bunch crossing. Most spikes are reconstructed with a hit time ~ 10 ns earlier next
365 than real EM hits because unlike real hits, whose pulse shapes include the time about
366 constant associated with crystal scintillation, the reconstructed spikes only involve spikes
367 the rise time of the electronics. There also is a long tail of late arriving spikes due to
368 slow neutrons from jets [26].

369 Because of their particular timing and topological characteristics, cuts have been
370 developed to effectively identify and reject spike-like hits. This analysis utilizes both
371 the “Swiss cross” cut $1 - E_4/E_1 > 0.95$, where E_1 is the energy of the spike candidate

372 crystal and E_4 is the sum of the energies in the four crystals whose edges are parallel to
373 the four edges of the spike candidate crystal, and a timing cut $t \geq 3$ ns, to flag spikes.
374 More information about these cuts can be found in ref. [26]. A simpler algorithm
375 using the fine grain veto bit of the L1 TPG is used to reject spikes at the trigger level
376 **[insert citation]**.

377 In addition to the trigger primitives, no uncalibrated hits that are spike-like are eli-
378 gible for calibration. The calibrations applied are crystal transparency loss corrections
379 measured continuously by the laser/LED system, energy intercalibrations (relative en-
380 ergy calibration between crystals), absolute scale calibrations between ADC counts
381 and GeV,¹ and time intercalibrations (relative time calibration between crystals).

382 The ECAL crystals were pre-calibrated before installation in CMS using labora-
383 tory light yield and photodetector gain measurements [28]. In addition, some EB and
384 EE crystals were intercalibrated using test beams [29], and all EB crystals were inter-
385 calibrated with cosmic ray muons [30]. EE precalibrations were validated with LHC
386 *splash events* in 2009 [30, 31], in which the beam was dumped onto a collimator ap-
387 proximately 150 meters upstream of CMS, causing a spray of muons to enter CMS at
388 one endcap and exit at the other. Splash events were also used to derive time intercal-
389ibration constants. Before colliding beam operations commenced, the intercalibration
390 precision was estimated to be 0.5%-2.2% in EB and 1%-5% in EE [32].

391 Three calibration methods were employed once colliding beam operations began:

- 392 • ϕ symmetry relative calibration between crystals, exploiting the azimuthal sym-
393 metry of CMS
- 394 • π^0 and η relative calibration between crystals, using the diphoton decays of
395 these particles

¹The ADC-GeV scale factors (one for EB and one for EE) are defined such that the sum of fully calibrated and scaled hits in a particular 5×5 cluster of crystals (plus the associated energy deposited in ES) is 50 GeV for a 50 GeV incident unconverted photon [27].

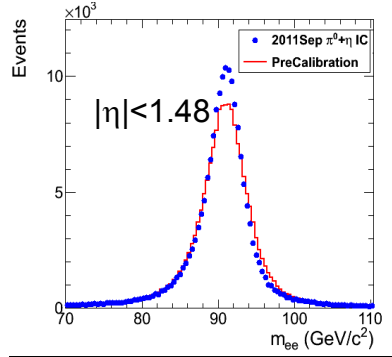


Figure 2.2: Z peak reconstructed using pre-LHC calibration constants (red) or September 2011 π^0/η -derived intercalibration constants (blue). Reprinted from ref. [33].

- 396 • E/p absolute calibration, comparing the momentum measured in the tracker p
 397 to the energy measured in the ECAL E of a sample of electrons from Z decay

398 By September 2011, the intercalibration precision in EB was measured to be be-
 399 tween 0.3% and 1.1% using the π^0/η method [33]. Figure 2.2 shows the improvement
 400 in Z reconstruction from pre-LHC calibration constants to the latest π^0/η -derived
 401 constants.

402 **Calibrated ES Hits**

Added

403 ES calibrated hits are formed from the three samples read out per sensor. Just as in the paren-
 404 case of EB/EE crystals, ES uncalibrated hits gain-adjusted, pedestal-subtracted, and thetical
 405 reconstructed using weights. To make a calibrated ES hit, intercalibration constants, remark
 406 angle correction constants (for the non-uniformity of sensor angle with respect to the
 407 vertical across ES), and a MIP-GeV absolute scale factor are applied.

408 **Clustering**

409 After calibrated ECAL hits are formed, they must be clustered into shapes that
 410 represent the energy deposit from a single particle. *Basic clusters* are formed around
 411 seed hits, defined as a hit that

- 412 • has calibrated $E_T > 1(0.18)$ GeV in EB(EE),
- 413 • does not originate from a dead channel or one with faulty hardware,
- 414 • is not poorly calibrated,
- 415 • was reconstructed with the standard algorithm (i.e. not a special recovery algo-
- 416 rithm for channels with subpar data integrity),
- 417 • is not saturated,
- 418 • is not spike-like, and
- 419 • is in time (EB).

420 EB basic clusters are formed around the seeds via the *hybrid* algorithm, while EE basic
 421 clusters are formed with the `multi5x5` algorithm [34]. In addition to non-radiating
 422 electrons and unconverted photons, both algorithms are designed to also recover all of
 423 the energy associated with electron bremsstrahlung deposits and photon conversions.
 424 The geometry of the CMS magnetic field means that bremsstrahlung and conversions
 425 will tend to spread the shower out in ϕ , not η . Both algorithms work by forming
 426 basic clusters around seeds, then combining the basic clusters into *superclusters* (SC)
 427 by searching in a window extended in the ϕ direction for all basic clusters consistent
 428 with bremsstrahlung radiation from the primary electron, or with a photon conversion.
 429 Figure 2.3 illustrates the hybrid algorithm in EB. In EE, the energy deposited in ES
 430 must also be added into the total clustered energy sum.

431 Figure 2.4 shows the effect of superclustering on $Z \rightarrow ee$ reconstruction.

432 **Supercluster Corrections**

433 The total clustered ECAL energy is defined as

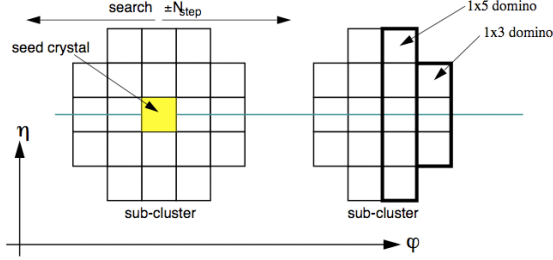


Figure 2.3: Hybrid algorithm in EB. The shower extent is essentially constant in η , but spreads out in ϕ as the two sub-clusters (or basic clusters) are grouped into the same supercluster. Reprinted from ref. [34].

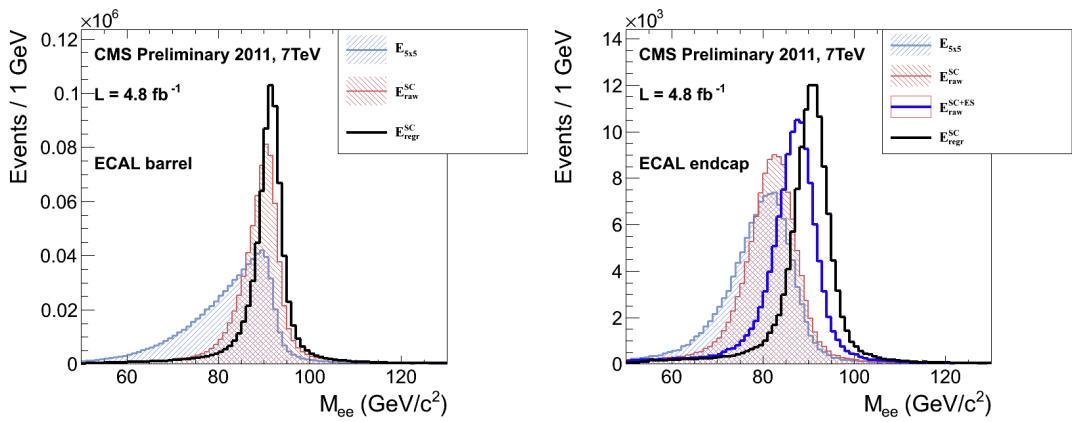


Figure 2.4: Z peak reconstructed in the dielectron channel for different kinds of clustering. The left plot is for EB and the right plot for EE. The constituent hits were calibrated with the best available intercalibrations and laser calibrations as of December 2011. The light blue histogram shows the reconstruction using a 5×5 energy sum, the red histogram shows the reconstruction using the SC energy for crystals only (the dark blue histogram on the right-hand side adds in the energy from ES), and the black histogram shows the reconstruction after the SCs are corrected using a multivariate method [?]. Reprinted from Fig. 30 of ref. [?].

$$E = F \times \sum_{i=1}^{n_{\text{crystal}}} G \times c_i \times A_i \quad (2.1)$$

434 where G is the ADC-GeV or MIP-GeV scale factor, c_i are the intercalibration con-
 435 stants, A_i is the uncalibrated hit amplitude in ADC counts, and F is a SC correction
 436 factor. G and c_i were explained in Sec. 2.1.1. F is a product of three factors for hybrid
 437 SCs (two for multi5x5 SCs) [34]:

- 438 1. $C_{\text{EB}}(\eta)$, which compensates for lateral energy leakage due to the crystal off-
 439 pointing in EB. These corrections are taken from MC simulation [34] and were
 440 confirmed in test beams [29].
- 441 2. $f(\text{brem})$, which corrects for biases in the clustering algorithms for showers char-
 442 acterized by differing amounts of bremsstrahlung. These corrections are taken
 443 from MC simulation [34].
- 444 3. Residual correction $f(E_T, \eta)$, due to the variation in η of detector material
 445 traversed by a primary electron or photon, and to any residual E_T dependence
 446 of the reconstruction. These corrections are determined from MC and validated
 447 on $Z \rightarrow ee$ data samples [35].

Changed

448 As a benchmark of ECAL calibration performance, the extra energy smearing in
 449 MC needed to achieve data/MC agreement in the Z width was between $\sim 0.9\%$ (in
 450 the central part of EB for electrons with little bremsstrahlung) and $\sim 3.3\%$ (in the
 451 outer part of EE for heavily radiating electrons) [36].

452 From Supercluster to Photon

453 The CMS photon object is any SC with $E_T > 10$ GeV and $H/E < 0.5$, unless the SC
 454 $E_T > 100$ GeV, in which case the H/E requirement is dropped. H/E is defined as the

455 ratio of energy in the HCAL in a 0.15 cone around the SC centroid, directly behind
 456 the SC, to the SC energy. SCs with $R9 > 0.94(0.95)$ in EB(EE), where $R9$ is defined
 457 as the ratio of the energy in the central 3×3 cluster of crystals divided by the SC
 458 energy $E_{3 \times 3}/E_{\text{SC}}$, are the best calibrated and most accurate type of electromagnetic
 459 shower. Therefore, for these objects, the photon energy is defined as the energy sum
 460 of the fully calibrated hits in the central 5×5 cluster around the seed (with $C_{\text{EB}}(\eta)$
 461 applied for EB photons). For all other SCs, the photon energy is equal to the fully
 462 corrected SC energy (cf. Sec. 2.1.1).

Reorganized

463 In this search, candidate photons and *fake photons* (f , “fakes”) are further selected next 3
 464 according to the criteria listed in Table 2.1. Fakes are used in the determination of para-
 465 the QCD background, as explained in Chapter 3. graphs;

edited
Ta-ble 2.1
caption

Table 2.1: Selection criteria for photons and fakes. “Pixel seed,” I_{comb} , and $\sigma_{i\eta i\eta}$ are defined in the text.

Variable	Cut (γ)	Cut (f)
SC $ \eta $	< 1.4442	< 1.4442
H/E	< 0.05	< 0.05
$R9$	< 1	< 1
Has pixel seed	No	No
$I_{\text{comb}}, \sigma_{i\eta i\eta}$	$< 6 \text{ GeV} \&\& < 0.011$	$(\geq 6 \&\& < 20 \text{ GeV}) \parallel \geq 0.011$

Updated
effective
area

466 I_{comb} is defined as

$$I_{\text{comb}} = I_{\text{ECAL}} - 0.093\rho + I_{\text{HCAL}} - 0.0281\rho + I_{\text{track}} \quad (2.2)$$

467 where I_{ECAL} , I_{HCAL} , and I_{track} are E_T sums in the annular regions defined in Figure 2.5
 468 and ρ is the average pileup energy density in the calorimeters (per unit $\eta \cdot \phi$) as
 469 measured with the Fastjet algorithm [37, 38]. Note that the ECAL and track isolation
 470 veto strips at constant η ensure that the isolation cuts are similarly efficient for
 471 converted photons, radiating electrons, and unconverted photons.

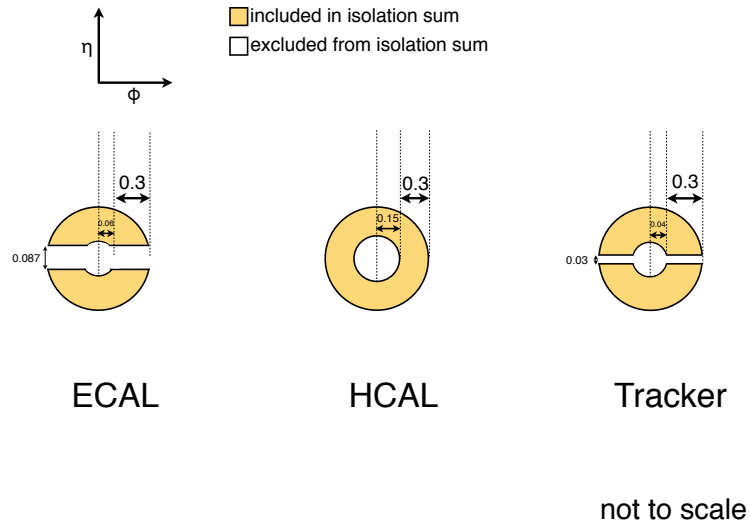


Figure 2.5: ECAL, HCAL, and track Isolation cones.

472 $\sigma_{i\eta i\eta}$ is the log energy weighted extent of the shower in η and is defined as

Added

$$\sigma_{i\eta i\eta} = \frac{\sum_{i=1}^{25} w_i (\eta_i - \bar{\eta})^2}{\sum_{i=1}^{25} w_i} \quad (2.3)$$

$\sigma_{i\eta i\eta}$

defini-
tion

473 where the sums run over the 5×5 matrix of crystals surrounding the seed, $w_i =$
474 $\max(0, 4.7 + \ln(E_i/E))$, E_i is the energy of the i^{th} crystal, E is the total energy in the
475 25 crystals, η_i is the offset in η of the i^{th} crystal from the seed, and $\bar{\eta}$ is the weighted
476 average η of the 25 crystals (using the w_i as weights) [39].

Changed

477 Figure 2.6 shows the ρ distribution for a sample of two-photon events, with at least one 40 GeV and one 25 GeV photon, passing the selection requirements in Table 2.1 and the trigger requirements in Table 2.3. This sample represents the full 2011 dataset of 4.7 fb^{-1} . Since the average ρ is $\sim 7.5 \text{ GeV}$, and there is a long tail above this average value, it is necessary to subtract pileup energy from the ECAL and HCAL isolation cones to recover otherwise clean photons in events with large pileup. The ECAL and HCAL *effective areas* of 0.093 and 0.0281, respectively, are

average

ρ ; up-

dated

fig. 2.6

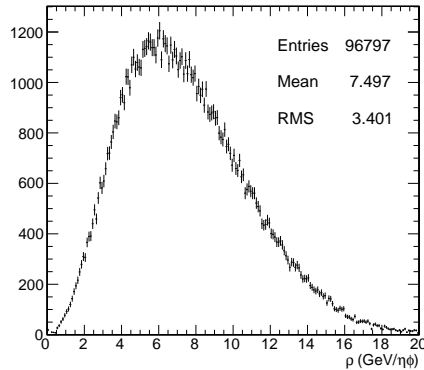


Figure 2.6: ρ distribution for a sample of two-photon events, with at least one 40 GeV and one 25 GeV photon, passing the selection requirements in Table 2.1 and the trigger requirements in Table 2.3. This sample covers the full 2011 dataset of 4.7 fb^{-1} .

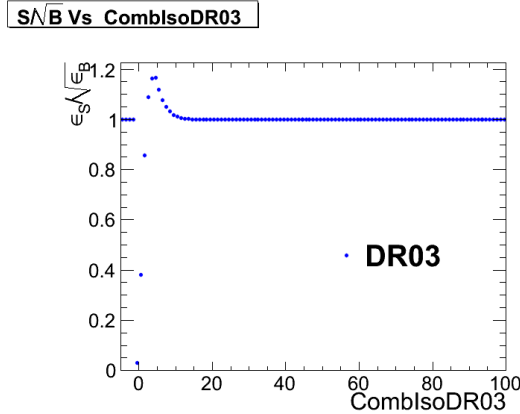


Figure 2.7: S/\sqrt{B} (S and B defined in the text) vs. combined isolation. Reprinted from Fig. 7 of ref. [40].

484 calculated by fitting the average ECAL or HCAL isolation energy vs. ρ in a sample
 485 of $Z \rightarrow ee$ events to a straight line. The slope of the line—which has the units of $\eta \cdot \phi$,
 486 or area—is the effective area.

New

487 The cut on combined isolation of 6 GeV (Table 2.1) is the result of an S/\sqrt{B}
 488 optimization procedure [40]. S is a sample of photons in simulated GGM events that
 489 are products of neutralino decay, while B is a sample of photons matched to generated
 490 hadronic jets in simulated QCD events. Figure 2.7 shows the value of S/\sqrt{B} vs.
 491 combined isolation, in particular the pronounced peak around 6 GeV.

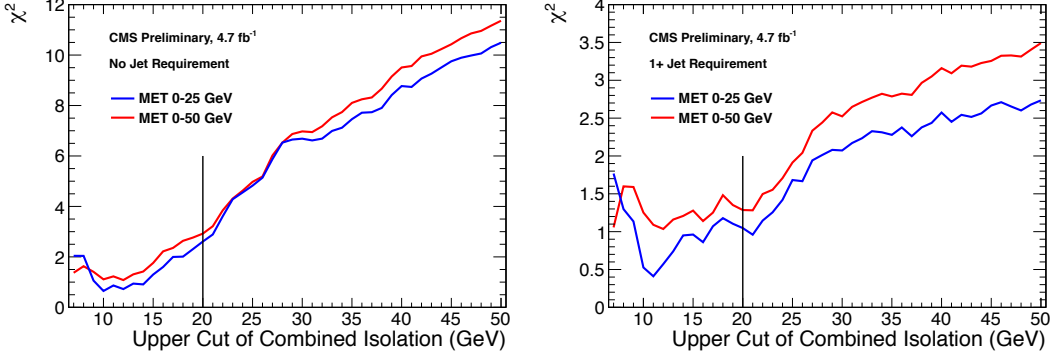


Figure 2.8: Neyman’s χ^2 between the ff and $\gamma\gamma$ \cancel{E}_T distributions, truncated at either 25 (red) or 50 (blue) GeV, vs. upper bound on fake combined isolation. The left plot includes all events; the right plot is for events with ≥ 1 jet defined as in Table 2.2, but with the ΔR cleaning criteria applied to the two primary EM objects and all additional electrons, photons, and fake photons. The full reweighting and normalization procedure is employed in the \cancel{E}_T calculation (see Sec. 3.1). Error bars include statistical, reweighting, and normalization error (see Sec. 3.3). Reprinted from Fig. 9 of ref. [40].

492 The upper bound on fake photon combined isolation guarantees that poorly iso-
 493 lated dijet events, with \cancel{E}_T resolution dissimilar to the candidate diphoton events,
 494 do not enter the ff sample. The exact value of 20 GeV (cf. Table 2.1) arises from
 495 a low- \cancel{E}_T $ff/\gamma\gamma$ χ^2 optimization procedure [40]. Figure 2.8 shows the value of the
 496 Neyman’s χ^2 between the ff and $\gamma\gamma$ \cancel{E}_T distributions, truncated at either 25 or 50
 497 GeV, vs. upper bound on fake combined isolation. As shown in the figure, 20 GeV
 498 very nearly minimizes the χ^2 , while also being large enough that a sufficient number
 499 of ff events may be collected.

500 Finally, a “pixel seed” is defined as a hit in the pixel detector consistent with a
 501 track extrapolated from the position of the ECAL SC back to the primary vertex.
 502 Real photons, having no charge and therefore no bending in the magnetic field, should
 503 not have a pixel seed.

504 **2.1.2 Electrons**

505 Electrons are reconstructed identically to photons, except that in the electron case
 506 the presence of a pixel seed is enforced, rather than vetoed.² Photons and electrons
 507 are defined by very similar criteria so that $Z \rightarrow ee$ events can be used to model
 508 the QCD background in the two-photon sample without introducing any bias in the
 509 electron energy measurement (cf. Sec. 3.1).

510 **2.1.3 Jets and Missing Transverse Energy**

511 **Particle Flow**

512 In this analysis, jets and \cancel{E}_T are formed from *particle flow* (PF) candidates. The parti-
 513 cle flow algorithm [44, 45] uses information from all CMS subdetectors to reconstruct
 514 as accurately as possible the positions and momenta of all visible jet constituents,
 515 exploiting the fine granularity of the tracker and ECAL to achieve a greatly improved
 516 momentum resolution over calorimeter-only jets [46]. The PF algorithm is summa-
 517 rized below [47].

518 1. Reconstruct the fundamental detector objects via iterative procedures

- 519 • Tracks in the inner silicon layers
 - 520 – High efficiency and low fake rate for charged hadrons in jets
 - 521 – Relaxed primary vertex constraint allows photon conversions, parti-
 522 cles originating from nuclear interactions in the silicon, and long-lived
 523 particles to be reconstructed
- 524 • Calorimeter clusters
- 525 • Muon tracks in the outer muon layers

²In many CMS analyses, electrons are reconstructed very differently from photons. In particular, a special tracking algorithm [43] is used to best follow a radiating electron. However, in this analysis, the electron tracking is not used.

526 2. Create a “block” of linked fundamental objects

- 527 • Link silicon tracks to calorimeter clusters via $\Delta R_{\text{track-cluster}}$ (account for
528 electron bremsstrahlung)
- 529 • Link clusters in one calorimeter layer to clusters in a separate layer via
530 $\Delta R_{\text{cluster-cluster}}$
- 531 • Link silicon tracks to muon tracks via global track χ^2

532 3. ID the particles in the block

- 533 • If global (silicon + muon layers) muon p_T is compatible with silicon track
534 p_T , ID as a muon and remove corresponding tracks from block
- 535 • ID electron tracks via special algorithm and removed all corresponding
536 tracks and cluster from block
- 537 • Remove fake tracks from the block Fixed
- 538 • Remove excess track-cluster links via $\Delta R_{\text{track-cluster}}$ minimization (but al-
539 low multiple tracks to be associated to one cluster) typo
- 540 • If the cluster energy is significantly larger then the energy of the linked
541 track, ID as a PF photon or PF neutral hadron and remove corresponding
542 clusters from the block
- 543 • If the cluster is not linked to a track, ID as a PF photon or PF neutral
544 hadron and remove corresponding clusters from the block
- 545 • Remaining track-cluster links are PF charged hadrons

546 Jets

547 PF candidates are clustered into jets by means of the anti- k_T algorithm with $R = 0.5$
548 [48]. In this algorithm, all possible pairs of PF candidates i, j are looped over, and
549 the momenta of the pair that minimize the distance variable

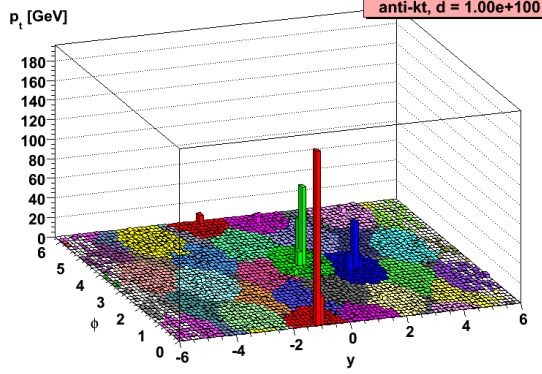


Figure 2.9: Example event display showing jets clustered via the anti- k_T algorithm. y is pseudorapidity.

$$d_{ij} = \frac{\Delta R_{ij}^2}{R^2 \max(k_{Ti}^2, k_{Tj}^2)} \quad (2.4)$$

are combined, where k_{Ti} is the transverse momentum of “combined” PF candidate i .
 550 The constituent PF candidates are clustered together. The process is repeated until
 551 $d_{ij} > 1/k_{Ti}^2$ for all pairs of clustered PF momenta [49]. An illustration is given in Fig-
 552 ure 2.9. The anti- k_T algorithm is infrared and collinear safe, leading to well-behaved
 553 theoretical predictions and ease of comparison between data and MC simulation. It
 554 also tends to form circular jets, making it easy for experimental effects such as ex-
 555 pected out-of-cone energy and fiducial acceptance to be measured or simulated. For
 556 these reasons, the anti- k_T jet clustering algorithm was chosen for this analysis.
 557

Once jets are clustered, they must be corrected for biases in the energy mea-
 558 surement due to non-compensation [50], invisible energy (lost to overcoming nuclear
 559 binding energy, in neutrinos, or in unclustered muons, for example) [50], detector
 560 geometry and cracks [51], zero suppression and trigger inefficiencies [52], pileup, and
 561 effects of the clustering algorithm [51]. Four multiplicative correction factors are ap-
 562 plied to the raw jet four-momentum p_μ^{raw} [46]:
 563

- 564 • $C_{\text{offset}}(p_T^{\text{raw}})$, which accounts for extra energy due to noise, pileup, and the un-

565 derlying event;

- 566 • $C_{\text{MC}}(C_{\text{offset}}p_T^{\text{raw}}, \eta)$, which is derived from MC and accounts for most of the p_T
567 and η dependence;
- 568 • $C_{\text{rel}}(\eta)$, which accounts for the remaining differences in uniformity over the
569 entire calorimeter between data and MC; and
- 570 • $C_{\text{abs}}(C_{\text{rel}}C_{\text{MC}}C_{\text{offset}}p_T^{\text{raw}})$, which accounts for the remaining differences in linear-
571 ity over the full p_T range between data and MC.

572 Figure 2.10 shows the total jet energy correction factor $C_{\text{offset}}C_{\text{MC}}C_{\text{rel}}C_{\text{abs}}$ vs. η
573 for jets reconstructed with the anti- k_T algorithm, $R = 0.5$. The PF jet corrections
574 are more uniform across η than those of CALO jets (composed of simple calorimeter
575 towers) or JPT jets (Jet Plus Tracks; composed of calorimeter energies replaced,
576 where possible, with matching track p_T) [53]. In addition, for p_T in the range 30-200
577 GeV and $|\eta|$ up to 2.0, the PF jet energy correction uncertainty is lower than that of
578 the other two types of jets, and never exceeds $\sim 3\%$ [46]. The superior performance
579 of PF jets motivates their use in this search.

580 In this analysis, candidate and QCD control events are binned by number of jets
581 satisfying the criteria in Table 2.2.

582 Missing Transverse Energy

583 To be consistent with the jet reconstruction, \cancel{E}_T in this analysis is also reconstructed
584 from PF candidates. Raw \cancel{E}_T is defined as

$$\cancel{E}_{T\text{raw}} = \left| - \sum_{i=1}^{n_{\text{PF}}} \vec{p}_{Ti} \right| \quad (2.5)$$

Table 2.2: Definition of HB/HE hadronic jets.

Variable	Cut
Algorithm	L1FastL2L3Residual corrected PF
p_T	$> 30 \text{ GeV}$
$ \eta $	< 2.6
Neutral hadronic energy fraction	< 0.99
Neutral electromagnetic energy fraction	< 0.99
Number of constituents	> 1
Charged hadronic energy	$> 0.0 \text{ GeV}$ if $ \eta < 2.4$
Number of charged hadrons	> 0 if $ \eta < 2.4$
Charged electromagnetic energy fraction	< 0.99 if $ \eta < 2.4$
ΔR to nearest PF electron ^a , muon ^b , or one of the two primary EM objects	> 0.5

^aA PF electron is defined as an electron reconstructed with the PF algorithm [41] with $p_T > 15 \text{ GeV}$, $|\eta| < 2.6$, and $(I_{\text{charged}} + I_{\text{photon}} + I_{\text{neutral}})/p_T < 0.2$, where $I_{\text{charged}}(I_{\text{photon}})(I_{\text{neutral}})$ is the sum of PF charged hadron(PF photon)(PF neutral hadron) momenta in a $\Delta R = 0.4$ cone around the PF electron.

^bMuons are reconstructed [42] from a combination of muon station and inner tracker hits. Here, a muon must have track $\chi^2 < 10$, at least one good muon station hit, inner track transverse impact parameter $< 0.02 \text{ cm}$, inner track longitudinal impact parameter $< 0.5 \text{ cm}$, $p_T > 15 \text{ GeV}$, $|\eta| < 2.6$, and $(I_{\text{ECAL}} + I_{\text{HCAL}} + I_{\text{track}})/p_T < 0.2$, where $I_{\text{ECAL}}(I_{\text{HCAL}})(I_{\text{track}})$ is the sum of ECAL(HCAL)(track) momenta in a $\Delta R = 0.3$ cone around the muon.

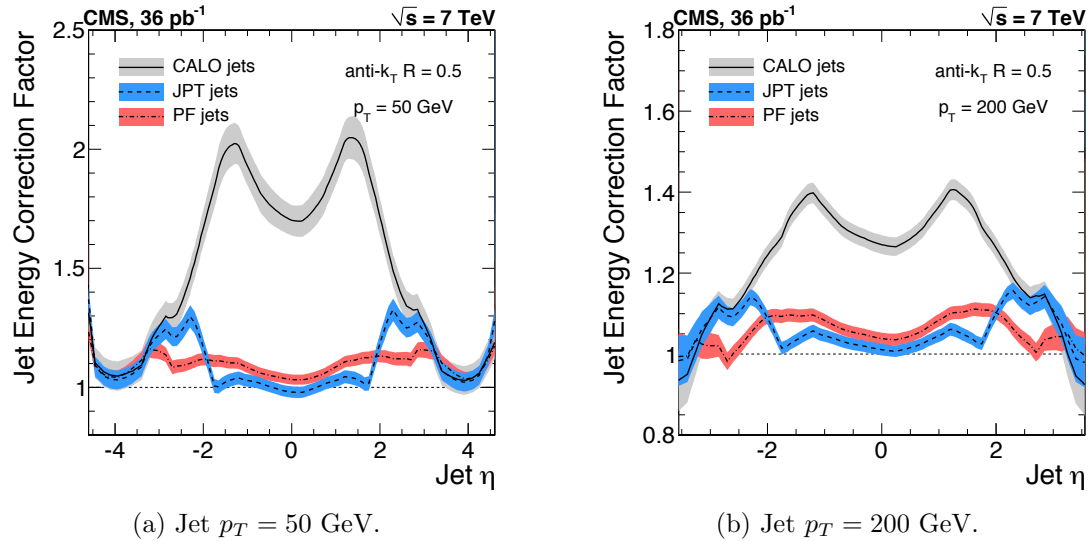


Figure 2.10: Total jet energy correction factor $C_{\text{offset}}C_{\text{MC}}C_{\text{rel}}C_{\text{abs}}$ vs. η , including uncertainty band, for jets reconstructed with the anti- k_T algorithm, $R = 0.5$. Reprinted from Fig. 26 of ref. [46].

where n_{PF} is the number of PF candidates in the event. \cancel{E}_{Raw} may be corrected for the same effects that necessitate jet corrections, since \cancel{E}_{Raw} is usually the result of jet mis-measurement (except, of course, in electroweak physics processes that include an energetic neutrino, or SUSY production). CMS *Type-I* \cancel{E}_T corrections simply involve replacing the PF jets with their corrected energies (cf. Sec 2.1.3) and recalculating \cancel{E}_T . Only jets with *electromagnetic fraction* (EMF) below 90% and $p_T > 20$ GeV are replaced. This ensures that very electromagnetic jets (as well as isolated leptons, which also receive no correction), which consist chiefly of neutral pions and are measured accurately by the ECAL, do not receive a correction derived for jets with a large fraction of their energy in charged hadrons. In addition, the p_T cut guarantees that jet corrections are only applied where they are known to within a few percent. For this search, the level of agreement between the SM background estimate and the two-photon search sample in a low- \cancel{E}_T control region is the same regardless of whether the \cancel{E}_T is corrected or not, so for simplicity the Type-I \cancel{E}_T corrections are not used (see Sec. ??).

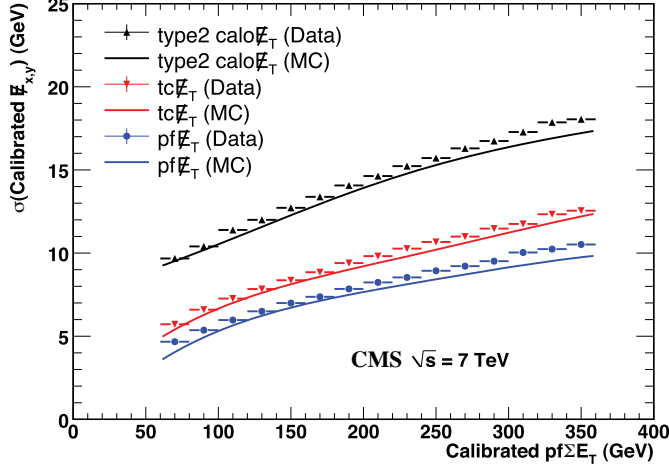


Figure 2.11: σ of a Gaussian fit to the x- and y-components of calibrated E_T vs. the calibrated PF E_T sum in a sample of events containing at least two jets with $p_T > 25$ GeV. σ is calibrated such that the E_T scale is equal for all three algorithms. PF $\sum E_T$ is corrected, on average, to the particle level using a Pythia v8 simulation [54]. The blue markers (data) and line (MC) refer to PF jets. Reprinted from Fig. 13 of ref. [52].

600 Figure 2.11 shows the σ of a Gaussian fit to the x- and y-components of calibrated
 601 E_T vs. the calibrated PF E_T sum in a sample of events containing at least two jets
 602 with $p_T > 25$ GeV. Again, PF E_T outperforms E_T constructed of calorimeter towers
 603 or track-corrected calorimeter deposits.

604 2.2 HLT

605 From the objects described in Sec. 2.1, four samples of events are formed:

- 606 • $\gamma\gamma$ candidate sample, in which the two highest E_T objects are photons,
- 607 • $e\gamma$ control sample, in which the two highest E_T objects are one electron and
 608 one photon,
- 609 • ee control sample, in which the two highest E_T objects are electrons, and
- 610 • ff control sample, in which the two highest E_T objects are fakes.

611 In all samples, the leading EM object is required to have $E_T > 40$ GeV, while the
 612 trailing EM object is required to have $E_T > 25$ GeV. The high level triggers used to
 613 select the four samples, by run range, are listed in Table 2.3. No trigger is prescaled.

Table 2.3: HLT paths triggered by the $\gamma\gamma$, $e\gamma$, ee , and ff samples, by run range. No triggers are prescaled.

Run range	$\gamma\gamma$	$e\gamma$	ee	ff
160404-163261	Photon26_ IsoVL_ Photon18	Photon26_ IsoVL_ Photon18	Photon26_ IsoVL_ Photon18	Photon26_ IsoVL_ Photon18
161216-166967	Photon36_ CaloIdL_ Photon22_ CaloIdL	Photon36_ CaloIdL_ Photon22_ CaloIdL	Photon36_ CaloIdL_ Photon22_ CaloIdL	Photon36_ CaloIdL_ Photon22_ CaloIdL
166347-180252	Photon36_ CaloIdL_ IsoVL_ Photon22_ CaloIdL_ IsoVL	Photon36_ CaloIdL_ IsoVL_ Photon22_ CaloIdL_ IsoVL	Photon36_ CaloIdL_ IsoVL_ Photon22_ R9Id	Photon36_ CaloIdL_ IsoVL Photon36_ CaloIdL_ IsoVL Photon36_ R9Id_ Photon22_ CaloIdL_ IsoVL Photon36_ R9Id_ Photon22_ R9Id

614 Each piece of the HLT path name is defined as follows.

615 • “Photon”: Energy deposit in the ECAL that fired an L1 trigger (cf. Sec. ??).

616 For Photon26_IsoVL_Photon18, the L1 seed E_T threshold is 12 GeV, while for
 617 all other triggers in Table 2.3 it is 20 GeV.

618 • Integer following the word “Photon”: E_T threshold in GeV for offline recon-
 619 structed photon, using the full photon reconstruction of Sec. 2.1.1 minus the
 620 laser calibrations and assuming the primary vertex at (0, 0, 0).

621 • “CaloIdL”: For EB photons, $H/E < 0.15$ and $\sigma_{in\eta} < 0.014$.

622 • “IsoVL”: $I_{ECAL} < 0.012E_T + 6$ GeV, $I_{HCAL} < 0.005E_T + 4$ GeV, and $I_{track} <$
 623 $0.002E_T + 4$ GeV.

624 • “R9Id”: $R9 > 0.8$.

625 In addition, the versions of HLT_Photon26_IsoVL_Photon18 and
 626 Photon36_CaloIdL_Photon22_CaloIdL that were active during runs 160404-163268
 627 included a cut $E_{max}/E_{5\times5} < 0.98$ for spike rejection. E_{max} is the energy in the highest
 628 energy crystal of the EM cluster and $E_{5\times5}$ is the energy in the 5×5 crystal matrix
 629 around the seed crystal. For runs after 163268, Swiss cross spike rejection of individual
 630 crystals from HLT quantities was performed (cf. Sec. 2.1.1). All information about the
 631 evolution of the CMS HLT settings can be found in the HLT configuration browser
 632 at <http://j2eeps.cern.ch/cms-project-confdb-hltdev/browser/>.

633 As an example of the naming convention just described, the HLT path Pho-
 634 ton36_CaloIdL_IsoVL_Photon22_R9Id is fired if one photon is found with $E_T > 36$
 635 GeV passing the CaloIdL and IsoVL requirements, and another is found with $E_T > 22$
 636 GeV passing the R9Id requirement.

637 **Add a discussion of trigger efficiency here, with plots.**

638 2.3 Event Quality

639 To suppress instrumental backgrounds, a set of event quality cuts are applied to the
 640 $\gamma\gamma$, $e\gamma$, ee , and ff samples. First, all events are required to pass a good run selec-
 641 tion, as determined by the CMS Physics Validation Team (<https://twiki.cern.ch/twiki/bin/view/CMS/PVTMain>, CERN computing ID needed). The good run selec-
 642 tion excludes luminosity sections during which a sufficient part of the CMS detector
 643 was unpowered or malfunctioning. Such conditions could occur if, for example, a high
 644 voltage supply trips off in the middle of a run, or a DAQ error corrupts data quality
 645 but is not spotted until after the data have been collected. The severity of a detec-
 646 tor problem is judged by its effect on a wide range of analyses and reconstruction
 647 algorithms. Of the **N** fb^{-1} of integrated luminosity delivered by the LHC in 2011,
 648 4.68 fb^{-1} passed the good run selection. This analysis is performed on the entire 2011
 649 certified dataset.

651 Second, all events must contain at least one good interaction vertex. The criteria
 652 for a good vertex are:

653 • $\chi^2 \neq 0 \parallel \text{ndof} \neq 0 \parallel N_{\text{tracks}} \neq 0$, where χ^2 and ndof are calculated for the track
 654 fit to the vertex, and N_{tracks} is the number of tracks in the vertex fit

655 • $\text{ndof} > 4$

656 • $|z| < 24 \text{ cm}$, where z is the z -coordinate of the vertex position

657 • $|\rho| < 2 \text{ cm}$, where ρ is the transverse displacement of the vertex position from
 658 the beam line

659 The good vertex requirement eliminates non-collision backgrounds such as beam
 660 scraping, beam halo, cosmic muon interactions, and instrumental effects.

661 Third, the two electromagnetic objects in the $\gamma\gamma$, $e\gamma$, ee , and ff events must
 662 be separated in ϕ by at least 0.05. This requirement protects against beam halo

663 bremsstrahlung, in which a halo muon traveling parallel to the beam line radiates
 664 an energetic photon while itself depositing a large amount of energy in the ECAL.
 665 In this case, the two ECAL hits would likely be at the same ϕ (and ρ). An example
 666 cartoon is shown in Figure ???. **Insert figure.**

667 Fourth, the two EM objects must be separated in R by at least 0.6. Since the
 668 isolation cone size used is 0.3, this ensures that the isolation energy of one EM object
 669 cannot be in the veto strip (Fig. 2.5) of the other.

670 Finally, the $\gamma\gamma$, $e\gamma$, ee , and ff events must pass an HCAL noise filter and ECAL
 671 dead channel filter. The HCAL noise filter guarantees that all HCAL reconstructed
 672 hits are inconsistent with any noise source. Noise sources [55] include:

- 673 • Ion feedback in the HPDs absent any true incident photons, in which a thermal
 674 electron ionizes a molecule in the HPD acceleration gap, faking a real signal
- 675 • HPD discharge affecting nearly all channels in the same HPD [56], partially
 676 explained by the effect of the 4 T CMS magnetic field on the flashover voltage
 677 of the dielectric [58]
- 678 • Concurrent signals in nearly all 72 channels of a single RBX, as yet unexplained
- 679 • HF PMT window hits (as opposed to the usual quartz fiber hits)
- 680 • ADC saturation

681 Since HCAL noise may induce fake jets or E_T , events are rejected if any of the
 682 following criteria are true:

- 683 • Any HPD has > 17 hits
- 684 • A single HPD has > 10 hits, but every other HPD has zero hits
- 685 • An RBX has > 10 zero-ADC-count hits

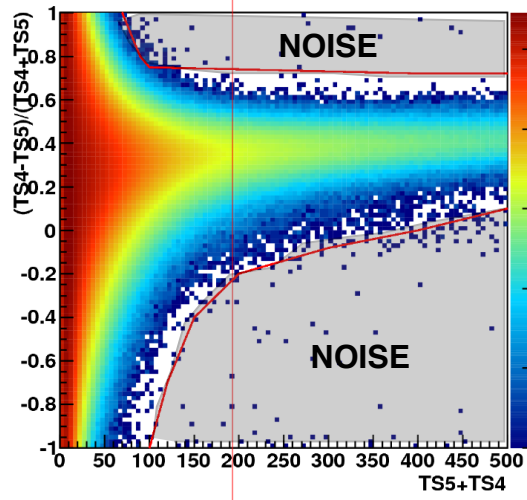


Figure 2.12: $(TS4 - TS5)/(TS4 + TS5)$ vs. $TS4 + TS5$ for a minimum bias sample. HB/HE hits are considered noisy if they lie in the sparsely populated gray region labeled "NOISE" defined by the curved red lines. Adapted from ref. [57].

- 686 • Any HB/HE reconstructed hit corresponding to an RBX with > 50 GeV of
- 687 energy fails a two-dimensional cut defined by the variables $(TS4 - TS5)/(TS4 +$
- 688 $TS5)$ vs. $TS4 + TS5$, where $TS4(TS5)$ is the hit amplitude in the fourth(fifth)
- 689 time sample read out for that hit. The cut is defined in Fig. 2.12.

690 The ECAL dead channel filter is designed to flag events in which significant EM
 691 energy was deposited in a masked region of the ECAL by using the trigger primitive
 692 information for the corresponding trigger tower. Energy deposited in a masked region
 693 of ECAL can cause fake \cancel{E}_T . Events are rejected if the trigger primitive E_T exceeds
 694 the maximum value of 63.75 GeV in any trigger tower that is masked in the readout.

695 **2.4 Photon Identification Efficiency**

696 In order to determine the cross section (or cross section upper limit) for a GGM
 697 signal, the photon identification efficiency is needed. Since no suitably large sample
 698 of $Z \rightarrow \mu\mu\gamma$ events in CMS exists yet, the efficiency calculation relies on the similarity
 699 between detector response to electrons and photons. A scale factor to correct the MC

700 photon ID efficiency to the real photon efficiency for the data is obtained from the
 701 ratio of the electron efficiency from the data to the electron efficiency from MC.

702 The different types of photon ID variables—calorimeter and track isolation, ratio
 703 of hadronic to electromagnetic energy of the shower, and transverse shower shape—
 704 are chosen so that their distributions for isolated electrons and photons are similar.³
 705 Figure ?? shows distributions of photon ID variables for MC electrons and photons,
 706 where a MC electron(photon) is a `reco::Photon` object matched to a generated
 707 electron(photon) originating from a Z decay(the hard interaction) within $\Delta R = 0.3$.
 708 MC electrons come from the DYJets0LL sample, while MC photons come from the
 709 GJet sample (see Appendix A). **Make these plots.** The shapes of the distributions
 710 agree well. **Also include data/MC comparisons?**

711 The photon selection efficiency is

$$\epsilon_\gamma = \epsilon_\gamma^{\text{MC}} \times \frac{\epsilon_e^{\text{data}}}{\epsilon_e^{\text{MC}}} \quad (2.6)$$

712 where

- 713 • ϵ_γ is the photon ID efficiency in data,
- 714 • $\epsilon_\gamma^{\text{MC}}$ is the photon ID efficiency in MC,
- 715 • ϵ_e^{data} is the electron ID efficiency obtained using $Z \rightarrow ee$ electrons in the data
 716 that satisfy the photon ID cuts, and
- 717 • ϵ_e^{data} is the electron ID efficiency obtained using $Z \rightarrow ee$ electrons in MC that
 718 satisfy the photon ID cuts.

719 The ratio $\epsilon_e^{\text{data}}/\epsilon_e^{\text{MC}}$ is defined as the scale factor by which the GGM signal MC
 720 photon ID efficiency must be multiplied to give an estimate of the photon ID efficiency

³ $R9$ differs between photons and radiating electrons, but the requirement $R9 < 1$ is loose enough not to introduce problems with the use of electrons to measure the photon ID efficiency.

721 in data. The photon ID requirements of Table 2.1 plus the IsoVL HLT requirement
 722 described in Sec. 2.2 and Table 2.3 are repeated in Table 2.4.

Table 2.4: Candidate photon ID requirements.

Variable	Cut
I_{ECAL}	$< 0.012E_T + 6 \text{ GeV}$
I_{HCAL}	$< 0.005E_T + 4 \text{ GeV}$
I_{track}	$< 0.002E_T + 4 \text{ GeV}$
H/E	< 0.05
$\sigma_{i\eta i\eta}$	< 0.011
$I_{\text{ECAL}} - 0.0792\rho + I_{\text{HCAL}} - 0.0252\rho + I_{\text{track}}$	$< 6 \text{ GeV}$
$R9$	< 1

723 2.4.1 Tag and Probe Method

724 A *Z tag and probe* method is utilized to measure the efficiency of the photon ID
 725 cuts in Table 2.1. The tag is a well-identified electron. The probe, by contrast, is as
 726 loosely identified as possible, and all tags must pass the probe criteria in addition to
 727 the stringent tag criteria. The tag and probe criteria used in this study are shown in
 728 Table 2.5.

729 The invariant mass of the tag and probe are required to be within a narrow window
 730 around Z mass. Assuming that the probabilities of the tag and probe legs of the Z
 731 decay to pass the photon ID cuts are uncorrelated, the efficiency can be estimated as

$$\epsilon = \frac{N_{\text{tag-pass}}}{N_{\text{tag-pass}} + N_{\text{tag-fail}}} \quad (2.7)$$

732 where $N_{\text{tag-pass}}$ is the number of tag-probe pairs in which the probe leg passes the
 733 photon ID cuts under study and $N_{\text{tag-fail}}$ is the number of tag-probe pairs in which
 734 the probe leg fails the cuts. Implicit in these definitions is a double counting of pairs
 735 in which both electrons pass the tag and probe criteria [59]. In addition, in the rare

Table 2.5: Tag and probe criteria. The superscript 0.4 indicates that the isolation variable was calculated in a cone of $\Delta R = 0.4$ around the photon candidate. The isolations without superscripts use the standard $\Delta R = 0.3$ cones.

Variable	Cut	
	Tag	Probe
RECO object	photon	photon
HLT	HLT_Ele17_CaloIdVT_CaloIsoVT_TrkIdT_-TrkIsoVT_SC8_Mass30_v* (must have fired the 17 GeV leg)	—
H/E	< 0.05	< 0.15
$I_{\text{ECAL}}^{0.4}$	$< 0.006E_T + 4.2 \text{ GeV}$	—
$I_{\text{HCAL}}^{0.4}$	$< 0.0025E_T + 2.2 \text{ GeV}$	—
$I_{\text{track}}^{0.4}$	$< 0.001E_T + 2.0 \text{ GeV}$	—
E_T	$> 25 \text{ GeV}$	—
SC E_T	—	$> 15 \text{ GeV}$
SC $ \eta $	< 1.4442	< 1.4442
$\sigma_{in\eta}$	< 0.009	—
Has pixel seed?	Yes	—
Track match type	General track	—
Track match ΔR	< 0.04	—
Track match p_T	$> 15 \text{ GeV}$	—
Track match $ \eta $	< 1.479	—

736 circumstance (less than 1% in MC [59]) that two or more probes may be matched to
 737 one tag, the pair with invariant mass closest to the Z mass is chosen.

738 In practice, $N_{\text{tag-pass}}$ and $N_{\text{tag-fail}}$ are returned by a simultaneous unbinned maxi-
 739 mum likelihood fit to the invariant mass distributions of tag-pass and tag-fail events,
 740 with appropriate signal and background PDF assumptions. The fit form used is

$$\begin{aligned} f_{\text{tag-pass}}(m_{\text{tag-pass}}) &= \epsilon N_S f_S^{\text{pass}}(m_{\text{tag-pass}}) + N_B^{\text{pass}} f_B^{\text{pass}}(m_{\text{tag-pass}}) \\ f_{\text{tag-fail}}(m_{\text{tag-fail}}) &= (1 - \epsilon) N_S f_S^{\text{fail}}(m_{\text{tag-fail}}) + N_B^{\text{fail}} f_B^{\text{fail}}(m_{\text{tag-fail}}) \end{aligned} \quad (2.8)$$

741 where $f_{\text{tag-pass}}(m_{\text{tag-pass}})$ and $f_{\text{tag-fail}}(m_{\text{tag-fail}})$ are the tag-pass and tag-fail PDFs,
 742 respectively; ϵ is the efficiency; N_S is the total number of Z signal events summed over
 743 both samples; $f_S^{\text{pass}}(m_{\text{tag-pass}})$ and $f_S^{\text{fail}}(m_{\text{tag-fail}})$ are the tag-pass and tag-fail signal
 744 PDFs, respectively; N_B^{pass} and N_B^{fail} are the numbers of background events in the tag-
 745 pass and tag-fail samples, respectively; and $f_B^{\text{pass}}(m_{\text{tag-pass}})$ and $f_B^{\text{fail}}(m_{\text{tag-fail}})$ are the
 746 tag-pass and tag-fail background PDFs, respectively. This particular implementation
 747 of the tag and probe methodology is based on tag CMSSW_4_2_5 of the CMSSW
 748 package PhysicsTools/TagAndProbe, and uses the MINUIT2 [60] library, as coded
 749 in RooFit [61], for the likelihood maximization. For this study, CMSSWv4.2.8 was
 750 used.

751 For both samples, the signal shape is assumed to be a Crystal Ball function [62]
 752 convoluted with the Z generated lineshape, while the background shape is a PDF that
 753 describes the falling background as well as the kinematic turn-on at low invariant
 754 mass. The background PDF, called ‘‘RooCMSShape’’ [59], is given by

$$\text{RooCMSShape}(x) = \begin{cases} 1e20 & \text{for } (x - \mu)\gamma < -70 \\ 0 & \text{for } (x - \mu)\gamma > 70 \\ \text{erfc}((\alpha - x)\beta) \exp(-(x - \mu)\gamma) & \text{otherwise} \end{cases} \quad (2.9)$$

where α , β , γ , and μ are parameters of the fit, most of which are held fixed. In the three lowest E_T bins, all parameters of the tag-pass and tag-fail background PDFs are left floating, because the effect of the relaxed E_T cuts has a significant effect on the background shape. More details of the signal and background PDFs are given in Table 2.6. The fixed signal and background parameter values were determined by fitting a small sample ($0.0 \leq \eta < 0.25$) of Fall11 MC signal (DYJetsToLL) and background (QCD_Pt-20to30_BCtoE, QCD_Pt-30to80_BCtoE, QCD_Pt-80to170_BCtoE, GJet_Pt-20_doubleEMEnriched, WJetsToLNu, TTJets) with parameters left floating.

Some fit examples are shown in Figures ?? and ???. In Fig. ??, which shows fits to data and MC for $15 \text{ GeV} \leq \text{probe } E_T \leq 20 \text{ GeV}$, the kinematic turn-on is below the invariant mass range covered by the plot. The exponentially falling background is easily seen underneath the signal, and is especially pronounced in the background-dominated tag-fail sample. **Include these plots.**

2.4.2 Photon Efficiency Scale Factor $\epsilon_e^{\text{data}}/\epsilon_e^{\text{MC}}$

Figure 2.13 shows the dependence of the photon ID efficiency scale factor $\epsilon_e^{\text{data}}/\epsilon_e^{\text{MC}}$ on E_T , η , $\Delta R_{\gamma\text{jet}}$, and N_{jet} , where jets are defined as in Sec. 3.5.2 ([insert reference to “Jet Selection” section here](#)). **$\Delta R_{\gamma\text{jet}}$ plot will be added during second round.** Errors are statistical only. For the plot of the scale factor vs. $\Delta R_{\gamma\text{jet}}$, only events with ≥ 1 jets are included. There is no significant dependence of the scale factor on these variables, so only one scale factor is computed from the entire dataset.

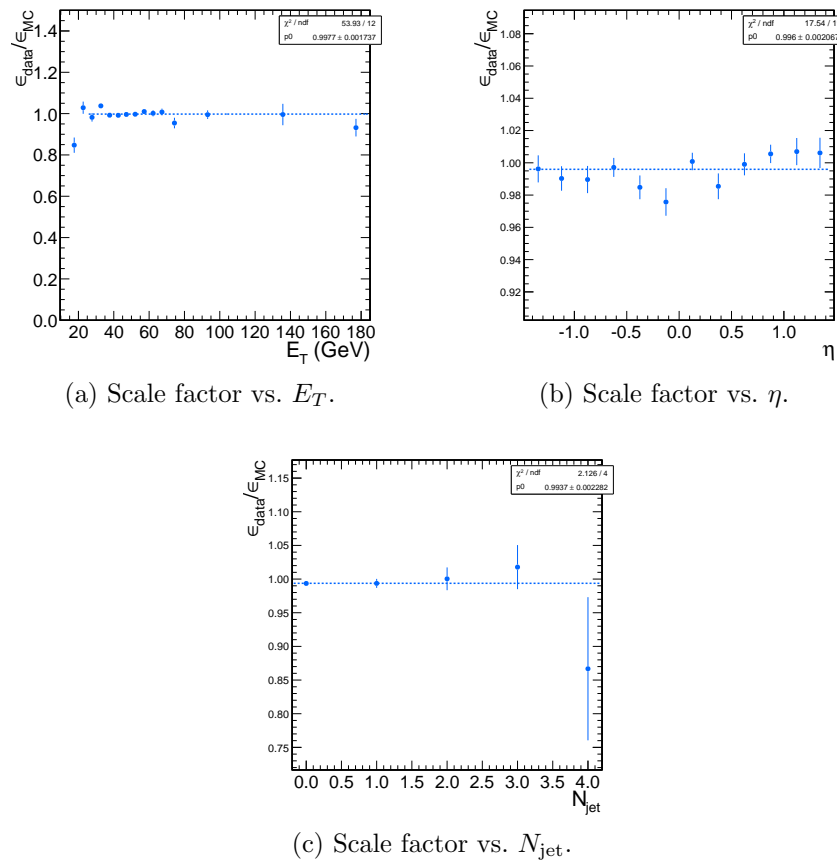


Figure 2.13: Dependence of the photon ID efficiency scale factor on some kinematic variables. Errors are statistical only.

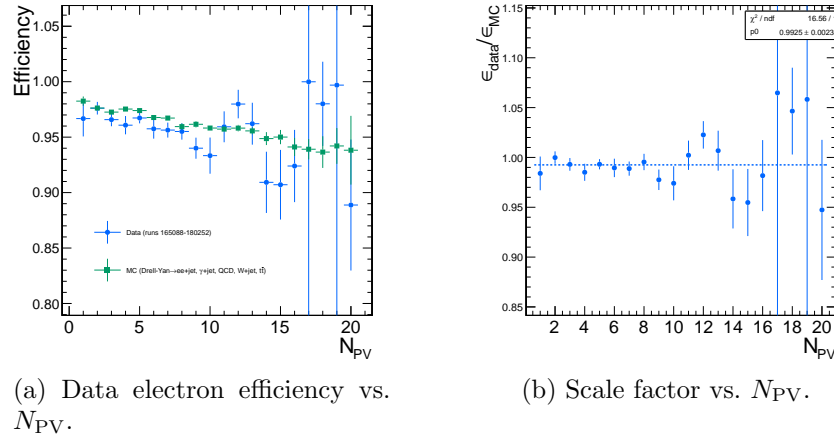


Figure 2.14: Dependence of the photon ID efficiency scale factor on the number of primary vertices per event. Errors are statistical only.

The effect of pileup is studied by comparing the efficiencies ϵ_e^{data} and ϵ_e^{MC} vs. the number of primary vertices (N_{PV}) in the event. The efficiency drops for events with large N_{PV} , even after using pileup-corrected isolation cuts, as can be seen in Figure 2.14a. However, the MC tracks the data, and the scale factor is flat vs. N_{PV} , as shown in Fig. 2.14b.

The scale factor is measured to be $\epsilon_e^{\text{data}}/\epsilon_e^{\text{MC}} = 0.994 \pm 0.002(\text{stat.}) \pm ?(\text{syst.})$. Four main sources of systematic error, in addition to the statistical error of 0.2%, were studied.

Different behavior of electrons and photons in MC Even though the photon ID cuts are designed to be similarly efficient for both electrons and photons, there might be a small difference in the performance between the two kinds of particles, e.g. because of electron bremsstrahlung. To check this effect, the MC electron ID efficiency was calculated using a $Z \rightarrow ee$ sample and the MC photon ID efficiency was calculated using a $\gamma + \text{jets}$ sample. Both samples were reconstructed in CMSSWv3.6. Half the difference between these two results, 0.5%, was taken as an error on the scale factor. **This result is now out of date because it used an older selection. Should this check be redone?**

792 **Pileup** To account for the possibility that the MC simulation may not adequately
 793 reproduce the data in a high pileup environment, the data/MC scale factor
 794 for events with 1-4 good reconstructed primary vertices was calculated, along
 795 with the same for events with ≥ 7 good reconstructed primary vertices. This
 796 particular division of the data was chosen because the pileup distribution in
 797 data peaks at ~ 7 primary vertices per event. The difference between the scale
 798 factors from both samples, ?, was taken as an error on the scale factor from
 799 pileup.

800 **Signal fit over/underestimation** It was found that the signal fit slightly under-
 801 estimates the data in the tag-pass sample, and slightly overestimates it in the
 802 tag-fail sample. To cover this effect with a systematic error, the efficiencies in
 803 data and MC, and then the scale factor, were recalculated using the background
 804 (from fit) subtracted integrals of the tag-pass and tag-fail distributions, rather
 805 than the fitted signal yields in those distributions. The difference between the
 806 scale factor found in this way and the nominal scale factor, ?, was taken as an
 807 error on the scale factor. **Not sure this is a problem anymore.**

808 **Signal and background shape assumption** The largest source of systematic er-
 809 ror comes from the signal and background shape assumptions. To assess the
 810 magnitude of this error, the tag-pass and tag-fail tail parameters (Crystal Ball
 811 ? and n) were varied by $\pm 1\sigma$, and the background shape was varied between
 812 “RooCMSShape, exponential, power law, and quadratic. All possible combi-
 813 nations of varied parameters were generated, and the data and MC were refit
 814 and new scale factors generated according to those combinations. The error was
 815 taken as the largest deviation of the scale factor from nominal, ?%. **Also, in**
 816 **many bins, there is zero background fitted under the tag-pass peak.**
 817 **Background is a small effect here anyway, but we should get a sys-**

818 tematic for this somehow.

819 Add in a MC estimate of the pixel veto efficiency with varied tracker
820 geometries.

Table 2.6: Parameter values for the signal and background PDFs for the different samples. The background PDF applies to all efficiency bins except the four lowest E_T bins, which use a floating RooCMSShape background. When a bracketed range is given, the parameter is allowed to float within that range. When a constant is given, the parameter is fixed to that constant.

PDF	Crystal Ball fit parameters				RooCMSShape fit parameters			
	μ	σ	α	n	μ	α	β	γ
Tag-pass signal	[-1.0, 1.0]	[1.0, 3.0]	0.87	97.0	N/A	N/A	N/A	N/A
Tag-fail signal	[-1.0, 1.0]	[1.0, 3.0]	0.73	134.9	N/A	N/A	N/A	N/A
Tag-pass background	N/A	N/A	N/A	N/A	65.0	61.949	0.04750	0.01908
Tag-fail background	N/A	N/A	N/A	N/A	α	[50.0, 100.0]	0.065	0.048

821

Chapter 3

822

Data Analysis

823 The signature of GGM SUSY particle production in this search is an excess of two-
824 photon events with high \cancel{E}_T . \cancel{E}_T is reconstructed using the particle flow algorithm
825 as described in Sec. 2.1.3. Candidate two-photon events, as well as control events,
826 are selected according to the offline object criteria presented in Secs. 2.1.1, 2.1.2,
827 and 2.1.3; the event quality criteria in Sec. 2.3; and the trigger requirements in Sec. 2.2.
828 These are summarized in Table 3.1.

Table 3.1: Selection criteria for $\gamma\gamma$, $e\gamma$, ee , and ff events.

Variable	Cut			
	$\gamma\gamma$	$e\gamma$	ee	ff
HLT match	IsoVL	IsoVL	IsoVL	IsoVL R9Id
E_T	$> 40/ > 25 \text{ GeV}$			
$\text{SC } \eta $	< 1.4442	< 1.4442	< 1.4442	< 1.4442
H/E	< 0.05	< 0.05	< 0.05	< 0.05
$R9$	< 1	< 1	< 1	< 1
Pixel seed	No/No	Yes/No	Yes/Yes	No/No
I_{comb} , $\sigma_{inj\eta}$	$< 6 \text{ GeV} \&& < 0.011$	$< 6 \text{ GeV} \&& < 0.011$	$< 6 \text{ GeV} \&& < 0.011$	$< 20 \text{ GeV} \&& (\geq 6 \text{ GeV} \parallel \geq 0.011)$
JSON	Yes	Yes	Yes	Yes
No. good PVs	≥ 1	≥ 1	≥ 1	≥ 1
ΔR_{EM}	> 0.6	> 0.6	> 0.6	> 0.6
$\Delta\phi_{\text{EM}}$	≥ 0.05	≥ 0.05	≥ 0.05	≥ 0.05

829 This search utilizes 4.7 fb^{-1} of CMS data collected during the period April
 830 December 2011, corresponding to the following datasets [63]:

- 831 • /Photon/Run2011A-05Jul2011ReReco-ECAL-v1/AOD
- 832 • /Photon/Run2011A-05Aug2011-v1/AOD
- 833 • /Photon/Run2011A-03Oct2011-v1/AOD
- 834 • /Photon/Run2011B-PromptReco-v1/AOD

835 The search strategy is to model the backgrounds to the GGM SUSY signal using
 836 \cancel{E}_T shape templates derived from the control samples, and then to look for a high- \cancel{E}_T
 837 excess above the estimated background in the $\gamma\gamma$ sample. There are two categories
 838 of backgrounds: QCD processes with no real \cancel{E}_T and electroweak processes with real
 839 \cancel{E}_T from neutrinos. The relevant QCD background processes are multijet production
 840 with at least two jets faking photons, photon + jet production with at least one jet
 841 faking a photon, and diphoton production, and Z production with a radiated photon
 842 where at least one of the Z decay products (typically a jet) fakes a photon. The
 843 relevant electroweak background processes, which are small compared to the QCD
 844 background, involve $W \rightarrow e\nu$ decay with a recoiling jet that fakes a photon or a
 845 real radiated photon (the W may come from the decay of a top quark in $t\bar{t}$ events).
 846 In both cases, the electron is misidentified as a photon due to a small inefficiency
 847 in reconstructing the electron pixel seed. The main diagrams contributing to the
 848 QCD(electroweak) backgrounds are shown in Figure 3.1(3.2).

849 Data control samples are used to model all of the backgrounds. The primary
 850 control sample used to model the QCD background is the ff sample, which is similar
 851 to the candidate $\gamma\gamma$ sample but with combined isolation or $\sigma_{inj\eta}$ cuts inverted. The cuts
 852 on these variables are used to distinguish between photons and jets, so by inverting
 853 those cuts, the resulting ff sample becomes enriched with QCD dijets. Because the

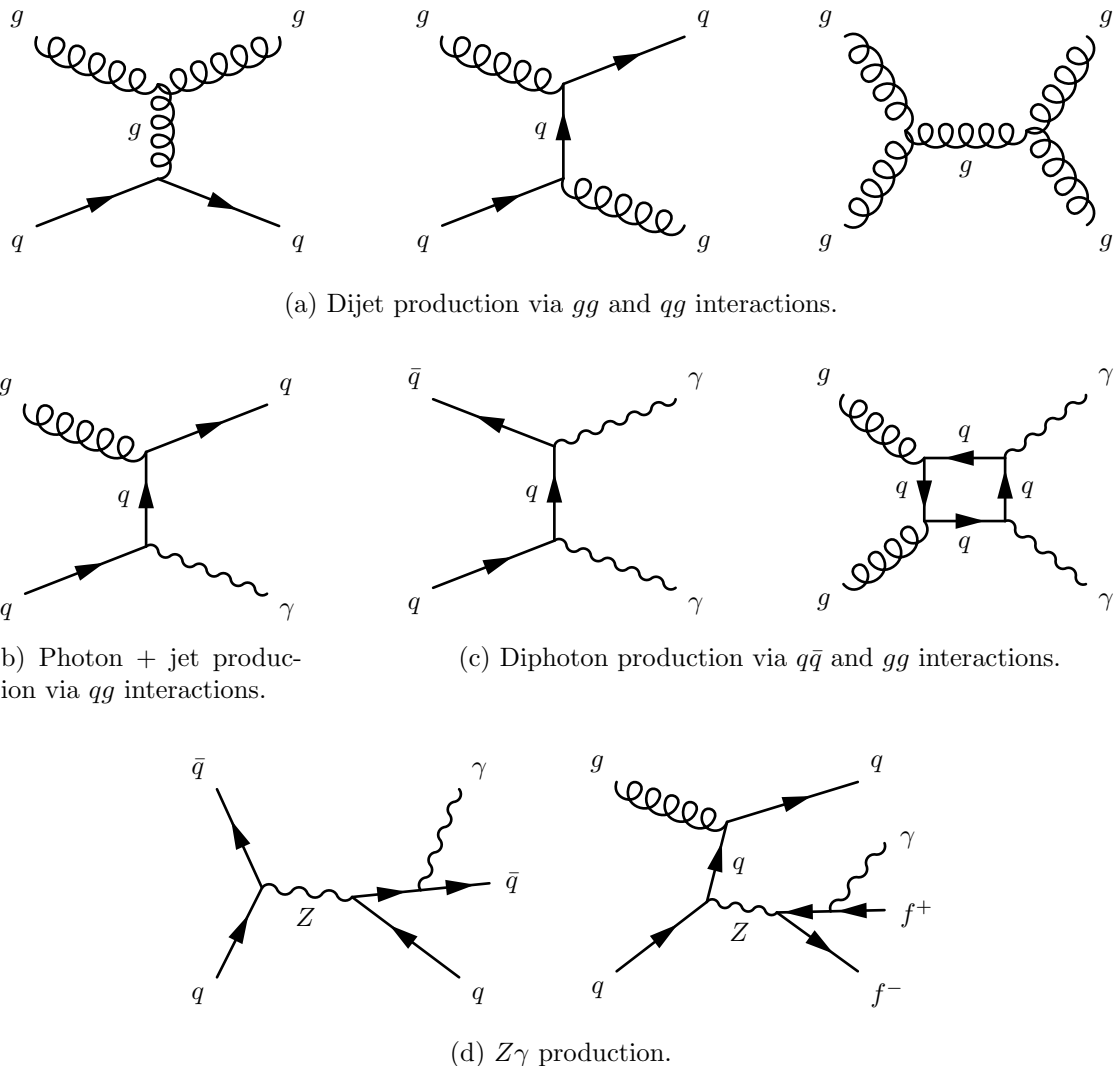


Figure 3.1: Representative Feynman diagrams of some QCD backgrounds to the GGM SUSY search.

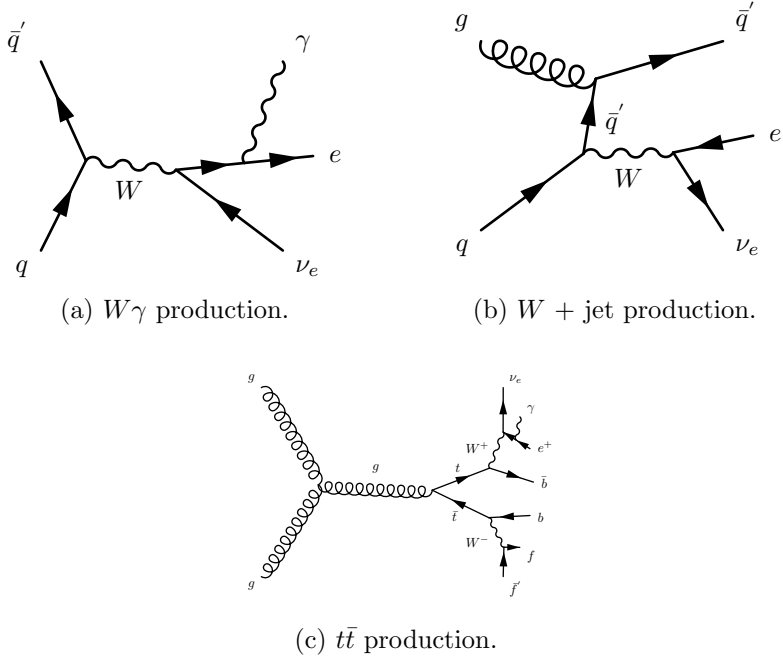


Figure 3.2: Representative Feynman diagrams of some electroweak backgrounds to the GGM SUSY search.

fake photons are still required to pass a tight cut on H/E , they are guaranteed to be very electromagnetic jets, with an EM energy scale and resolution similar to that of the candidate photons. This insures that the resulting estimate of the \cancel{E}_T shape does not have too long of a tail from severe HCAL mis-measurements that are actually rare in the $\gamma\gamma$ sample.

As a cross-check, the ee sample is also used to model the QCD background. This sample of Z decays should have no true \cancel{E}_T , just like the ff sample, and the electron definition (differing from the photon definition only in the presence of a pixel seed) insures that the electron energy scale and resolution is similar to that of the photon.

Finally, the $e\gamma$ sample is used to model the electroweak background from $W \rightarrow e\nu$ decays. The $e\gamma$ \cancel{E}_T distribution is scaled by the electron \rightarrow photon misidentification rate to predict the number of $W\gamma$, $W + \text{jet}$, and $t\bar{t}$ events in the $\gamma\gamma$ sample.

The remainder of this chapter describes the data analysis procedures and the final results of the search. Sec. 3.1 addresses the QCD background estimation. Sec. 3.2

868 addresses the electroweak background estimation. The chapter concludes with a dis-
 869 cussion of systematic errors in Sec. 3.3 and a presentation of the final results in
 870 Sec. 3.4.

871 3.1 Modeling the QCD Background

872 3.1.1 Outline of the Procedure

873 Due to the fact that the CMS ECAL energy resolution is much better than the
 874 HCAL energy resolution, the energies of the two candidate photons in the events of
 875 the $\gamma\gamma$ sample are typically measured to far greater accuracy and precision than the
 876 energy of the hadronic recoil in those events. Therefore, fake E_T in the $\gamma\gamma$ sample
 877 is almost entirely the result of hadronic mis-measurement in QCD dijet, photon +
 878 jet, and diphoton events. The strategy employed to model this background is to find
 879 a control sample in data consisting of two well-measured EM objects, just like the
 880 candidate $\gamma\gamma$ sample, and assign each event a weight to account for the underlying
 881 kinematic differences between the control and candidate samples. Once the reweighted
 882 E_T spectrum of the control sample is created, it is then normalized in the low- E_T
 883 region, the assumption being that GGM SUSY does not predict a significant amount
 884 of events at low E_T . There are three aspects of this QCD background estimation
 885 procedure that bear highlighting:

886 **Choice of control sample** Since the underlying cause of E_T in the candidate sam-
 887 ple is mis-measured hadronic activity, a control sample with similar hadronic
 888 activity to the candidate sample should be chosen. Hadronic activity refers to
 889 number of jets, jet E_T , pileup, etc.

890 **Reweighting** The control sample is reweighted so that its E_T spectrum appears as it
 891 would if the control sample had the same kinematic properties as the candidate

sample (i.e. particle p_T and η distributions, etc.). By choosing an appropriate control sample and reweighting it, the control \cancel{E}_T distribution should now match both the hadronic activity and the kinematics of the candidate sample.

Normalization Finally, the control E_T distribution is normalized in a region of low \cancel{E}_T , where contamination from the expected GGM SUSY signal is small. This implies an extrapolation of the low- \cancel{E}_T QCD background prediction to the high- \cancel{E}_T signal region.

As explained in the beginning of this chapter, the ff sample is used as the primary QCD control sample, while the ee sample is used as a cross-check. Both samples have two well-measured EM objects per event, no real \cancel{E}_T , and similar hadronic activity to the $\gamma\gamma$ sample. Figure 3.3 shows a comparison of the shapes of some distributions relevant to hadronic activity between the $\gamma\gamma$, ee , and ff samples. In general, the ee sample has less hadronic activity than the $\gamma\gamma$ and ff samples, as shown by the more steeply falling ee distributions in Figs. 3.3a, 3.3b, 3.3c, and 3.3d. In addition to the kinematic reweighting, there is also a reweighting by number of jets per event, which attempts to correct for this difference (see Sec. 3.1.2).

3.1.2 Reweighting

To reweight the control sample events to match the kinematics of the candidate sample events, a weight based on the p_T of the di-EM-object system and the number of jets in the event is used. As explained in Sec. 3.1.1, E_T in the $\gamma\gamma$, ff , and ee samples is due to the poorly measured hadronic recoil off the well-measured di-EM system. Therefore, the p_T of the di-EM system is a good handle on the true magnitude of the hadronic recoil, which affects the measured \cancel{E}_T . The di-EM system is depicted in Figure 3.4. As shown in Figure 3.5, \cancel{E}_T is largely uncorrelated with di-EM p_T , so there is little danger of reweighting away a true signal excess.

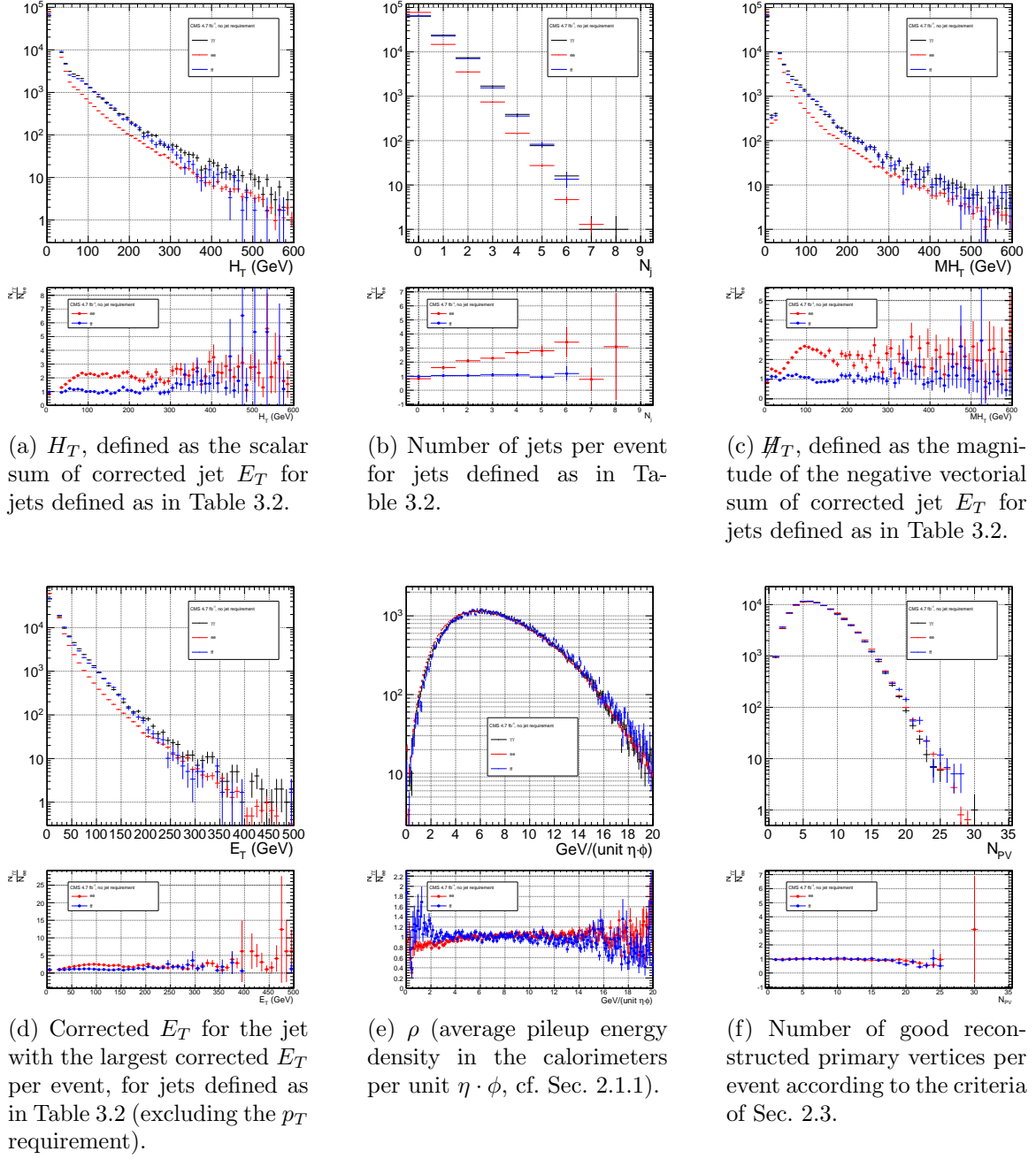


Figure 3.3: Comparison of the shapes of some distributions relevant to hadronic activity between the $\gamma\gamma$, ee ($81 \text{ GeV} \leq m_{ee} < 101 \text{ GeV}$), and ff samples. The ee and ff distributions are normalized to the number of events in the $\gamma\gamma$ distribution. Errors are statistical only.

Table 3.2: Definition of HB/HE/HF hadronic jets.

Variable	Cut
Algorithm	L1FastL2L3Residual corrected PF (cf. Sec. 2.1.3)
p_T	$> 30 \text{ GeV}$
$ \eta $	< 5.0
Neutral hadronic energy fraction	< 0.99
Neutral electromagnetic energy fraction	< 0.99
Number of constituents	> 1
Charged hadronic energy	$> 0.0 \text{ GeV}$ if $ \eta < 2.4$
Number of charged hadrons	> 0 if $ \eta < 2.4$
Charged electromagnetic energy fraction	< 0.99 if $ \eta < 2.4$
ΔR to nearest PF electron ^a , muon ^b , or one of the two primary EM objects	> 0.5

^aA PF electron is defined as an electron reconstructed with the PF algorithm [41] with $p_T > 15 \text{ GeV}$, $|\eta| < 2.6$, and $(I_{\text{charged}} + I_{\text{photon}} + I_{\text{neutral}})/p_T < 0.2$, where $I_{\text{charged}}(I_{\text{photon}})(I_{\text{neutral}})$ is the sum of PF charged hadron(PF photon)(PF neutral hadron) momenta in a $\Delta R = 0.4$ cone around the PF electron.

^bMuons are reconstructed [42] from a combination of muon station and inner tracker hits. Here, a muon must have track $\chi^2 < 10$, at least one good muon station hit, inner track transverse impact parameter $< 0.02 \text{ cm}$, inner track longitudinal impact parameter $< 0.5 \text{ cm}$, $p_T > 15 \text{ GeV}$, $|\eta| < 2.6$, and $(I_{\text{ECAL}} + I_{\text{HCAL}} + I_{\text{track}})/p_T < 0.2$, where $I_{\text{ECAL}}(I_{\text{HCAL}})(I_{\text{track}})$ is the sum of ECAL(HCAL)(track) momenta in a $\Delta R = 0.3$ cone around the muon.

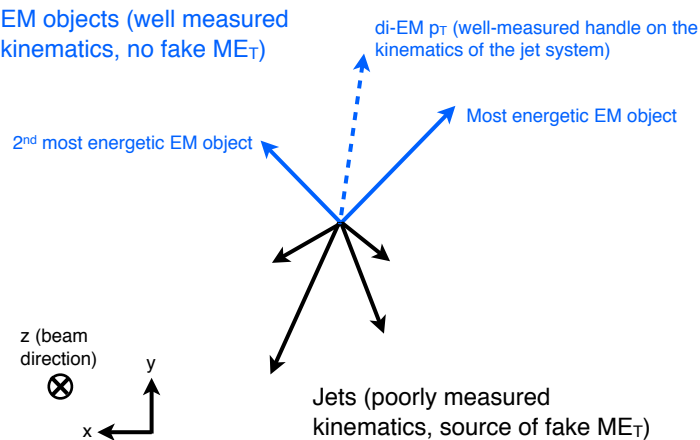


Figure 3.4: Cartoon showing the di-EM system in blue and the hadronic recoil in black. The di-EM p_T (dashed blue line) is used to reweight the control sample kinematic properties to match those of the candidate $\gamma\gamma$ sample.

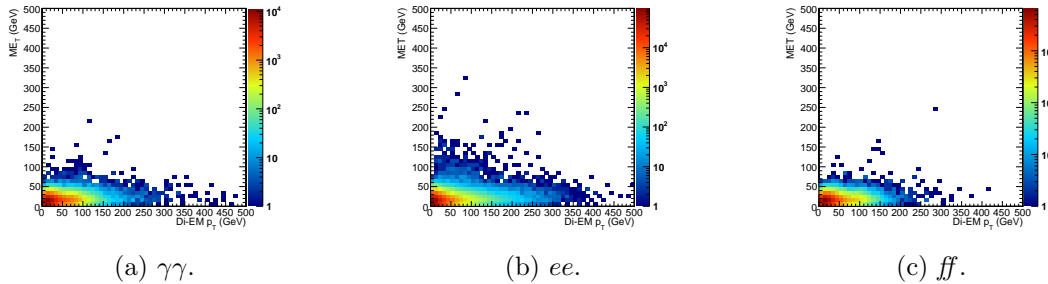


Figure 3.5: E_T vs. di-EM p_T .

Whereas the di-EM p_T reweighting accounts for differences in production kinematics between the control and $\gamma\gamma$ samples, a simultaneous reweighting based on the number of jets in the event accounts for differences in hadronic activity between the samples, especially between ee and $\gamma\gamma$ (cf. Fig. 3.3). Jets are defined as in Table 2.2. Figure 3.6 shows the effect of reweighting by number of jets per event, which is to increase(decrease) the tail of the $ee(ff)$ E_T spectrum.

923 Although the electron and photon energies are well measured by the ECAL, the
 924 ECAL-only measurement of the fake photon energy (cf. Sec 2.1.1) is biased slightly
 925 low due to the fact that fakes (which are really jets) tend to deposit some energy in
 926 the HCAL. This can be seen in Figs. 3.7 and 3.8, which show the relative difference
 927 between the ECAL-only E_T measurement and the PF E_T measurement vs. EMF for
 928 electrons, photons, and fakes. PF E_T is defined as the L1Fast-corrected E_T of the
 929 nearest PF jet with $p_T \geq 20$ GeV (i.e., the E_T of the PF jet object reconstructed from
 930 the same ECAL shower as the fake photon). On average, the fakes tend to deposit
 931 a few percent more energy in the HCAL than the electrons or photons, which is
 932 recovered by the PF algorithm. For this reason, the PF p_T is used in the calculation
 933 of di-EM p_T rather than the ECAL-only p_T .¹ This leads to a modest improvement in
 934 the agreement between the ee and ff E_T spectra, as shown in Figure 3.9.

935 The control sample event weights are defined as

¹In the few events ($\mathcal{O}(10^{-3})$) in which two PF jet objects, corresponding to the two electrons or fakes, are not found, the ECAL-only p_T is used.

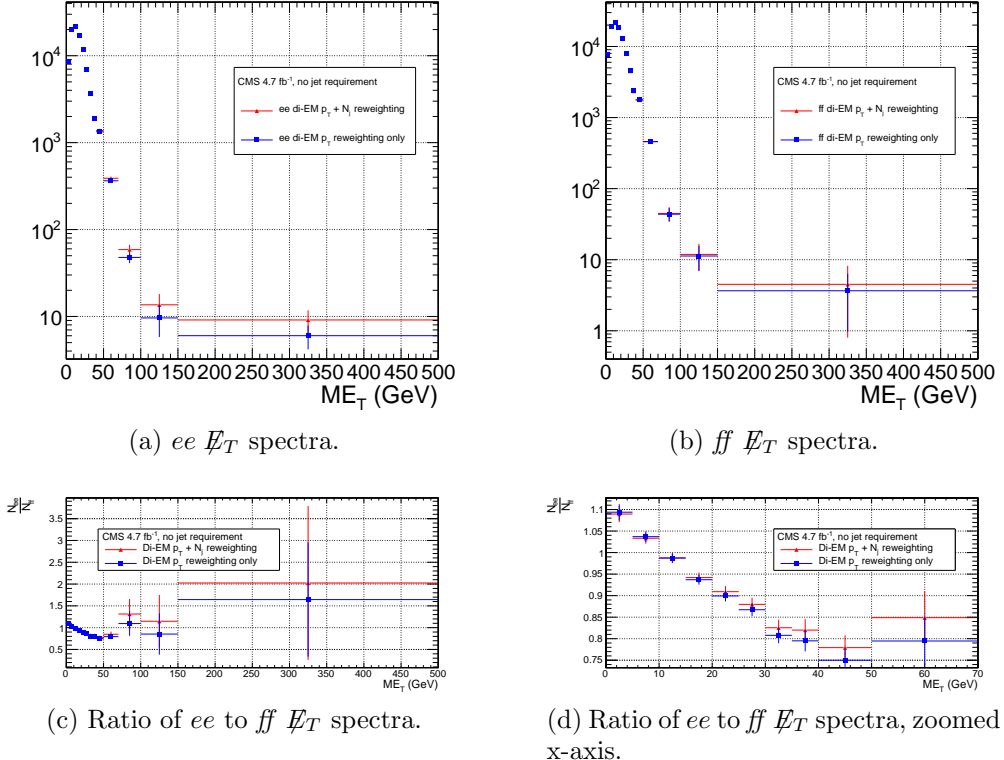


Figure 3.6: \cancel{E}_T spectra of the reweighted ee ($81 \text{ GeV} \leq m_{ee} < 101 \text{ GeV}$) and ff control samples. Blue squares indicate di-EM p_T reweighting only; red triangles indicate di-EM $p_T + \text{number of jets}$ reweighting. PF p_T (cf. p. 67) is used to calculate the di-EM p_T . The full normalization procedure is employed, along with ee sideband subtraction (discussed at the end of this section). Error bars are statistical only.

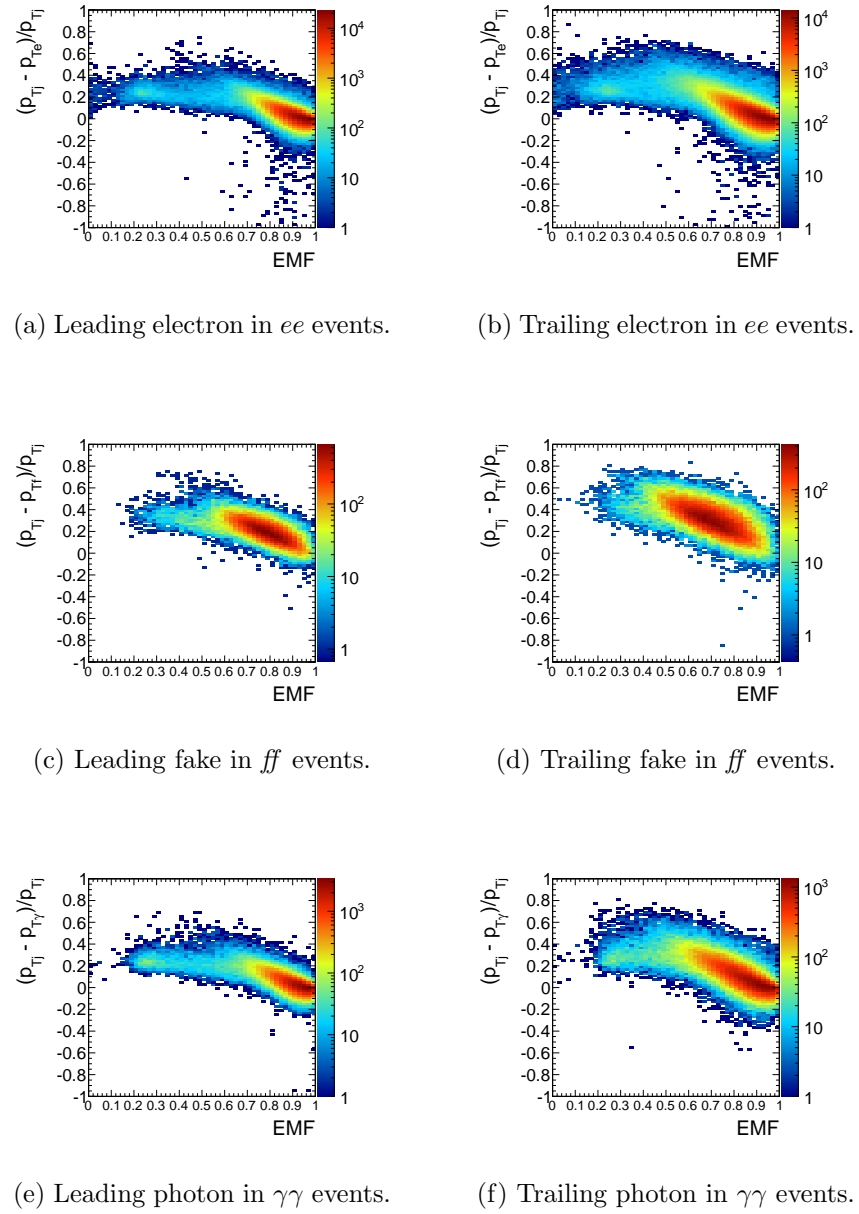


Figure 3.7: Relative difference between the ECAL-only E_T measurement and the PF E_T measurement vs. EMF. PF E_T is defined in the text.

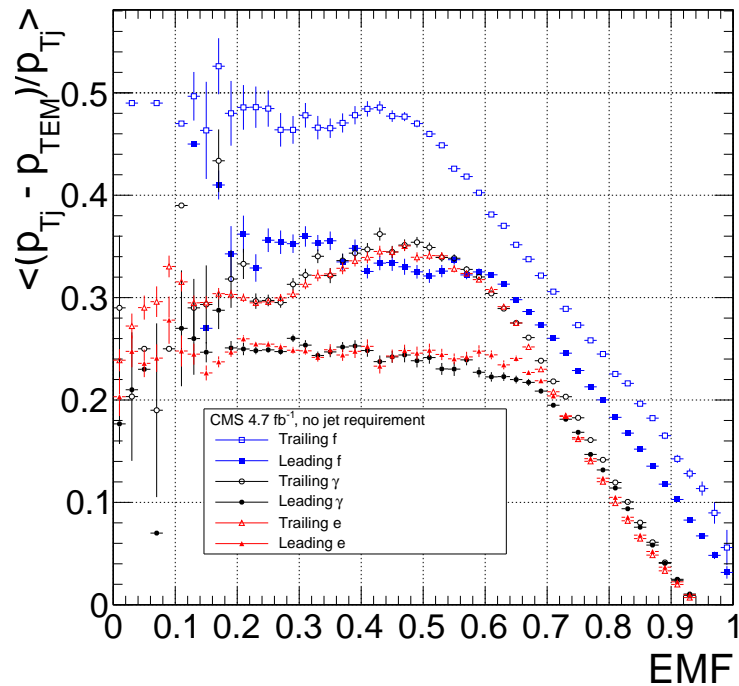


Figure 3.8: Average relative difference between the ECAL-only E_T measurement and the PF E_T measurement vs. EMF for the leading (filled marker) and trailing (open marker) electrons in ee events (red triangles), fakes in ff events (blue squares), and photons in $\gamma\gamma$ events (black circles). These are nothing more than profile histograms of Fig. 3.7. PF E_T is defined in the text. Error bars are statistical only.

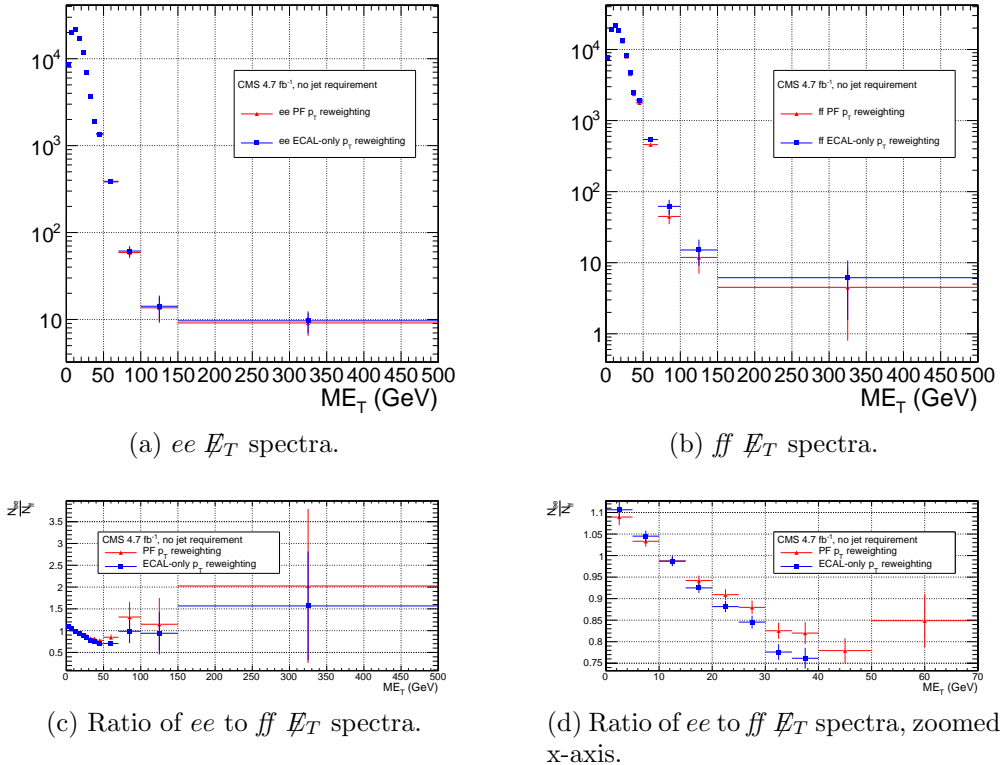


Figure 3.9: E_T spectra of the reweighted ee ($81 \text{ GeV} \leq m_{ee} < 101 \text{ GeV}$) and ff control samples. Blue squares indicate reweighting using the ECAL-only p_T estimate; red triangles indicate reweighting using the PF p_T estimate. The full reweighting and normalization procedure is employed, along with ee sideband subtraction (discussed at the end of this section). Error bars are statistical only.

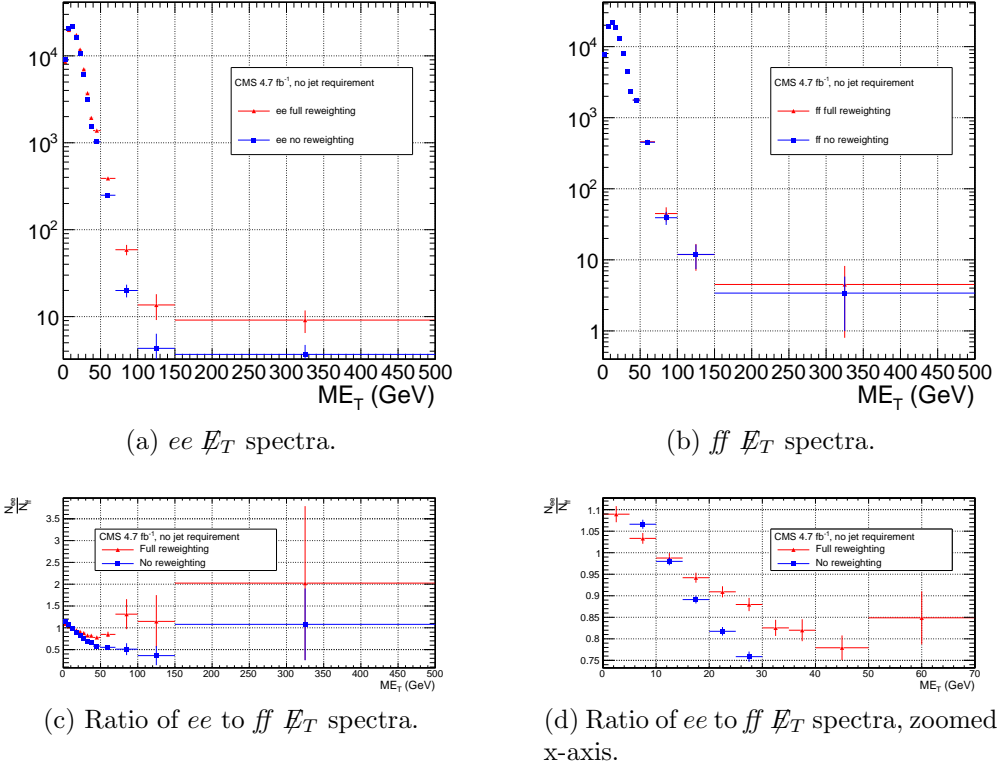


Figure 3.10: E_T spectra of the ee ($81 \text{ GeV} \leq m_{\text{ee}} < 101 \text{ GeV}$) and ff control samples. Red triangles indicate full di-EM $p_T +$ number of jets reweighting; blue squares indicate no reweighting. PF p_T (cf. p. 69) is used to calculate the di-EM p_T . The full normalization procedure is employed, along with ee sideband subtraction (discussed at the end of this section). Error bars are statistical only.

$$w_{ij} = \frac{N_{\text{control}}}{N_{\gamma\gamma}} \frac{N_{\gamma\gamma}^{ij}}{N_{\text{control}}^{ij}} \quad (3.1)$$

where i runs over the number of di-EM p_T bins, j runs over the number of jet bins, N_{control} is the total number of events in the control sample, $N_{\gamma\gamma}$ is the total number of events in the $\gamma\gamma$ sample, $N_{\gamma\gamma}^{ij}$ is the number of $\gamma\gamma$ events in the i^{th} di-EM p_T bin and j^{th} jet bin, and N_{control}^{ij} is the number of control sample events in the i^{th} di-EM p_T bin and j^{th} jet bin. The effect of the reweighting is more significant for the ee sample than for the ff sample, as shown in Figure 3.10.

942 The ee sample contains a non-negligible background of $t\bar{t}$ events in which both
 943 W bosons decay to electrons. These events have significant real \cancel{E}_T from the two
 944 neutrinos (unlike the $\gamma\gamma$ events), and therefore inflate the background estimate at
 945 high \cancel{E}_T . In order to remove the $t\bar{t}$ contribution from the ee sample, a sideband
 946 subtraction method is employed.

947 Only events in the ee sample with $81 \text{ GeV} \leq m_{ee} < 101 \text{ GeV}$, where m_{ee} is the
 948 di-electron invariant mass, are used in the QCD background estimate. This choice
 949 maximizes the ratio of Z signal to background. The sidebands used to estimate the
 950 background contribution within the Z window are defined such that $71 \text{ GeV} \leq m_{ee} <$
 951 81 GeV and $101 \text{ GeV} \leq m_{ee} < 111 \text{ GeV}$.

952 The full reweighting procedure is applied to the Z signal region and the two
 953 sideband regions independently. Only Z signal events are used in the calculation of
 954 the di-EM p_T weights for the Z signal region, and likewise only the events within
 955 a given sideband region are used in the calculation of the weights for that region.
 956 Assuming a constant $t\bar{t}$ background shape, the resulting reweighted sideband \cancel{E}_T
 957 distributions are added together and subtracted from the reweighted Z signal \cancel{E}_T
 958 distribution. The sideband subtracted Z signal \cancel{E}_T distribution is then normalized
 959 as discussed in Secs. 3.1.1 and 3.1.3. The statistical and reweighting error from the
 960 sideband regions is propagated to the error on the final ee QCD \cancel{E}_T estimate.

961 The di-EM p_T weights for the two ee sideband regions are shown in Figure 3.11.
 962 The overall scale of the weights, as well as the trend with di-EM p_T , is similar for
 963 the two regions (except at high di-EM p_T , where the statistics are poor anyway).
 964 Figure 3.12 shows the \cancel{E}_T spectra for the two sideband regions and the Z signal
 965 region after subtraction. The shapes of the spectra indicate that the high- \cancel{E}_T $t\bar{t}$ tail,
 966 present in the sideband distributions, was successfully subtracted from the Z signal
 967 distribution.

968 The ee ($81 \text{ GeV} \leq m_{ee} < 101 \text{ GeV}$), ff , and $\gamma\gamma$ di-EM p_T spectra for events with

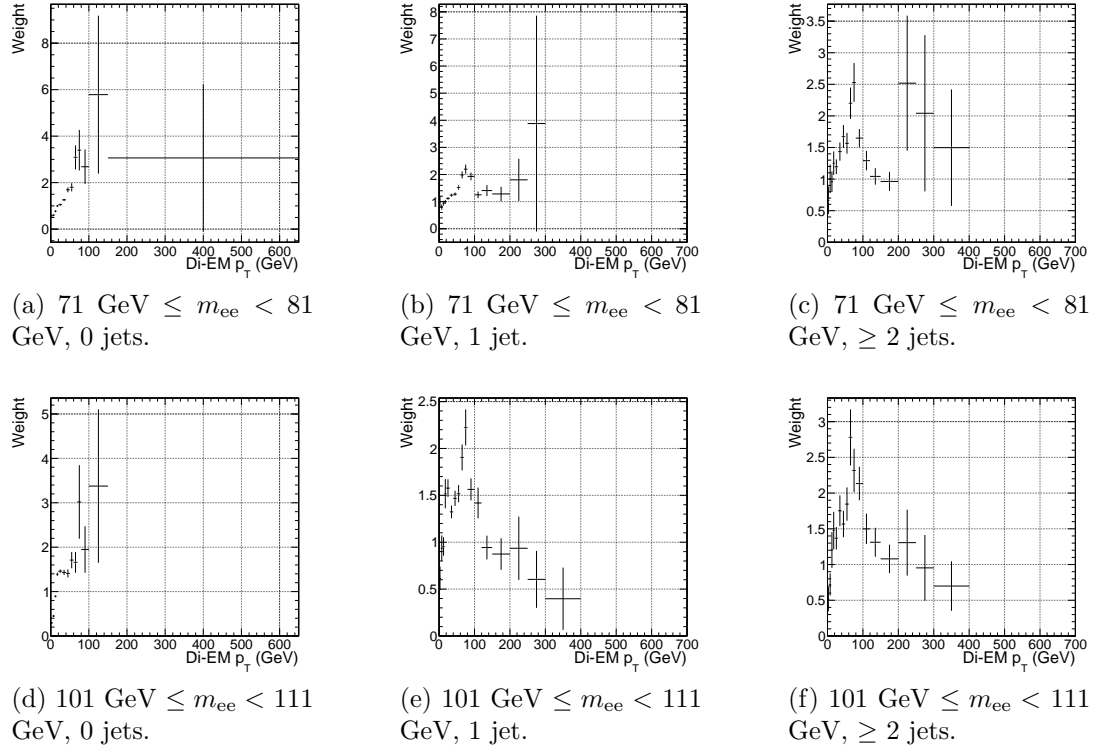


Figure 3.11: ee sideband di-EM p_T weights for events with 0, 1, or ≥ 2 jets (as in Table 2.2). Errors are statistical only.

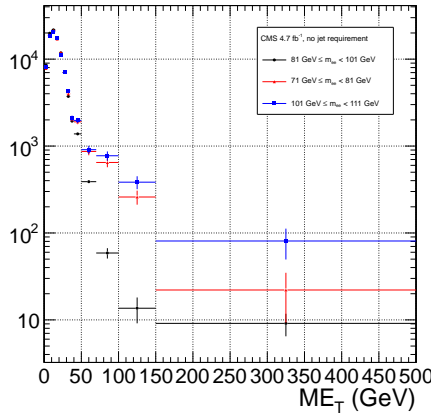


Figure 3.12: E_T spectra of the ee sample for $71 \text{ GeV} \leq m_{ee} < 81 \text{ GeV}$ (red triangles), $81 \text{ GeV} \leq m_{ee} < 101 \text{ GeV}$ (black circles), and $101 \text{ GeV} \leq m_{ee} < 111 \text{ GeV}$ (blue squares). The two sideband distributions (red and blue) and the Z signal distribution (black) are normalized to the total number of $\gamma\gamma$ events. Errors are statistical only.

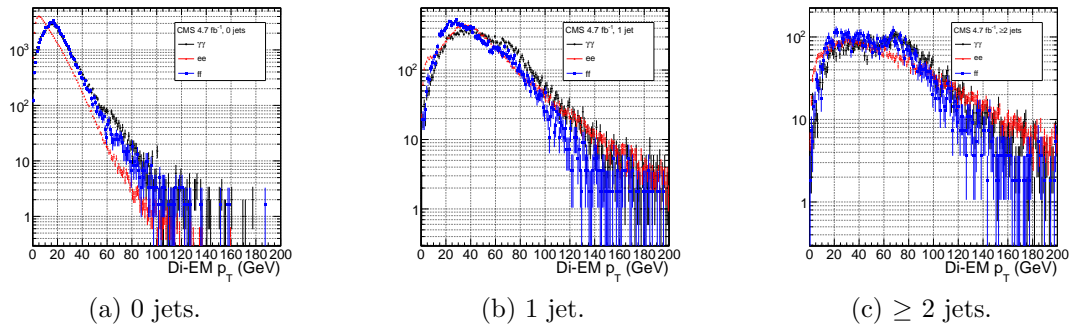


Figure 3.13: ee ($81 \text{ GeV} \leq m_{ee} < 101 \text{ GeV}$) (red triangles), ff (blue squares), and $\gamma\gamma$ (black circles) di-EM p_T spectra for events with 0, 1, or ≥ 2 jets (as in Table 2.2). Errors are statistical only.

969 0, 1, or ≥ 2 jets (as in Table 2.2) are shown in Figure 3.13. Broad humps in the ff
 970 and $\gamma\gamma$ spectra are due to kinematic ΔR and p_T turn-ons that are suppressed in the
 971 ee sample due to the invariant mass cut. Figure 3.14 shows the weights applied to
 972 the ee ($81 \text{ GeV} \leq m_{ee} < 101 \text{ GeV}$) and ff \cancel{E}_T spectra as a function of di-EM p_T and
 973 number of jets per event.

974 3.1.3 Normalization

After reweighting, the \cancel{E}_T distributions of the QCD control samples are normalized to the $\cancel{E}_T < 20$ GeV region of the candidate $\gamma\gamma \cancel{E}_T$ spectrum, where signal contamination is low. The normalization factor is $(N_{\gamma\gamma}^{\cancel{E}_T < 20\text{GeV}} - N_{e\gamma}^{\cancel{E}_T < 20\text{GeV}})/N_{\text{control}}^{\cancel{E}_T < 20\text{GeV}}$, where $N_{e\gamma}^{\cancel{E}_T < 20\text{GeV}}$ is the expected number of electroweak background events with $\cancel{E}_T < 20$ GeV (discussed in Section 3.2).

980 3.2 Modeling the Electroweak Background

⁹⁸¹ $W\gamma$, $W + \text{jet}$, and $t\bar{t}$ processes in which the W decay electron is misidentified as a
⁹⁸² photon (due to a failure to properly associate a pixel seed to the electron candidate)
⁹⁸³ can contribute significantly to the high- E_T tail of the $\gamma\gamma E_T$ spectrum. To estimate

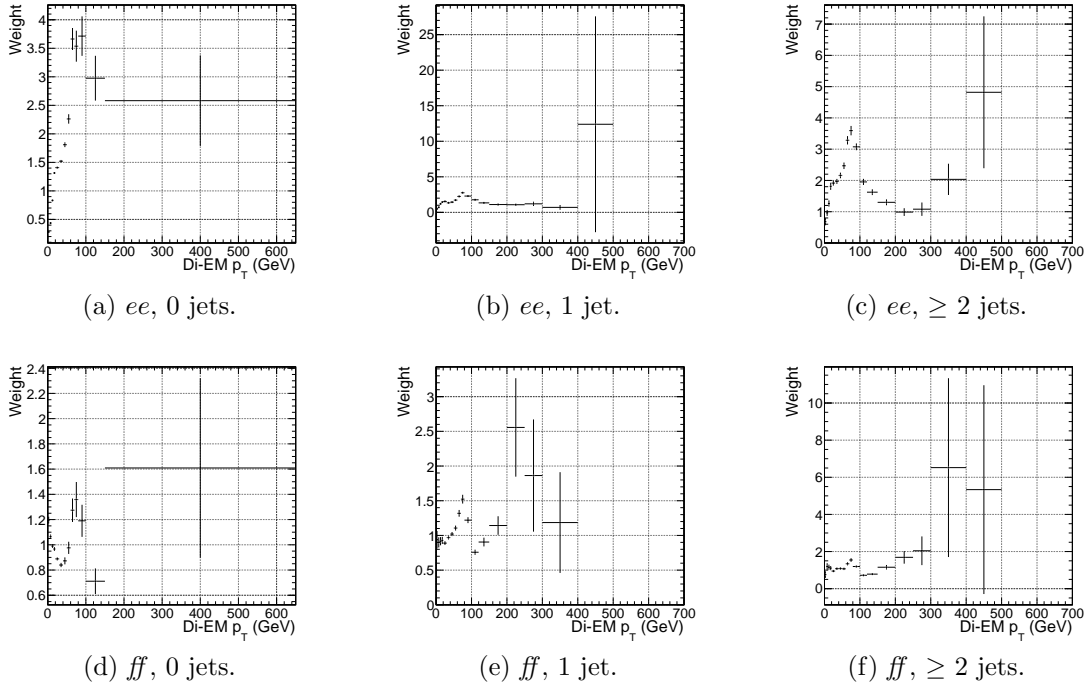


Figure 3.14: ee ($81 \text{ GeV} \leq m_{ee} < 101 \text{ GeV}$) and ff di-EM p_T weights for events with 0, 1, or ≥ 2 jets (as in Table 2.2). Errors are statistical only.

984 this background, the $e\gamma$ sample, which is enriched in $W \rightarrow e\nu$ decays, is scaled by
 985 $f_{e \rightarrow \gamma}/(1 - f_{e \rightarrow \gamma})$, where $f_{e \rightarrow \gamma}$ is the rate at which electrons are misidentified as photons.
 986 The derivation of this scaling factor comes from the two equations

$$N_{e\gamma}^W = f_{e \rightarrow e} N_W \quad (3.2)$$

$$N_{\gamma\gamma}^W = (1 - f_{e \rightarrow e}) N_W \quad (3.3)$$

987 where $N_{e\gamma}^W$ is the number of W events in the $e\gamma$ sample in which the electron was
 988 correctly identified, $f_{e \rightarrow e}$ is the probability to correctly identify an electron, N_W is
 989 the true number of triggered $W \rightarrow e\nu$ events, and $N_{\gamma\gamma}^W$ is the number of W events in
 990 the $\gamma\gamma$ sample in which the electron was misidentified as a photon. The contribution
 991 from $Z \rightarrow ee$ can be neglected (i.e. $f_{e \rightarrow \gamma}$ is small and the Z contribution involves
 992 $f_{e \rightarrow \gamma}^2$, since both electrons have to be misidentified). Since $f_{e \rightarrow e} = 1 - f_{e \rightarrow \gamma}$, solving

993 for $N_{\gamma\gamma}^W$ gives

$$N_{\gamma\gamma}^W = \frac{f_{e\rightarrow\gamma}}{1 - f_{e\rightarrow\gamma}} N_{e\gamma}^W \quad (3.4)$$

994 $f_{e\rightarrow\gamma}$ is measured by fitting the Z peaks in the ee and $e\gamma$ samples. The number of
995 Z events fitted in the ee and $e\gamma$ samples, respectively, is given by

$$N_{ee}^Z = (1 - f_{e\rightarrow\gamma})^2 N_Z \quad (3.5)$$

$$N_{e\gamma}^Z = 2f_{e\rightarrow\gamma}(1 - f_{e\rightarrow\gamma}) N_Z \quad (3.6)$$

996 where N_Z is the true number of triggered $Z \rightarrow ee$ events. Solving for $f_{e\rightarrow\gamma}$ gives

$$f_{e\rightarrow\gamma} = \frac{N_{e\gamma}^Z}{2N_{ee}^Z + N_{e\gamma}^Z} \quad (3.7)$$

997 A Crystal Ball function is used to model the Z signal shape in both the ee and
998 $e\gamma$ samples, while an exponential convoluted with an error function (`RooCMSShape`,
999 see Sec. 2.4.1) is used to model the background shape. The fixed fit parameters are
1000 identical for the two samples, but the other parameters are allowed to float indepen-
1001 dently. Table 3.3 shows the values and ranges of the fixed and floating fit parameters,
1002 respectively.

1003 Fits to the ee and $e\gamma$ invariant mass spectra are shown in Figure 3.15. Figure 3.16
1004 indicates that the dependence of $f_{e\rightarrow\gamma}$ on the electron p_T and η is small. (Note that all
1005 fit parameters are floating in the p_T -dependent fits.) Therefore, a constant misidenti-
1006 fication rate (derived from all ee and $e\gamma$ events), rather than a p_T - and η -dependent
1007 misidentification rate, is used in the final electroweak background estimate, with the

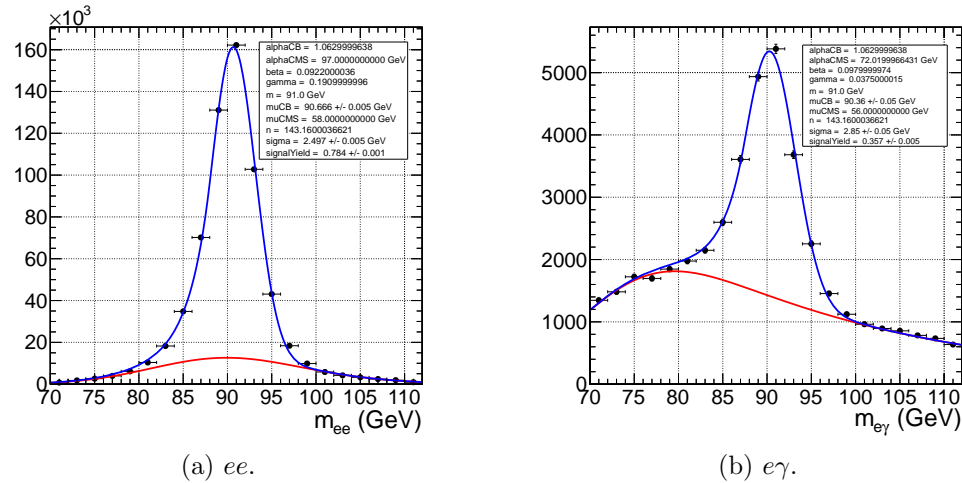


Figure 3.15: Fits to the ee and $e\gamma$ invariant mass spectra using the Crystal Ball `RooCMSShape` function described in the text and in Table 3.3. The total fit is shown in blue, while the background component is shown in red.

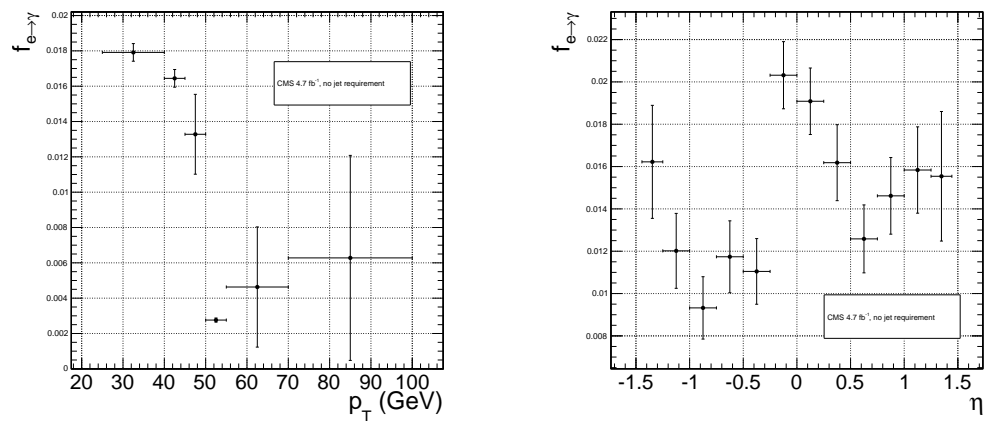
difference between the constant rate and the rate for electrons with p_T between 25
 and 40 GeV (the range in which the bulk of the trailing photons in the $\gamma\gamma$ sample
 lie) taken as a systematic error.

Using the integrals of the Z fits shown in Fig. 3.15, Eq. 3.7, and the p_T systematic discussed above, $f_{e \rightarrow \gamma}$ is calculated to be $0.014 \pm 0.000(\text{stat.}) \pm 0.004(\text{syst.})$. The scaled $e\gamma$ MET distribution is shown in Figure 3.17.

In the 36 pb^{-1} version of this analysis [64], it was shown that the ee sample could
 accurately predict the QCD and real Z contribution to the $e\gamma$ sample at low \cancel{E}_T , and
 that the expectation from $W \rightarrow e\nu$ MC accounted for the remaining W contribution
 at high \cancel{E}_T . A plot of the \cancel{E}_T distributions of the 2010 $e\gamma$ sample and the predicted
 components is shown in Figure 3.18. This exercise helps to validate both the QCD
 and electroweak background prediction methods.

Table 3.3: Parameter values for the signal and background PDFs for the ee and $e\gamma$ samples. When a bracketed range is given, the parameter is allowed to float within that range. When a constant is given, the parameter is fixed to that constant.

PDF	Crystal Ball fit parameters				RooCMSShape fit parameters			
	μ	σ	α	n	μ	α	β	γ
ee signal	[86.2, 96.2]	[1.0, 5.0]	1.063	143.16	N/A	N/A	N/A	N/A
$e\gamma$ signal	[86.2, 96.2]	[1.0, 5.0]	1.063	143.16	N/A	N/A	N/A	N/A
ee background	N/A	N/A	N/A	N/A	58	97.0	0.0922	0.191
$e\gamma$ background	N/A	N/A	N/A	N/A	56	72.02	0.098	0.0375



(a) $f_{e \rightarrow \gamma}$ vs. electron p_T . For the lowest p_T bin, the fit to the $e\gamma$ spectrum does not converge well, so the Z signal fraction is fixed to the value in Fig. 3.15b.

(b) $f_{e \rightarrow \gamma}$ vs. electron η .

Figure 3.16: $f_{e \rightarrow \gamma}$ vs. electron p_T and η .

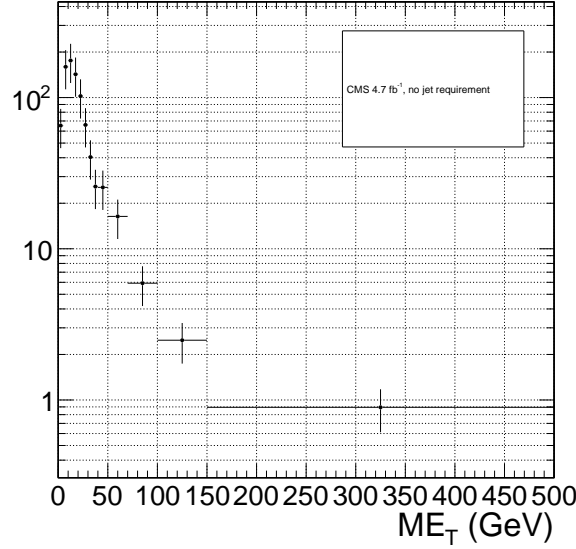


Figure 3.17: E_T spectrum of the $e\gamma$ sample after scaling by $f_{e \rightarrow \gamma}$. The total error on $f_{e \rightarrow \gamma}$ is propagated to the total error on the electroweak background estimate.

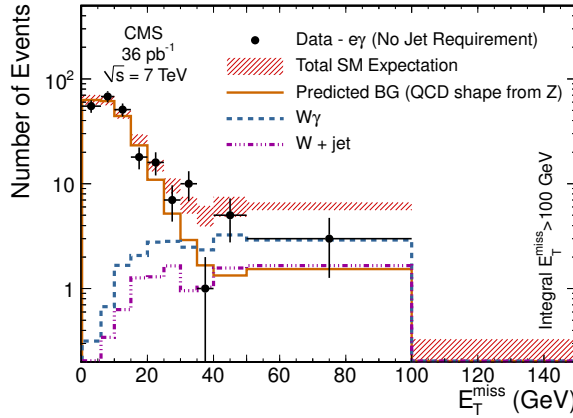


Figure 3.18: E_T spectrum of the $e\gamma$ sample in 36 pb^{-1} of 2010 LHC data scaled by the 2010 measured $f_{e \rightarrow \gamma}$ (black dots), QCD and real Z predicted background from the 2010 ee sample (solid orange line), MC $W + \text{jet}$ estimate (dash-dotted purple line), and MC $W\gamma$ estimate (dashed blue line). The total $e\gamma$ prediction (red band) is the sum of the ee , $W + \text{jet}$, and $W\gamma$ predictions. Reprinted from Fig. 2 of ref. [64].

1020 **3.3 Errors on the Background Prediction**

1021 The statistical error on the final background estimate in a particular \cancel{E}_T bin comes
 1022 from three sources: the number of control sample events collected in that bin, the
 1023 statistical error on the weights applied to events in that bin, and the statistics of the
 1024 normalization region. In the case of the ee control sample, there are contributions
 1025 from the statistics of the m_{ee} sidebands as well.

1026 In order to estimate the statistical error due to the reweighting procedure, 1000
 1027 toy sets of weights are generated. Each set includes a weight for each (di-EM p_T , N_j)
 1028 bin, with the values picked from a Gaussian distribution with mean and standard
 1029 deviation equal to the observed weight for that bin and its statistical error. The effect
 1030 of reweighting error is not correlated between \cancel{E}_T bins. For each of the 1000 exper-
 1031 iments, the control sample data are reweighted according to the generated weights,
 1032 and the background estimates are calculated for each \cancel{E}_T bin. Since the distribution
 1033 of the toy background estimates follows a Gaussian distribution in each \cancel{E}_T bin, the
 1034 RMS spread of the estimates is taken as the statistical error due to reweighting. This
 1035 procedure is carried out for the ff , ee , low sideband ee , and high sideband ee samples.

1036 The total statistical error on the background estimate per \cancel{E}_T bin is given by

$$\sigma_{\text{stat}}^2 = \sigma_{\text{stat,QCD}}^2 + \sigma_{\text{stat,EW}}^2 \quad (3.8)$$

1037 where $\sigma_{\text{stat,QCD}}^2$ is the square of the total statistical error on the QCD prediction in
 1038 the \cancel{E}_T bin

$$\sigma_{\text{stat,QCD}}^2 = \sigma_{\text{stat},s}^2 + \sigma_{\text{Poisson,QCD}}^2 + \sigma_{\text{reweight},s}^2 + \sigma_{\text{reweight,QCD}}^2 \quad (3.9)$$

1039 and $\sigma_{\text{stat,EW}}$ is the Poisson error on the number of $e\gamma$ events in the \cancel{E}_T bin ($= \sqrt{N_{e\gamma}}$,
 1040 where $N_{e\gamma}$ is the prediction in the \cancel{E}_T bin after scaling by $f_{e\rightarrow\gamma}$). The contributions
 1041 to $\sigma_{\text{stat,QCD}}^2$ are discussed below.

- 1042 • $\sigma_{\text{stat},s}^2$ is the statistical error contributed by the normalization factor s (i.e. from
 1043 Poisson error in the normalization region $\cancel{E}_T < 20$ GeV):

$$\begin{aligned}\sigma_{\text{stat},s}^2 = & \frac{N_{\text{control}}^2}{(N_{\gamma\gamma}^{\text{norm}} - N_{e\gamma}^{\text{norm}})^2} (\left[\sigma_{\text{Poisson},\gamma\gamma}^{\text{norm}}\right]^2 + \left[\sigma_{\text{Poisson},e\gamma}^{\text{norm}}\right]^2) + \\ & \frac{N_{\text{control}}^2}{(N_{\text{control}}^{\text{norm}})^2} (\sigma_{\text{Poisson,control}}^{\text{norm}})^2\end{aligned}\quad (3.10)$$

1044 where N_{control} is the number of reweighted, normalized events in the \cancel{E}_T bin,
 1045 $N_{\gamma\gamma}^{\text{norm}}$ is the number of $\gamma\gamma$ events in the normalization region, $N_{e\gamma}^{\text{norm}}$ is the num-
 1046 ber of $e\gamma$ events in the normalization region (after scaling by $f_{e\rightarrow\gamma}$), $\sigma_{\text{Poisson},\gamma\gamma}^{\text{norm}}$
 1047 is the Poisson error on the number of $\gamma\gamma$ events in the normalization region
 1048 ($= \sqrt{N_{\gamma\gamma}^{\text{norm}}}$), $\sigma_{\text{Poisson},e\gamma}^{\text{norm}}$ is the Poisson error on the number of $e\gamma$ events in the
 1049 normalization region ($= \sqrt{N_{e\gamma}^{\text{norm}}}$), $N_{\text{control}}^{\text{norm}}$ is the number of QCD control (ee
 1050 or ff) events in the normalization region, and $\sigma_{\text{Poisson,control}}^{\text{norm}}$ is the Poisson error
 1051 on the number of QCD control (ee or ff) events in the normalization region
 1052 ($= \sqrt{\sum_{i=1}^{N_{\text{control}}^{\text{norm}}} w_i^2}$, where w_i is the di-EM p_T weight applied to event i). For
 1053 the ee control region, N_{control} and $N_{\text{control},\text{norm}}$ are sideband subtracted, and
 1054 $\sigma_{\text{Poisson,control}}^{\text{norm}}$ includes the Poisson error on the number of sideband events.

- 1055 • $\sigma_{\text{Poisson,QCD}}$ is the Poisson error due to the number of QCD control (ee or ff)
 1056 events in the \cancel{E}_T bin, equal to $\sqrt{\sum_{i=1}^{N_{\text{control}}^{\text{norm}}} w_i^2}$, where w_i is the di-EM p_T weight
 1057 applied to event i . For the ee control region, $\sigma_{\text{Poisson,QCD}}$ includes the Poisson
 1058 error on the number of subtracted sideband events.
- 1059 • $\sigma_{\text{reweight},s}$ is the error contributed by the control sample reweighting in the nor-

1060 malization region ($= \frac{N_{\text{control}}^2}{(N_{\text{control}}^{\text{norm}})^2} \sigma_{\text{reweight,control}}^{\text{norm}}$). $\sigma_{\text{reweight,control}}^{\text{norm}}$ is the quadrature
 1061 sum of the RMS of the 1000 toy reweighting experiments for each \cancel{E}_T bin in the
 1062 normalization region. For the ee control sample, it also includes (in quadrature)
 1063 the RMS of the toys in the sideband samples.

- 1064 • $\sigma_{\text{reweight,QCD}}$ is the error contributed by the control sample reweighting in the \cancel{E}_T
 1065 bin ($= s\sigma_{\text{reweight,control}}$). $\sigma_{\text{reweight,control}}$ is the RMS of the 1000 toy reweighting
 1066 experiments for the E_T bin. For the ee control sample, it also includes (in
 1067 quadrature) the RMS of the toys in the sideband samples.

1068 The dominant source of systematic error on the background estimate is the slight
 1069 difference in hadronic activity between the ee , ff , and $\gamma\gamma$ samples. This results in a
 1070 small bias (~ 1 GeV) of the ee \cancel{E}_T distribution towards lower values with respect to
 1071 the ff and $\gamma\gamma$ samples, as shown in Figure 3.19. Therefore, the ff sample is used as
 1072 the primary QCD background estimator, and the difference between the ee and ff
 1073 predictions is assigned as an error on the knowledge of the hadronic activity. For \cancel{E}_T
 1074 > 100 GeV, this error amounts to 43% of the total QCD + electroweak background
 1075 estimate.

1076 The second largest source of systematic error comes from the p_T dependence of the
 1077 $e \rightarrow \gamma$ misidentification rate (see 3.2). For $\cancel{E}_T > 100$ GeV, the expected electroweak
 1078 background is 3.4 ± 1.0 events, so this error amounts to 4.8% of the total QCD +
 1079 electroweak background estimate.

1080 Finally, the assumption of a constant $t\bar{t}$ and $W + \text{jets}$ background shape under
 1081 the Z peak in the ee sample induces a systematic error on the ee sideband-subtracted
 1082 background prediction. To assess the magnitude of this error, the sideband subtraction
 1083 (see Sec. 3.1.2) is performed once using only the prediction from the high sideband,
 1084 and once using only the prediction from the low sideband. In each of these cases, the
 1085 prediction is weighted by a factor of two, to account for the fact that the sideband
 1086 regions are only half as wide (10 GeV) as the signal region (20 GeV). The maximum

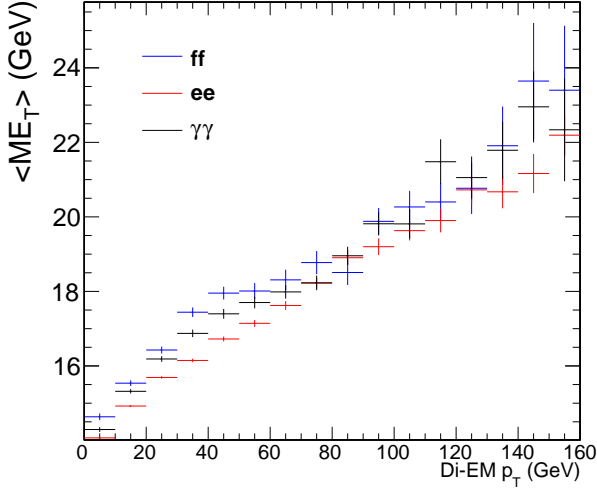


Figure 3.19: Average \mathcal{E}_T vs. di-EM p_T for the ff (blue), ee (red), and $\gamma\gamma$ (black) samples.

1087 variation from the nominal ee estimate is taken as the error, which amounts to 11%
 1088 for $\mathcal{E}_T > 100$ GeV. \mathcal{E}_T distributions using the nominal ee sideband subtraction, the
 1089 low-sideband-only subtraction, and the high-sideband-only subtraction are shown in
 1090 Figure 3.20.

1091 The uncertainty in how to define the (di-EM p_T , N_j) bins, especially at high di-
 1092 EM p_T where the statistics are low, is covered by the 1000-toys procedure as long as
 1093 the bins are not too coarse. This is shown in Figure 3.21. If the bins are too coarse,
 1094 the details of the shape of the di-EM p_T spectra are lost, and the reweighting has a
 1095 smaller effect.

1096 The use of uncorrected instead of corrected PF \mathcal{E}_T (see Sec. 2.1.3) makes no
 1097 difference in the agreement of the background predictions and the search sample in
 1098 a control region at low \mathcal{E}_T , as shown in Figure 3.22. Since the control samples are
 1099 derived from the same data as the search sample, any biases in the \mathcal{E}_T reconstruction
 1100 due to jet energy scale are present equally in both samples.

1101 Tables 3.4 and 3.5 list all the errors on the ee and ff QCD background predictions,
 1102 respectively, for the \mathcal{E}_T bins used in the search. Table 3.6 lists the errors on the

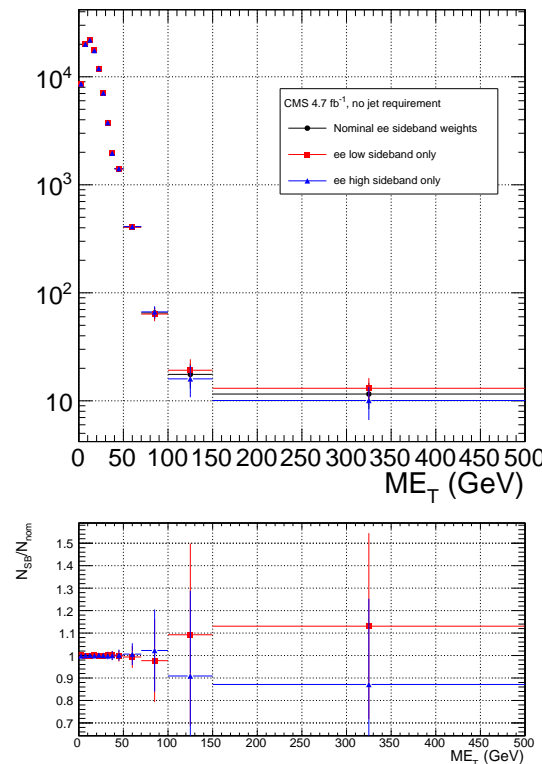


Figure 3.20: ee E_T distributions using the nominal sideband subtraction (black circles), low sideband only (red squares), and high sideband only (blue triangles). The bottom plot shows the ratio of the low sideband distribution to the nominal (red squares) and the ratio of the high sideband distribution to the nominal (blue triangles).

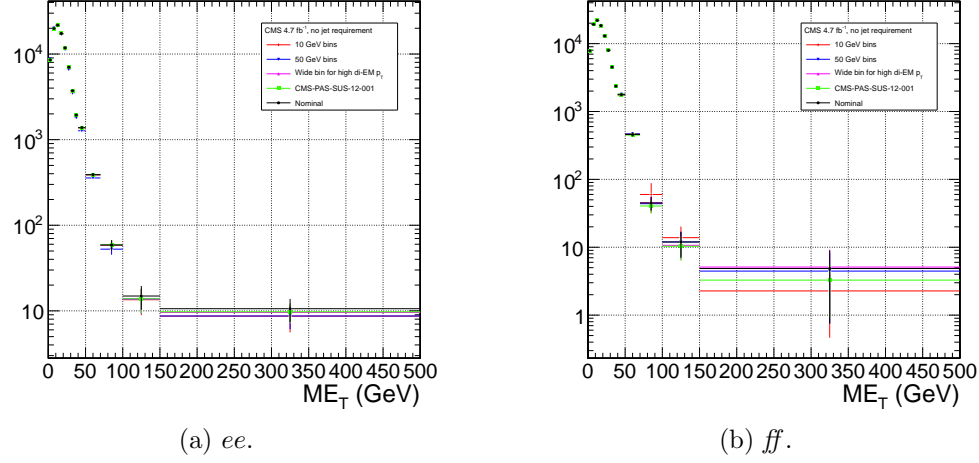


Figure 3.21: Comparison of E_T distributions for five different di-EM p_T bin definitions: uniform bins of width 10 GeV (red diamonds); uniform bins of width 50 GeV (blue downward-pointing triangles); bins with lower edges $\{0.0, 5.0, 10.0, 15.0, 20.0, 30.0, 40.0, 50.0, 60.0, 70.0, 80.0, 100.0, 750.0\}$ GeV for 0-jet events and $\{0.0, 5.0, 10.0, 15.0, 20.0, 30.0, 40.0, 50.0, 60.0, 70.0, 80.0, 100.0, 120.0, 150.0, 200.0, 700.0\}$ GeV for ≥ 1 -jet events (magenta upward-pointing triangles), i.e. a single wide bin at high di-EM p_T ; bins with lower edges $\{0.0, 5.0, 10.0, 15.0, 20.0, 30.0, 40.0, 50.0, 60.0, 70.0, 80.0, 100.0, 150.0\}$ GeV for 0-jet events and $\{0.0, 5.0, 10.0, 15.0, 20.0, 30.0, 40.0, 50.0, 60.0, 70.0, 80.0, 100.0, 120.0, 150.0, 200.0\}$ GeV for ≥ 1 -jet events (green squares), i.e. the bins used in ref. [19]; and the nominal bin definitions shown in Fig. 3.14 (black circles).

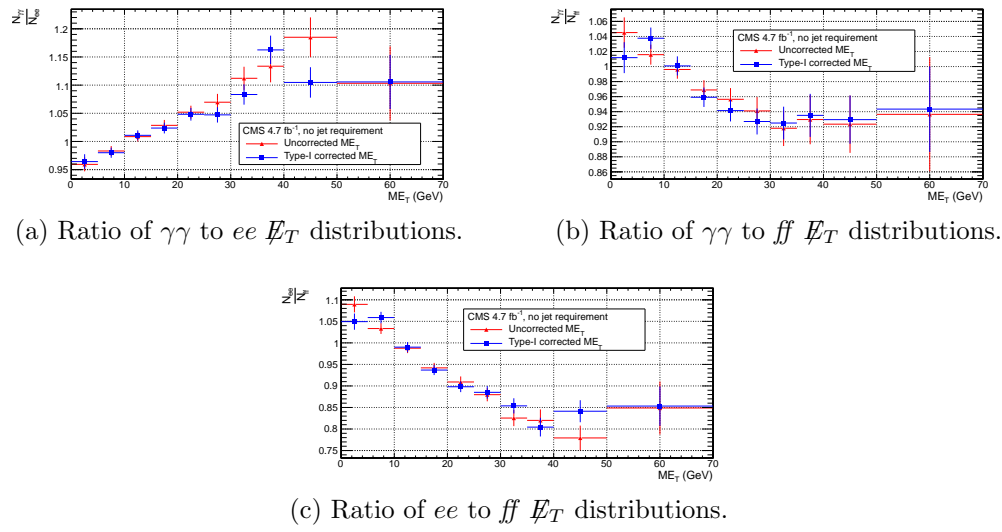


Figure 3.22: Agreement between $\gamma\gamma$, ee , and ff samples for uncorrected (red triangles) and corrected (blue squares) E_T .

1103 electroweak background prediction. Finally, Table 3.7 shows the errors on the total
1104 QCD + electroweak background prediction, broken down by origin (statistical or
1105 systematic) and QCD background estimation sample (ee or ff). In the final result,
1106 only the ff QCD estimate is used.

Table 3.4: Errors on the ee QCD background prediction as a fraction of the ee prediction.

Source of error	Fractional uncertainty (%)				
	[50, 60)	[60, 70)	[70, 80)	[80, 100)	≥ 100
Total	3.9	8.1	16	25	25
Statistics	3.6	7.8	16	24	22
No. events	3.6	7.7	15	24	20
In norm. region	0.43	0.44	0.46	0.55	0.51
In this E_T bin	3.5	7.7	15	24	20
Reweighting	0.73	1.2	3.5	4.3	7.7
In norm. region	0.19	0.19	0.2	0.24	0.23
In this E_T bin	0.71	1.2	3.5	4.3	7.7
Systematics	1.4	2	0.72	5.5	12
$f_{e \rightarrow \gamma}$ (in norm. region)	0.0012	0.0012	0.0013	0.0015	0.0014
m_{ee} background shape	1.4	2	0.72	5.5	12

Table 3.5: Errors on the ff QCD background prediction as a fraction of the ff prediction.

Source of error	Fractional uncertainty (%)				
	[50, 60)	[60, 70)	[70, 80)	[80, 100)	≥ 100
Total	15	25	61	34	64
Statistics	7.2	14	30	33	38
No. events	7.1	14	29	33	36
In norm. region	0.64	0.64	0.64	0.64	0.64
In this E_T bin	7.1	14	29	33	36
Reweighting	0.85	2.7	5.1	6.9	13
In norm. region	0.27	0.27	0.27	0.27	0.27
In this E_T bin	0.81	2.6	5.1	6.9	13
Systematics	13	21	53	5.5	52
ee/ff difference	13	21	53	5.5	52
$f_{e \rightarrow \gamma}$ (in norm. region)	0.0012	0.0012	0.0012	0.0012	0.0012

Table 3.6: Errors on the $e\gamma$ electroweak background prediction as a fraction of the $e\gamma$ prediction.

Source of error	Fractional uncertainty (%)				
	[50, 60)	[60, 70)	[70, 80)	[80, 100)	≥ 100
Total	29	29	30	30	30
Statistics	3.6	5.2	6.7	7.2	6.5
Systematics ($f_{e \rightarrow \gamma}$)	29	29	29	29	29

Table 3.7: Errors on the total QCD + electroweak background prediction as a fraction of the total prediction.

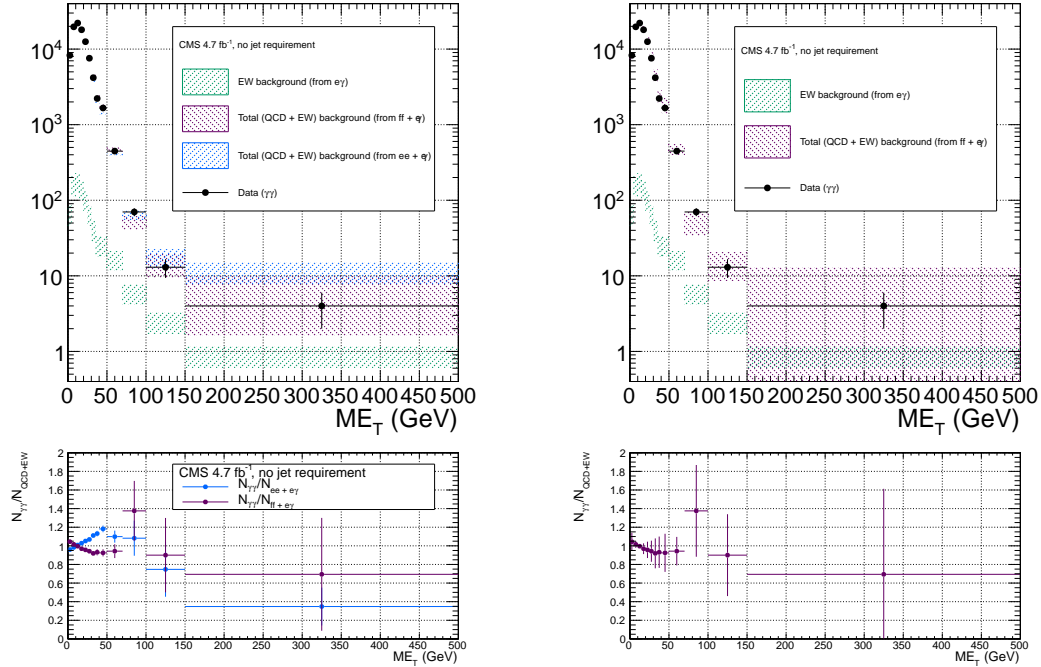
Source of error	Fractional uncertainty (%)				
	[50, 60)	[60, 70)	[70, 80)	[80, 100)	≥ 100
Total ($ee + e\gamma$)	3.9	7.8	15	22	22
Statistics	3.4	7.3	14	21	18
QCD	3.4	7.3	14	21	18
Electroweak	0.13	0.3	0.53	0.79	0.76
Systematics	1.7	2.5	2.4	5.8	11
QCD	1.4	1.9	0.66	4.9	11
Electroweak	1	1.7	2.3	3.2	3.4
Total ($ff + e\gamma$)	14	24	54	30	54
Statistics	6.9	13	26	29	30
QCD	6.9	13	26	29	30
Electroweak	0.11	0.24	0.79	0.83	1.1
Systematics	12	20	47	5.9	43
QCD	12	20	47	4.9	43
Electroweak	0.9	1.3	3.4	3.4	4.8

1107 3.4 Results

1108 Figure 3.23(3.24) shows the \cancel{E}_T distribution of the inclusive(≥ 1 -jet) $\gamma\gamma$ search sample
 1109 along with the predicted \cancel{E}_T distributions of the QCD and electroweak backgrounds.
 1110 The observed number of two-photon events, background estimates and their errors,
 1111 and expected number of inclusive(≥ 1 -jet) two-photon events from two representative
 1112 GGM SUSY models are listed in Table 3.8(3.9). (Details of the SUSY MC production
 1113 are given in Chapter 4 and App. A.) No deviation from the Standard Model prediction
 1114 is observed in the $\gamma\gamma$ search sample.

Table 3.8: Observed numbers of two-photon events, background estimates and their errors, and expected numbers of two-photon events from two representative GGM SUSY models (details of MC simulation given in Chapter 4 and App. A) for the \cancel{E}_T bins used in the search. Errors on the background estimates are detailed in Tables 3.4, 3.5, 3.6, and 3.7. Errors on the expected numbers of GGM events are purely statistical.

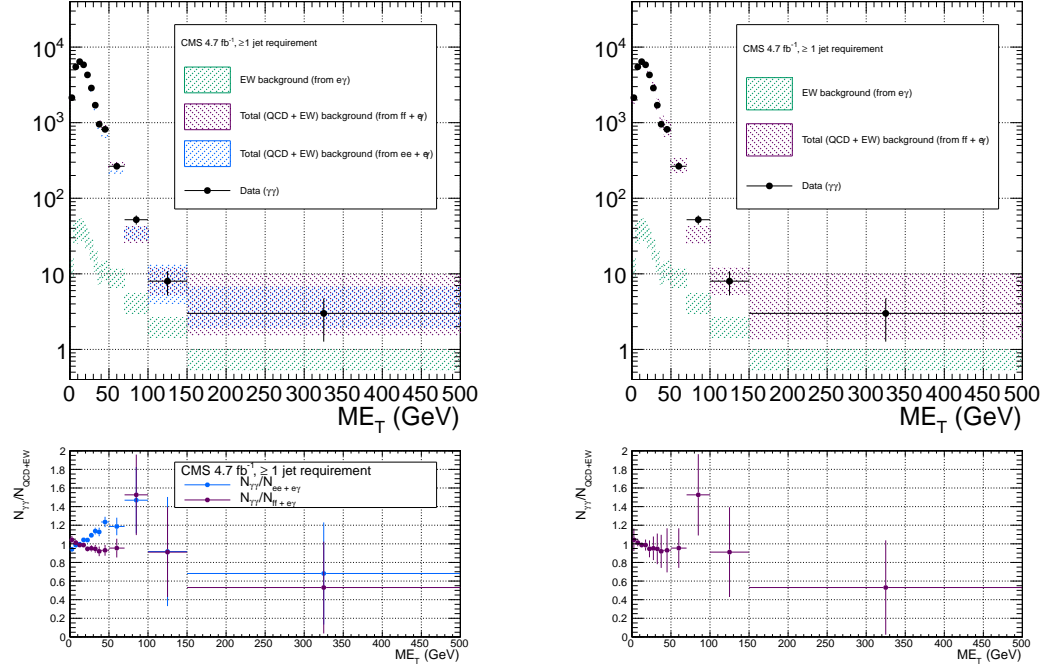
Source	No. events				
	[50, 60)	[60, 70)	[70, 80)	[80, 100)	≥ 100
Data observed ($\gamma\gamma$)	354	93	37	33	17
Background predicted ($ff + e\gamma$)	361 ± 51.5	113 ± 27.1	26.9 ± 14.5	23.9 ± 7.23	20.2 ± 10.9
GGM1 expected (fill in)					
GGM2 expected (fill in)					



(a) $ee + e\gamma$ and $ff + e\gamma$. The widths of the bands correspond to the errors given in Table 3.7, excluding the error associated with the difference between the ee and ff QCD estimates for the $ff + e\gamma$ E_T distribution.

(b) $ff + e\gamma$. The widths of the bands correspond to the errors given in Table 3.7, including the error associated with the difference between the ee and ff QCD estimates.

Figure 3.23: \not{E}_T distribution of the $\gamma\gamma$ search sample (black circles) along with the predicted \not{E}_T distributions of the QCD and electroweak backgrounds (blue band for ee QCD prediction + electroweak prediction, purple band for ff QCD prediction + electroweak prediction). The electroweak background prediction is shown in green. The bottom plots show the ratio of the $\gamma\gamma$ \not{E}_T distribution to the $ee + e\gamma$ background distribution (blue) and $ff + e\gamma$ background distribution (purple).



(a) $ee + e\gamma$ and $ff + e\gamma$. The widths of the bands correspond to the errors given in Table 3.7, excluding the error associated with the difference between the ee and ff QCD estimates for the $ff + e\gamma$ E_T distribution.

(b) $ff + e\gamma$. The widths of the bands correspond to the errors given in Table 3.7, including the error associated with the difference between the ee and ff QCD estimates.

Figure 3.24: E_T distribution of the $\gamma\gamma + \geq 1$ jet search sample (black circles) along with the predicted E_T distributions of the QCD and electroweak backgrounds (blue band for ee QCD prediction + electroweak prediction, purple band for ff QCD prediction + electroweak prediction). The electroweak background prediction is shown in green. The bottom plots show the ratio of the $\gamma\gamma E_T$ distribution to the $ee + e\gamma$ background distribution (blue) and $ff + e\gamma$ background distribution (purple).

Table 3.9: Observed numbers of two-photon + ≥ 1 -jet events, background estimates and their errors, and expected numbers of two-photon + ≥ 1 -jet events from two representative GGM SUSY models (details of MC simulation given in Chapter 4 and App. A) for the \cancel{E}_T bins used in the search. Errors on the background estimates are detailed in Tables 3.4, 3.5, 3.6, and 3.7. Errors on the expected numbers of GGM events are purely statistical.

Source	No. events				
	[50, 60)	[60, 70)	[70, 80)	[80, 100)	≥ 100
Data observed ($\gamma\gamma + \geq 1$ jet)	202	63	27	25	11
Background predicted ($ff + e\gamma$)	200 ± 35.4	77.7 ± 28.1	19.4 ± 8.55	14.7 ± 7.04	14.4 ± 5.59
GGM1 expected (fill in)					
GGM2 expected (fill in)					

₁₁₁₅ **Chapter 4**

₁₁₁₆ **Interpretation of Results in Terms
1117 of GMSB Models**

₁₁₁₈ As shown in Figs. 3.23 and 3.24 and Tables 3.8 and 3.9, no excess of events above
₁₁₁₉ the Standard Model expectation is found in either the ≥ 0 - or ≥ 1 -jet analyses for the
₁₁₂₀ GMSB-sensitive region $\cancel{E}_T \geq 50$ GeV. Therefore, upper limits on the production cross
₁₁₂₁ sections of various GMSB models are calculated and then translated into statements of
₁₁₂₂ exclusion. Section 4.1 describes the GMSB models that were generated with MC and
₁₁₂₃ tested for exclusion. The upper limit calculation and translation to model exclusions
₁₁₂₄ is laid out in Section 4.2. The upper limits themselves are presented in Section 4.3,
₁₁₂₅ and, finally, the exclusions are presented in Section 4.4.

₁₁₂₆ **4.1 Simplified Models**

₁₁₂₇ **4.2 Upper Limit Calculation and Model Exclusion**

₁₁₂₈ The upper limits are calculated according to the prescription followed for the 2011
₁₁₂₉ ATLAS + CMS Higgs limit combination [65]. This prescription utilizes the frequentist
₁₁₃₀ CL_s method [66] with profile likelihood test statistic [67]. The CL_s method and the

profile likelihood are explained in Section 4.2.2, using specific signal MC points to illustrate the procedure. First, however, the signal MC acceptance \times efficiency, which is an input to the limit setting procedure, is presented in Section 4.2.1.

4.2.1 Signal Acceptance \times Efficiency

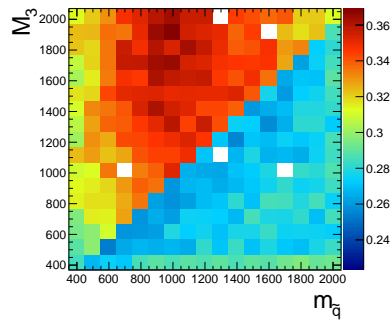
Include wino grids when available and update bino grids with missing points, or replace with old grids. Repeat for ≥ 1 -jet selection.

The signal acceptance \times efficiency (denoted $\mathcal{A} \times \epsilon$), defined for each signal point as the number of $\gamma\gamma$ events selected with $\cancel{E}_T \geq 50$ GeV divided by the total number of events generated, is shown in Figure 4.1 for the three different scenarios described in Sec. 4.1.

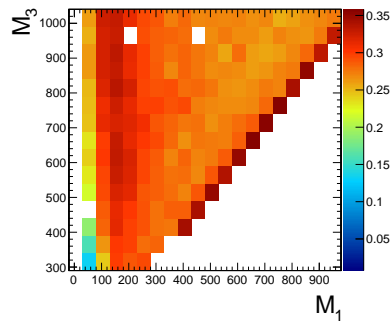
In Fig. 4.1a, the large drop in $\mathcal{A} \times \epsilon$ for $m_{\tilde{q}} > M_3$ is due to an increase in the number of jets produced per event and a consequent reduction in the number of photons that pass the $I_{\text{comb}} < 6$ GeV cut. For $m_{\tilde{q}} > M_3$, there is more phase space available to produce gluinos in the hard scatter than squarks. However, since gluinos must decay via squarks, and in these models all squarks are heavier than the gluino, only the two-jet decay $\tilde{g} \rightarrow q\tilde{q}\chi^0$ is available. Conversely, when $m_{\tilde{q}} < M_3$, there is more phase space available to produce squarks, which may then decay via one jet as $\tilde{q} \rightarrow q\tilde{\chi}^0$. Jets in SUSY events may be very close to the neutralino decay photons, and as a result the photons may fail the strict isolation requirements, leading to lower $\mathcal{A} \times \epsilon$ for jet-rich events.

The broad peak in $\mathcal{A} \times \epsilon$ shown in Fig. 4.1a for $m_{\tilde{q}} < M_3$ and ~ 600 GeV $< m_{\tilde{q}} < \sim 1600$ GeV is due to the $\cancel{E}_T > 50$ GeV cut. The efficiency of the cut decreases as $m_{\tilde{q}}$ decreases because of the fixed M_1 of 375 GeV. If the squark-neutralino mass splitting gets too small, the likelihood of producing an energetic enough gravitino to pass the \cancel{E}_T cut decreases.

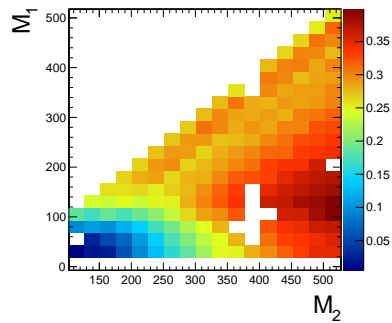
For $M_1 \leq 55$ GeV in Fig. 4.1b, the neutralino is not heavy enough to guarantee



(a) M_2 decoupled ($M_2 = 2$ TeV), $M_1 = 375$ GeV, M_3 vs. $m_{\tilde{q}}$.



(b) $m_{\tilde{q}}$ decoupled ($m_{\tilde{q}} = 5$ TeV), M_3 vs. M_1 .



(c) M_3 and $m_{\tilde{q}}$ decoupled ($M_3 = m_{\tilde{q}} = 5$ TeV), M_1 vs. M_2 .

Figure 4.1: Signal acceptance \times efficiency (defined in the text) for the three different scenarios described in Sec. 4.1.

1157 decay to a photon that can pass the 40 GeV p_T cut, leading to very low or zero $\mathcal{A} \times \epsilon$.
 1158 However, in the case $M_1 = 55$ GeV, $\mathcal{A} \times \epsilon$ increases as M_3 increases because the
 1159 larger gluino-neutralino mass splitting gives the neutralino a larger kinetic energy,
 1160 increasing the chance that it will decay to a photon with 40 GeV p_T or higher. After
 1161 the bino mass increases beyond the threshold needed to produce high p_T photons,
 1162 $\mathcal{A} \times \epsilon$ decreases with increasing M_1 , independent of gluino mass, because higher M_1
 1163 means more phase space is open to decays of the form $\tilde{\chi}_1^0 \rightarrow Z\tilde{G}$ and $\tilde{\chi}_1^0 \rightarrow H\tilde{G}$. The
 1164 two-photon search is naturally not as efficient for these decays.

1165 In the M_2 - M_1 plane, $\mathcal{A} \times \epsilon$ is highest when $M_2 \gg M_1$ and M_1 is low enough for
 1166 neutralino decays to photons to dominate (over decays to Z or H). This scenario is
 1167 what the two-photon search is optimized for. For large M_2 , $\mathcal{A} \times \epsilon$ decreases as M_1
 1168 increases due to the increasing phase space for neutralino decays to Z and H . For low
 1169 M_1 , $\mathcal{A} \times \epsilon$ decreases as M_2 decreases because lowering M_2 makes the lightest chargino
 1170 light enough to play a role as co-NLSP in LHC collisions (cf. Sec. 1.5). In the co-NLSP
 1171 scenario, the chargino will decay to a W boson and a gravitino, squeezing out phase
 1172 space for neutralino decays to photons.

1173 **4.2.2 CL_s and the Profile Likelihood Test Statistic**

1174 The process of setting a cross section upper limit entails (1) defining a test statistic,
 1175 (2) generating a distribution for that test statistic under the signal + background
 1176 and background-only hypotheses, and (3) deciding whether or not the observed value
 1177 of the test statistic is more compatible with the signal + background (i.e. weaker
 1178 upper limit) or background-only (i.e. stronger upper limit) hypotheses by considering
 1179 where it falls within the test statistic distributions. An important requirement on the
 1180 choice of test statistic is that it be able to effectively discriminate between the signal
 1181 + background and background-only hypotheses, i.e. the shape of its distribution for
 1182 these two hypotheses should be different. The procedure for determining the exclud-

ability of a particular model given the value of the test statistic observed should not give rise to pathological behavior in the presence of small signals, low statistics, or weak sensitivity to models, as is commonly the case in high energy physics. These demands on the test statistic and the limit setting procedure itself dictate the choice of the profile likelihood test statistic and CL_s procedure.

In the remainder of this section, the notation is taken from ref. [65].

Profile Likelihood

For a specific model of GMSB, the limit setting procedure concerns the question of whether to reject the signal + background hypothesis $\mu s+b$ in favor of the background-only (Standard Model) hypothesis of b ($\mu = 0$). μ is a dimensionless signal strength parameter. s is the expected number of signal events, calculated from MC simulated signal events as in Secs. 4.1 and 4.2.1. b is the expected number of background events, estimated in Chap. 3. By the Neyman-Pearson lemma [68], the ratio of the likelihood of $\mu s+b$ to the likelihood of b is the test statistic with the highest power to reject $\mu s+b$ at whatever confidence level is desired. In practice, this means that the likelihood ratio is the best discriminator between the GMSB and Standard Model hypotheses.

The likelihood of the signal + background hypothesis as a function of the data (either real or generated) is defined as

$$\mathcal{L}(\text{data}|\mu, \theta) = \prod_{i=1}^N \frac{(\mu s_i(\theta) + b_i(\theta))^{n_i}}{n_i!} e^{-\mu s_i(\theta) - b_i(\theta)} p(\tilde{\theta}|\theta) \quad (4.1)$$

where $N = 5$ is the number of E_T bins used in the analysis ([50, 60) GeV, [60, 70) GeV, [70, 80) GeV, [80, 100) GeV, and [100, ∞) GeV); $s_i(\theta)$ and $b_i(\theta)$ are the expected number of signal and background events in E_T bin i , respectively; n_i is the number of events observed in E_T bin i ; and θ represents all the nuisance parameters

(uncertainties). $p(\tilde{\theta}|\theta)$ represents the product of probability distribution functions (PDFs) for the nuisance parameters, where $\tilde{\theta}$ is the default value of the nuisance parameter. In this analysis, there are eight experimental nuisance parameters per E_T bin:

- Uncertainty on the measured integrated luminosity (4.5% in all bins) [69]
 - Uncertainty on the signal acceptance due to $\epsilon_e^{\text{data}}/\epsilon_e^{\text{MC}}$ (cf. Sec. 2.4.2) (4% in all bins)
 - Uncertainty on the jet energy scale (2% in all bins) **Update with newer figures as per UVa GGM meeting on May 8**
 - Systematic uncertainty on QCD background prediction due to difference between ff and ee estimates (5.5%-53% of the QCD background depending on bin)
 - Systematic uncertainty on electroweak background prediction due to p_T dependence of $f_{e \rightarrow \gamma}$ (29%-30% of the electroweak background depending on bin)
 - Statistical uncertainty on the number of signal $\gamma\gamma$ events (**XXX%-YYY%** depending on model and bin)
 - Statistical uncertainty on the QCD background prediction (7.2%-38% of the QCD background depending on bin)
 - Statistical uncertainty on the electroweak background prediction (3.6%-7.2% of the electroweak background depending on bin)
- and one very small theoretical nuisance parameter: the uncertainty on the signal acceptance due to underlying parton distribution function (PDF) uncertainties. In the limit-setting code, the two uncertainties on signal acceptance are added in quadrature

and treated as one. The uncertainty on integrated luminosity is 100% correlated between bins, and the uncertainty on signal acceptance can usually be treated similarly because the error on $\epsilon_e^{\text{data}}/\epsilon_e^{\text{MC}}$ often dominates the PDF error on acceptance.

Each nuisance parameter PDF is modeled by a log-normal distribution:

$$p(\tilde{\theta}|\theta) = \frac{1}{\sqrt{2\pi} \ln \kappa} \exp\left(-\frac{(\ln \tilde{\theta}/\theta)^2}{2(\ln \kappa)^2}\right) \frac{1}{\tilde{\theta}} \quad (4.2)$$

where $\tilde{\theta} = 1$ and $\kappa = 1 +$ the one-standard-deviation relative error on the nuisance parameter (e.g. for the 4.5% error due to integrated luminosity, $\kappa = 1.045$). **Check this formula.**

Similarly, the likelihood of the background-only hypothesis as a function of the data (either real or generated) is defined as

$$\mathcal{L}(\text{data}|0, \theta) = \prod_{i=1}^N \frac{b_i(\theta)^{n_i}}{n_i!} e^{-b_i(\theta)} p(\tilde{\theta}|\theta) \quad (4.3)$$

The profile likelihood test statistic is defined as

$$\tilde{q}_\mu = -2 \ln \frac{\mathcal{L}(\text{data}|\mu, \hat{\theta}_\mu)}{\mathcal{L}(\text{data}|\hat{\mu}, \hat{\theta})}, 0 \leq \hat{\mu} \leq \mu \quad (4.4)$$

where the $\hat{\theta}_\mu$ maximize $\mathcal{L}(\text{data}|\mu, \hat{\theta}_\mu)$ when it is evaluated at a particular μ , and $\hat{\mu}$ and $\hat{\theta}$ are the global maximum likelihood estimators of μ and θ . The condition $\hat{\mu} \leq \mu$ insures that the obtained cross section upper limit is one-sided, i.e. there is no possibility to find a lower limit on the cross section. The profile likelihood test statistic has the nice property that in the asymptotic (large statistics) limit its PDF can be approximated by analytic formulae, eliminating the need to generate multiple

1244 toy experiments to get the PDF. However, the approximation breaks down for small
 1245 numbers of observed events, so in practice the asymptotic limit is only used as a first
 1246 guess at the location of the true limit.

1247 The PDFs $f(\tilde{q}_\mu | \mu, \hat{\theta}_\mu^{\text{obs}})$ and $f(\tilde{q}_\mu | 0, \hat{\theta}_0^{\text{obs}})$ for the profile likelihood test statistic
 1248 under the signal + background and background-only hypotheses, respectively, are
 1249 obtained by generating toy MC pseudo-experiments. $\hat{\theta}_\mu^{\text{obs}}$ and $\hat{\theta}_0^{\text{obs}}$ maximize Eqs. 4.1
 1250 and 4.3, respectively, when they are evaluated for the observed data. For each μ (and
 1251 the background-only hypothesis $\mu = 0$), the pseudo-experiments are generated by
 1252 picking random values of s and b from a Poisson distribution with the θ fixed as just
 1253 described.

1254 **CL_s**

1255 In the classical frequentist approach, a signal model may be excluded at the 95%
 1256 confidence level (CL) if the probability of any measurement of the test statistic to be
 1257 greater than or equal to the observed value given the signal + background hypothesis
 1258 is 5%. This means that the observed value of the test statistic is so incompatible
 1259 with what one would expect to observe if the signal model were true that, under the
 1260 assumption that the signal model *is* true, the chance of observing a test statistic even
 1261 further afield from the signal expectation is only 5%. Mathematically,

$$p_\mu \equiv P(\tilde{q}_\mu \geq \tilde{q}_\mu^{\text{obs}} | \mu s + b) = \int_{\tilde{q}_\mu^{\text{obs}}}^{\infty} f(\tilde{q}_\mu | \mu, \hat{\theta}_\mu^{\text{obs}}) d\tilde{q}_\mu \quad (4.5)$$

$$p_\mu \leq 0.05 \Rightarrow \text{exclude } \mu$$

1262 where $\tilde{q}_\mu^{\text{obs}}$ is the observed value of the test statistic and p_μ is the p-value. As indicated
 1263 in Eq. 4.5, the p-value is simply the integral of the PDF of \tilde{q}_μ from $\tilde{q}_\mu^{\text{obs}}$ to infinity.

1264 By construction, the classical 95% CL frequentist approach described above will

reject a true signal + background hypothesis 5% of the time. This can happen if the experiment gets “unlucky” and the observation fluctuates low, causing $\tilde{q}_\mu^{\text{obs}}$ to fall in the tail of the \tilde{q}_μ distribution. This poses a problem for the case of very weak signals ($\mu \sim 0$), because it will lead to spurious exclusions of models to which the experiment has little sensitivity. To avoid this pitfall, the CL_s limit setting method is used.

In the CL_s method, the classical frequentist p-value of Eq. 4.5 is simply divided by one minus the p-value of the background-only hypothesis, and it is this ratio, rather than the p-value of the signal + background hypothesis alone, that is required to be ≤ 0.05 . Mathematically,

$$1 - p_0 \equiv P(\tilde{q}_\mu \geq \tilde{q}_\mu^{\text{obs}} | b) = \int_{\tilde{q}_\mu^{\text{obs}}}^{\infty} f(\tilde{q}_\mu | 0, \hat{\theta}_0^{\text{obs}}) d\tilde{q}_\mu \quad (4.6)$$

$$\text{CL}_s(\mu) \equiv \frac{p_\mu}{1 - p_0} \quad (4.7)$$

$$\text{CL}_s(\mu) \leq 0.05 \Rightarrow \text{exclude } \mu$$

where p_0 is the p-value for the background-only hypothesis ($\mu = 0$). In the case of low sensitivity to μ , $p_\mu \lesssim 1 - p_0$, so $\text{CL}_s(\mu) \lesssim 1$ and μ will not be excluded. On the contrary, for high sensitivity to μ ($\mu s \gg \sigma_b$), $p_\mu \ll 1 - p_0$, so models that can be excluded by the criterion $p_\mu \leq 0.05$ will also be excluded by the criterion $\text{CL}_s \leq 0.05$. Compared to the classical frequentist method, CL_s limits can be a little stronger in the case of low signal sensitivity [65].

To determine the upper limit on the cross section of a particular model, the lowest value of μ for which $\text{CL}_s(\mu) \leq 0.05$, denoted $\mu^{95\%\text{CL}}$, is found. The cross section upper limit of that model is then simply $\mu^{95\%\text{CL}}$ multiplied by the expected cross section of the model (cf. Fig. ??).

In contrast to the observed upper limit, the expected upper limit is calculated from an ensemble of background-only MC pseudo-experiments. The distribution $f(\mu_{\text{pseudo}}^{95\%\text{CL}})$

1286 is plotted (one entry per pseudo-experiment). The median expected upper limits and
 1287 $\pm 1\sigma$ and $\pm 2\sigma$ bands are defined as

$$0.5 = \int_0^{\mu_{\text{exp}}^{\text{95\%CL}}} f(\mu_{\text{pseudo}}^{\text{95\%CL}}) d\mu_{\text{pseudo}}^{\text{95\%CL}} \quad (4.8)$$

$$0.16 = \int_0^{\mu_{-1\sigma,\text{exp}}^{\text{95\%CL}}} f(\mu_{\text{pseudo}}^{\text{95\%CL}}) d\mu_{\text{pseudo}}^{\text{95\%CL}} \quad (4.9)$$

$$0.84 = \int_0^{\mu_{+1\sigma,\text{exp}}^{\text{95\%CL}}} f(\mu_{\text{pseudo}}^{\text{95\%CL}}) d\mu_{\text{pseudo}}^{\text{95\%CL}} \quad (4.10)$$

$$0.025 = \int_0^{\mu_{-2\sigma,\text{exp}}^{\text{95\%CL}}} f(\mu_{\text{pseudo}}^{\text{95\%CL}}) d\mu_{\text{pseudo}}^{\text{95\%CL}} \quad (4.11)$$

$$0.975 = \int_0^{\mu_{+2\sigma,\text{exp}}^{\text{95\%CL}}} f(\mu_{\text{pseudo}}^{\text{95\%CL}}) d\mu_{\text{pseudo}}^{\text{95\%CL}} \quad (4.12)$$

1288 The technical procedure followed to calculate the 95% CL cross section upper
 1289 limits for each GMSB model tested is given below.

1290 1. Calculate observed ($\mu_{\text{obs,asym}}^{\text{95\%CL}}$), median expected ($\mu_{\text{exp,asym}}^{\text{95\%CL}}$), and $\pm 1\sigma$ ($\mu_{\pm 1\sigma,\text{asym}}^{\text{95\%CL}}$)
 1291 and $\pm 2\sigma$ ($\mu_{\pm 2\sigma,\text{asym}}^{\text{95\%CL}}$) expected CL_s limits using the asymptotic formulae for
 1292 $f(\tilde{q}_\mu | \mu, \hat{\theta}_\mu^{\text{obs}})$ and $f(\tilde{q}_\mu | 0, \hat{\theta}_0^{\text{obs}})$.

1293 2. Calculate median expected ($\mu_{\text{exp}}^{\text{95\%CL}}$) and $\pm 1\sigma$ ($\mu_{\pm 1\sigma}^{\text{95\%CL}}$) and $\pm 2\sigma$ ($\mu_{\pm 2\sigma}^{\text{95\%CL}}$) ex-
 1294 pected CL_s limits using 100 toy MC pseudo-experiments to generate $f(\tilde{q}_\mu | \mu, \hat{\theta}_\mu^{\text{obs}})$
 1295 and $f(\tilde{q}_\mu | 0, \hat{\theta}_0^{\text{obs}})$.

1296 3. If $\mu_{\pm 2\sigma}^{\text{95\%CL}}$ could not be calculated, set $\mu_{\pm 2\sigma}^{\text{95\%CL}} = \mu_{\pm 2\sigma,\text{asym}}^{\text{95\%CL}}$ instead.

1297 4. If $\mu_{+2\sigma}^{\text{95\%CL}} \neq \mu_{-2\sigma}^{\text{95\%CL}}$ and $\mu_{\text{obs,asym}}^{\text{95\%CL}} > 0.0001$:

1298 • If $\mu_{\text{obs,asym}}^{\text{95\%CL}} > \mu_{+2\sigma}^{\text{95\%CL}}$, set $\mu_{+2\sigma}^{\text{95\%CL}} = 1.3 \times \mu_{\text{obs,asym}}^{\text{95\%CL}}$.

1299 • If $\mu_{\text{obs,asym}}^{\text{95\%CL}} < \mu_{-2\sigma}^{\text{95\%CL}}$, set $\mu_{-2\sigma}^{\text{95\%CL}} = 0.7 \times \mu_{\text{obs,asym}}^{\text{95\%CL}}$.

1300 5. If $\mu_{+2\sigma}^{\text{95\%CL}} = \mu_{-2\sigma}^{\text{95\%CL}}$, set $\mu_{\pm 2\sigma}^{\text{95\%CL}} = \mu_{\pm 2\sigma,\text{asym}}^{\text{95\%CL}}$ instead.

- 1301 6. Scan over 100 equally spaced test values of μ between $\mu_{-2\sigma}^{95\%CL}$ and $\mu_{+2\sigma}^{95\%CL}$ and,
 1302 if $\mu > 0.0001$, calculate the CL_s p-value (p_μ) for this test value of μ to 10^{-6}
 1303 precision using a minimum of 500 toy experiments to generate $f(\tilde{q}_\mu|\mu, \hat{\theta}_\mu^{\text{obs}})$ and
 1304 $f(\tilde{q}_\mu|0, \hat{\theta}_0^{\text{obs}})$.
- 1305 7. Determine the observed ($\mu_{\text{obs},\text{scan}}^{95\%CL}$), median expected ($\mu_{\text{exp},\text{scan}}^{95\%CL}$), and $\pm 1\sigma$ ($\mu_{\pm 1\sigma,\text{scan}}^{95\%CL}$)
 1306 and $\pm 2\sigma$ ($\mu_{\pm 2\sigma,\text{scan}}^{95\%CL}$) expected CL_s limits from the scan p-values for the signal
 1307 + background and background-only pseudo-experiments.

1308 Figure ?? shows $f(\tilde{q}_{\mu<}|\mu_{<}, \hat{\theta}_{\mu<}^{\text{obs}})$ ($\mu < \mu^{95\%CL}$), $f(\tilde{q}_{\mu^{95\%CL}}|\mu^{95\%CL}, \hat{\theta}_{\mu^{95\%CL}}^{\text{obs}})$, $f(\tilde{q}_{\mu>}|\mu_{>}, \hat{\theta}_{\mu>}^{\text{obs}})$
 1309 ($\mu > \mu^{95\%CL}$), and $f(\tilde{q}_\mu|0, \hat{\theta}_0^{\text{obs}})$ for a GMSB model with **some parameters**. The ob-
 1310 served value of the test statistic for each value of μ is also shown, along with the
 1311 p-values.

1312 Finally, a particular GMSB model is excluded if the upper limit on the cross
 1313 section for that model is less than the expected theoretical cross section.

1314 4.3 Cross Section Upper Limits

1315 **Also include figures for ≥ 1 -jet selection.**

1316 Figure ?? shows the observed upper limits on the cross sections for the models
 1317 described in Sec. 4.1. In some ($\mathcal{O}(10^{-2})$) cases, the upper limit is zero due to a
 1318 computational failure. The upper limit for these points is estimated from the average
 1319 of the upper limits of the four neighboring points, as shown in Figure 4.2. If any of
 1320 the four points is also missing a valid upper limit, it is dropped from the average.
 1321 The errors on the individual upper limits used in the estimate are propagated to the
 1322 error on the average.

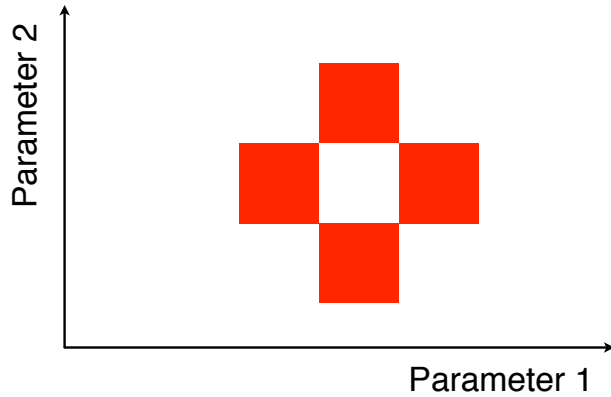


Figure 4.2: Diagram of the points (red squares) used in the estimation of an upper limit when a computational failure occurs (middle white square).

¹³²³ 4.4 Exclusion Contours

¹³²⁴ **Also include figures for ≥ 1 -jet selection.**

¹³²⁵ Exclusion contours for the GMSB models discussed above are shown in Figure ??.

¹³²⁶ The contours are derived from plots of predicted cross section minus cross section
¹³²⁷ upper limit ($\sigma(1 - \mu^{95\%CL})$), where σ is the nominal value of the predicted cross section
¹³²⁸ for a given GMSB model) vs. the two model parameters of interest, so the values are
¹³²⁹ either negative (not excluded) or positive (excluded). Sometimes, a particular point
¹³³⁰ may have a different sign than its four same-sign neighbors (cf. Fig. 4.2) due to a
¹³³¹ fluctuation. In these cases, $\sigma(1 - \mu^{95\%CL})$ for the anomalous point is estimated as the
¹³³² average $\sigma(1 - \mu^{95\%CL})$ of the four neighboring points. The errors on the individual
¹³³³ values of $\sigma(1 - \mu^{95\%CL})$ used in the estimate are propagated to the error on the average.

¹³³⁴ In the plots in Fig. ??, the expected limit (i.e. the contour derived from $\sigma(1 -$
¹³³⁵ $\mu_{\text{exp,scan}}^{95\%CL})$) is drawn in dark orange and the 1σ experimental band around the expected
¹³³⁶ limit (i.e. the shaded region between the contours derived from $\sigma(1 - \mu_{\pm 1\sigma, \text{scan}}^{95\%CL})$) is
¹³³⁷ drawn in light orange. The values of $\mu_{\text{exp,scan}}^{95\%CL}$ and $\mu_{\pm 1\sigma, \text{scan}}^{95\%CL}$ only reflect the experimental

1338 uncertainties given in Sec. 4.2.2.

1339 The observed limits (derived from $\sigma(1 - \mu_{\text{obs,scan}}^{95\% \text{CL}})$) and 1σ theoretical error bands
 1340 around the observed limits in Fig. ?? are drawn in blue. The contours that define
 1341 this band are derived from $\pm(\sigma_{\pm 1\sigma} - \sigma\mu_{\text{obs,scan}}^{95\% \text{CL}})$, where $\sigma_{\pm 1\sigma}$ is the nominal value
 1342 of the predicted cross section \pm the one-standard-deviation theoretical error on the
 1343 predicted cross section. In this way, the experimental and theoretical errors, the latter
 1344 due to imperfect knowledge of the predicted cross section, are shown separately.

1345 The dominant theoretical uncertainties on the GMSB cross sections are due to:

- 1346 • PDF uncertainty (**XXX%-YYY%** depending on model)
- 1347 • Renormalization scale uncertainty (**XXX%-YYY%** depending on model)

1348 The PDF4LHC [70] recommendations are used to calculate the effect of these uncer-
 1349 tainties on the GMSB cross sections. The recommendations state that PDF sets from
 1350 MSTW08 [71], CTEQ6.6 [72], and NNPDF2.0 [73] should be considered in the deter-
 1351 mination of the PDF uncertainties, because these three PDF sets include constraints
 1352 from the Tevatron and from fixed target experiments, as well as from HERA [?], and
 1353 are thus the most complete.

1354 Each collaboration's PDF prediction comes from a global fit to experimental data
 1355 with a certain number of free parameters. The best fit parameters come from mini-
 1356 mizing the χ^2 ; increasing the χ^2 by one from its minimum can be written in terms of
 1357 the N -dimensional Hessian error matrix [?] where N is the number of free parameters.
 1358 To form the i^{th} pair of members of the PDF set, the PDF is evaluated once at the
 1359 parameter values given by the i^{th} eigenvector of the Hessian matrix, and then again
 1360 at the parameter values given by the negative of the i^{th} eigenvector. Each PDF set
 1361 therefore contains $2N$ members, corresponding to the positive and negative values of
 1362 the N eigenvectors [74].

1363 To calculate the PDF uncertainties for a given GMSB model, the leading order

1364 Pythia cross section is reweighted by a factor of the error PDF divided by the leading
 1365 order PDF with which the model was generated. This is repeated for each error PDF
 1366 in a given PDF set. The $\pm 1\sigma$ deviations are proportional to the maximum difference
 1367 between cross sections obtained this way. The actual equation for the $\pm 1\sigma$ errors is
 1368 Eq. (43) of ref. [74]. In the same way, the $\pm 1\sigma$ errors are calculated for the CTEQ6.6,
 1369 MSTW08, and NNPDF2.0 PDF sets. The total error is given by the half the difference
 1370 between the largest $+1\sigma$ deviation and the smallest -1σ deviation [70].

1371 The uncertainties in the PDFs due to the error on $\alpha_S(M_Z)$ are evaluated by
 1372 reweighting the GMSB cross section by a factor of the varied- α_S PDF divided by
 1373 the leading order PDF with which the model was generated. Each PDF collaboration
 1374 provides a group of PDF sets for a range of α_S values around the nominal. The $\pm 1\sigma$
 1375 error envelope is calculated as above, and the PDF and α_S uncertainties are added
 1376 in quadrature to give the total PDF uncertainty.

1377 Note that the quoted GMSB cross sections are evaluated at next to leading order
 1378 using PROSPINO, but it is the leading order Pythia cross sections that are reweighted
 1379 to the next to leading order MSTW08, CTEQ6.6, and NNPDF2.0 PDFs to get the
 1380 error bands. In addition, since to a good approximation the GMSB production cross
 1381 sections for the M_3 - $m_{\tilde{q}}$ scans only depend on M_3 and $m_{\tilde{q}}$, the same PDF errors per
 1382 point are used for the \tilde{B} -like and \tilde{W} -like grids.

1383 **Appendix A**

1384 **Monte Carlo Samples**

1385 A number of MC samples are utilized in this analysis and referred to throughout the
1386 text. Below is a list of the MC samples used and an explanation of what the sample
1387 names mean.

1388 **A.0.1 List of Samples**

1389 1. Drell-Yan:

1390 /DYJetsToLL_TuneZ2_M-50_7TeV-madgraph-tauola/
1391 Fall11-PU_S6_START42_V14B-v1/AODSIM

1392 2. QCD enriched with B and D meson decays to electrons:

1393 /QCD_Pt-20to30_BCToE_TuneZ2_7TeV-pythia6/
1394 Fall11-PU_S6_START42_V14B-v1/AODSIM,
1395 /QCD_Pt-30to80_BCToE_TuneZ2_7TeV-pythia6/
1396 Fall11-PU_S6_START42_V14B-v1/AODSIM,
1397 /QCD_Pt-80to170_BCToE_TuneZ2_7TeV-pythia6/
1398 Fall11-PU_S6_START42_V14B-v1/AODSIM

1399 3. Photon + jet doubly enriched with jets passing an EM filter:

```
1400      /GJet_Pt-20_doubleEMEnriched_TuneZ2_7TeV-pythia6/  
1401      Fall11-PU_S6_START42_V14B-v1/AODSIM
```

4. W leptonic decays:

1403 /WJetsToLNu_TuneZ2_7TeV-madgraph-tauola/
1404 Fall11-PU_S6_START42_V14B-v1/AODSIM

1405

5. $t\bar{t}$:

```
1406 /TTJets_TuneZ2_7TeV-madgraph-tauola/  
1407 Fall11-PU_S6_START42_V14B-v2/AODSIM
```

1408 A.0.2 Explanation of Naming Conventions

- L: charged lepton
 - B: B hadron
 - C: D , or charmed, hadron
 - E: electron or positron
 - G: photon
 - W: W boson
 - Nu: neutrino
 - T: top quark
 - TuneZ2: Pythia tune incorporating 2010 LHC data with CTEQ6L1 [72] PDFs
 - [75]
 - M-50: Generated l^+l^- invariant mass threshold of 50 GeV
 - 7TeV: Generated center-of-mass energy 7 TeV

- 1421 • **pythia6**: Parton showering and hadronization simulated with Pythia v6.424
- 1422 [76]
- 1423 • **madgraph**: Hard interaction generated with MadGraph [77]
- 1424 • **tauola**: τ decays generated with Tauola [78]
- 1425 • **PU_S6**: Generated with S6 pileup scenario
- 1426 • **START42_V14B**: Reconstructed with best alignment and calibration constants
1427 and magnetic field conditions as of August 3, 2011
- 1428 • **Pt_XtoY**: $X \leq$ generated $\hat{p}_T < Y$
- 1429 • **BCToE**: Enriched in B and D meson decays to electrons
- 1430 • **doubleEMEnriched**: Enriched in electromagnetic jets

1431

Bibliography

- 1432 [1] S.L. Glashow, J. Iliopoulos, and L. Maiani, *Phys. Rev. D* **2** (1970) 1285; S.L. Glashow, *Nucl. Phys.* **22(4)** (1961) 579; J. Goldstone, A. Salam, and S. Weinberg, *Phys. Rev.* **127** (1962) 965; S. Weinberg, *Phys. Rev. Lett.* **19** (1967) 1264; A. Salam and J.C. Ward, *Phys. Lett.* **13(2)** (1964) 168.
- 1436 [2] M. Gell-Mann, *Phys. Lett.* **8** (1964) 214; G. Zweig, *CERN 8419/TH. 412* (1964) (unpublished).
- 1438 [3] J. Drees, *Int. J. Mod. Phys.* **A17** (2002) 3259.
- 1439 [4] P.W. Higgs, *Phys. Lett.* **12(2)** (1964) 132; P.W. Higgs, *Phys. Rev. Lett.* **13** (1964) 508; P.W. Higgs, *Phys. Rev.* **145** (1966) 1156.
- 1441 [5] I. Aitchison, *Supersymmetry in Particle Physics: An Elementary Introduction* (Cambridge University Press, Cambridge 2007), p. 4.
- 1443 [6] S. P. Martin, *A Supersymmetry Primer* **v4** (2006) 86. [arXiv:hep-ph/9709356](https://arxiv.org/abs/hep-ph/9709356).
- 1444 [7] M. Dine and W. Fischler, *Phys. Lett.* **B110** (1982) 227; C.R. Nappi and B.A. Ovrut, *Phys. Lett.* **B113** (1982) 175; L. Alvarez-Gaumé, M. Claudson, and M.B. Wise, *Nucl. Phys.* **B207** (1982) 96; M. Dine and A.E. Nelson, *Phys. Rev.* **D48** (1993) 1277; M. Dine, A.E. Nelson, and Y. Shirman, *Phys. Rev.* **D51** (1995) 1362; M. Dine, A.E. Nelson, Y. Nir, and Y. Shirman, *Phys. Rev.* **D53** (1996) 2658.

- 1450 [8] A.H. Chamseddine, R. Arnowitt, and P. Nath, *Phys. Rev. Lett.* **49** (1982) 970; R.
 1451 Barbieri, S. Ferrara, and C.A. Savoy, *Phys. Lett.* **B119** (1982) 343; L.E. Ibáñez,
 1452 *Phys. Lett.* **B118** (1982) 73; L.J. Hall, J.D. Lykken, and S. Weinberg, *Phys. Rev.*
 1453 **D27** (1983) 2359; N. Ohta, *Prog. Theor. Phys.* **70** (1983) 542; J. Ellis, D.V.
 1454 Nanopoulos, and K. Tamvakis, *Phys. Lett.* **B121** (1983) 123; L. Alvarez-Gaumé,
 1455 J. Polchinski, and M. Wise, *Nucl. Phys.* **B221** (1983) 495.
- 1456 [9] P. Meade, N. Seiberg, and D. Shih, *Progr. Theor. Phys. Suppl.* **177** (2009) 143.
- 1457 [10] G. Aad et al., *CERN-PH-EP-2011-160* (2011).
- 1458 [11] T. Aaltonen et al., *Phys. Rev. Lett.* **104** (2010) 011801.
- 1459 [12] CMS Collaboration, *CMS-PAS-SUS-11-009* (2011).
- 1460 [13] <http://en.wikipedia.org/wiki/Tevatron>.
- 1461 [14] E. Fernandez et al., *Phys. Rev. Lett.* **54** (1985) 1118; E. Fernandez et al., *Phys.*
 1462 *Rev.* **D35** (1987) 374; D. Decamp et al., *Phys. Lett.* **B237(2)** (1990) 291; F.
 1463 Abe et al., *Phys. Rev. Lett.* **75** (1995) 613; S. Abachi et al., *Phys. Rev. Lett.* **75**
 1464 (1995) 618; G. Alexander et al., *Phys. Lett.* **B377(4)** (1996) 273; S. Aid et al.,
 1465 *Z. Phys.* **C71(2)** (1996) 211; S. Aid et al., *Phys. Lett.* **B380(3-4)** (1996) 461; B.
 1466 Aubert et al., *Phys. Rev. Lett.* **95** (2005) 041802.
- 1467 [15] O. Buchmueller et al., *CERN-PH-TH/2011-220* (2011).
- 1468 [16] <https://twiki.cern.ch/twiki/bin/view/CMSPublic/PhysicsResultsSUS>.
- 1469 [17] G. Aad et al., *JINST* **3** (2008) S08003.
- 1470 [18] B.C. Allanach et al., *Eur. Phys. J.* **C25** (2002) 113.
- 1471 [19] CMS Collaboration, *CMS-PAS-SUS-12-001* (2012).

- ¹⁴⁷² [20] A. Boyarsky, J. Lesgourgues, O. Ruchayskiy, and M. Viel, *CERN-PH-TH/2008-*
¹⁴⁷³ *234* (2009).
- ¹⁴⁷⁴ [21] E. Komatsu et al., *Astrophys. J. Suppl. Ser.* **180** (2009) 330.
- ¹⁴⁷⁵ [22] C.-H. Chen and J.F. Gunion, *Physical Review D* **58** (1998) 075005.
- ¹⁴⁷⁶ [23] F. Staub, W. Porod, J. Niemeyer, *JHEP* **1001** (2010) 058.
- ¹⁴⁷⁷ [24] R. Brunelière, *Nucl. Instr. Meth. Res.* **A572** (2007) 33.
- ¹⁴⁷⁸ [25] S. Chatrchyan et al. (CMS Collaboration), *JINST* **5** (2010) T03011.
- ¹⁴⁷⁹ [26] CMS Collaboration, *CMS PAS EGM-10-002* (2010).
- ¹⁴⁸⁰ [27] P. Meridiani and C. Seez, *CMS IN-2011/002* (2011).
- ¹⁴⁸¹ [28] P. Adzic et al. (CMS Electromagnetic Calorimeter Group), *Eur. Phys. J.* **C44S2**
¹⁴⁸² (2006) 1.
- ¹⁴⁸³ [29] P. Adzic et al. (CMS Electromagnetic Calorimeter Group), *JINST* **3** (2008)
¹⁴⁸⁴ P10007.
- ¹⁴⁸⁵ [30] M. Malberti, *Nuc. Sci. Symposium Conference Record NSS/MIC IEEE* (2009)
¹⁴⁸⁶ 2264.
- ¹⁴⁸⁷ [31] S. Chatrchyan et al. (CMS Collaboration), *JINST* **5** (2010) T03010.
- ¹⁴⁸⁸ [32] R. Paramatti, *J. Phys. Conf. Ser.* **293** (2011) 012045.
- ¹⁴⁸⁹ [33] Y. Yang, http://www.hep.caltech.edu/cms/posters/Pi0Poster_CMSWeekDec2011.pdf (2011).
- ¹⁴⁹¹ [34] M. Anderson, A. Askew, A.F. Barfuss, D. Evans, F. Ferri, K. Kaadze, Y. Maravin,
¹⁴⁹² P. Meridiani, and C. Seez, *CMS IN-2010/008* (2010).

- 1493 [35] <https://twiki.cern.ch/twiki/bin/view/CMS/ECALEnergyScaleCorrections>.
- 1494 [36] The H $\rightarrow \gamma\gamma$ working group, *CMS AN-2011/426* (2011).
- 1495 [37] M. Cacciari, *LPTHE-P06-04* (2006).
- 1496 [38] M. Cacciari, G.P. Salam, and G. Soyez, *CERN-PH-TH-2011-297* (2011).
- 1497 [39] S. Chatrchyan et al. (CMS Collaboration), *Phys. Rev. Lett.* **106** (2011) 082001.
- 1498 [40] A. Askew, B. Cox, D. Elvira, Y. Gershtein, M. Hildreth, D. Jang, Y.-F. Liu, D.
- 1499 Mason, D. Morse, U. Nauenberg, M. Paulini, R. Stringer, R. Yohay, and S.L.
- 1500 Zang, *CMS AN-2011/515* (2011).
- 1501 [41] F. Beaudette, D. Benedetti, P. Janot, and M. Pioppi, *CMS AN-2010/034* (2010).
- 1502 [42] M. Konecki, in Proceedings of the European Physical Society Europhysics Con-
- 1503 ference on High Energy Physics, Krakow, 2009, Eur. Phys.Soc. Mulhouse (ed.)
- 1504 (unpublished).
- 1505 [43] W. Adam, R. Früwirth, A. Strandlie, and T. Todorov, *J. Phys.* **G31** No. 9 (2005).
- 1506 [44] CMS Collaboration, *CMS PAS PFT-09-001* (2009).
- 1507 [45] CMS Collaboration, *CMS PAS PFT-10-002* (2010).
- 1508 [46] S. Chatrchyan et al., *JINST* **6** (2011) P11002.
- 1509 [47] CMS Collaboration, *CERN-PH-EP 2011-102* (2011).
- 1510 [48] M. Cacciari, G.P. Salam, and G. Soyez, *JHEP* **0804** (2008) 063.
- 1511 [49] G. Salam, talk given at CERN Theory Institute: SM and BSM Physics at the
- 1512 LHC (2009).
- 1513 [50] C.W. Fabjan and R. Wigmans, *Rep. Prog. Phys.* **52** (1989) 1519.

- 1514 [51] <http://www-cdf.fnal.gov/physics/new/top/2004/jets/cdfpublic.html>
 1515 (visited on 16 January 2011).
- 1516 [52] S. Chatrchyan et al. (CMS Collaboration), *JINST* **6** (2011) P09001.
- 1517 [53] CMS Collaboration, *CMS PAS JME-09-002* (2009).
- 1518 [54] T. Sjöstrand, S. Mrenna, and P. Z. Skands, *Comput. Phys. Commun.* **178** (2008)
 1519 852.
- 1520 [55] S. Chatrchyan et al. (CMS Collaboration), *JINST* **5** (2010) T03014.
- 1521 [56] J. P. Chou, S. Eno, S. Kunori, S. Sharma, and J. Wang, *CMS IN-2010/006*
 1522 (2010).
- 1523 [57] Y. Chen, talk given at a meeting of the CMS JetMET group (2011).
- 1524 [58] R. Korzekwa et al., *iEEE Trans. Elec. Dev.* **38** (1991) 745.
- 1525 [59] G. Daskalakis, D. Evans, C.S. Hill, J. Jackson, P. Vanlaer, J. Berryhill, J. Haupt,
 1526 D. Futyan, C. Seez, C. Timlin, and D. Wardrope, *CMS AN-2007/019* (2007).
- 1527 [60] F. James and M. Roos, *Comput. Phys. Commun.* **10** (1975) 343.
- 1528 [61] W. Verkerke and D.P. Kirkby, *CHEP-2003-MOLT007* (2003).
- 1529 [62] J.E. Gaiser, Ph.D. thesis, Stanford University (1982).
- 1530 [63] Information about all CMS datasets is available from the CMS Data Aggregation
 1531 System (DAS), located at the URL <https://cmsweb.cern.ch/das/>.
- 1532 [64] S. Chatrchyan et al., *Phys. Rev. Lett.* **106** (2011) 211802.
- 1533 [65] G. Aad et al. (ATLAS Collaboration), S. Chatrchyan et al. (CMS Collaboration),
 1534 and LHC Higgs Combination Group, *CMS-NOTE-2011/005* (2011).

- 1535 [66] A.L. Read, in *Proceedings of the First Workshop on Confidence Limits, Geneva,*
 1536 2000, edited by L. Lyons, Y. Perrin, and F.E. James (CERN, Geneva, 2000), p.
 1537 81.
- 1538 [67] G. Cowan, K. Cranmer, E. Gross, and O. Vitells, *Eur. Phys. J.* **C71** (2011) 1554.
- 1539 [68] J. Neyman and E.S. Pearson, *Phil. Trans. R. Soc. Lond.* **A231** (1933) 289.
- 1540 [69] CMS Collaboration, *CMS PAS EWK-11-001* (2011).
- 1541 [70] S. Alekhin et al. (The PDF4LHC Working Group), arXiv:1101.0536[hep-ph];
 1542 M. Botje et al. (The PDF4LHC Working Group), arXiv:1101.0538[hep-ph];
 1543 <http://www.hep.ucl.ac.uk/pdf4lhc/index.html>.
- 1544 [71] A.D. Martin, W.J. Stirling, R.S. Thorne, and G. Watt, *Eur. Phys. J.* **C63** (2009)
 1545 189.
- 1546 [72] P. M. Nadolsky, H.-L. Lai, Q.-H. Cao, J. Huston, J. Pumplin, D. Stump, W.-K.
 1547 Tung, and C.-P. Yuan, *Phys. Rev.* **D78** (2008) 013004.
- 1548 [73] R.D. Ball, L. Del Debbio, S. Forte, A. Guffanti, J.I. Latorre, J. Rojo, and M.
 1549 Ubiali, *Nucl. Phys.* **B838** (2010) 136.
- 1550 [74] J.M. Campbell, J.W. Huston, and W.J. Stirling, *Rep. Prog. Phys.* **70** (2007) 89.
- 1551 [75] R. Field, talk given at LHC Physics Centre at CERN Minimum Bias and Un-
 1552 derlying Event Working Group Meeting (2011).
- 1553 [76] T. Sjöstrand, S. Mrenna, and P. Z. Skands, *JHEP* **0605** (2006) 026.
- 1554 [77] dummy
- 1555 [78] dummy